NTNU
Norwegian University of
Science and Technology

Development of Structural Characterization Methods for Polyvinyl Alcohol (PVA)/Nanocellulose Composite Membranes

Henrik Riis

Nanotechnology
Submission date: June 2016
Supervisor: Øyvind Weiby Gregersen, IKP
Co-supervisor: Jonathan Torstensen, IKP

Norwegian University of Science and Technology
Department of Chemical Engineering

Abstract

Structural characterization of polyvinyl alcohol (PVA)/nanocellulose films by scanning electron microscopy (SEM) generally only provides an qualitative estimate of how well the nanocellulose is distributed, and is not capable of giving detailed information on individual nanocellulose particles. Nor do the existing techniques preserve the native, porous state of the water-rich film or allow for uncoated imaging of the polymer films. In an effort to address this, new characterization methods have been developed. This has been done by image analysis of field-emission SEM images which revealed a segregation effect in both cellulose nanocrystals (CNC) and cellulose nanofibrils (CNF) containing PVA films. This was believed to be caused by nanocellulose preferring the water phase over the solid matrix and receding with the water during drying. Further, methods using focused ion beam - scanning electron microscope (FIB-SEM) and reactive ion etching (RIE) have been developed. FIB-SEM cross-sections of stained and unstained samples yielded no direct observation of nanocellulose, but voids believed to be at the PVA/nanocellulose interface were possibly seen. Preservation of the porous structure was done by liquid ethane and nitrogen freeze-drying. Samples frozen in liquid ethane observed in FIB-SEM showed a significant increase in cross-section features believed to be interfacial voids. This may indicate a partial preservation of the porous structure. RIE of the films resulted in surface roughening and a suitable etching recipe was not determined. However, several observations were made indicating the problem originated from surface heating during etching. High-energy particles bombarding the surface and exothermic surface reactions may be the cause of heating combine with poor heat conduction of PVA. Low-voltage SEM (LVSEM) successfully imaged uncoated surfaces with acceleration voltages around 1.4 kV because this range resulted in nearly zero surface charging. Much of the work was also supported by Monte Carlo simulations to determine the viability and likely starting parameters of experiments.

Sammendrag

Strukturell karakterisering av polyvinyl alkohol (PVA)/nanocellulose filmer med sveipende elektron mikroskopi (SEM) gir som oftest kun et kvalitativt estimat på distribusjonen av nanocellulose, og kan ikke gi detaljert informasjon om individuelle nanocellulose partikler. Eksisterende teknikker kan ikke bevare den opprinnelige og porøse tilstanden til de vannholdige filmene og muliggjør ikke SEM avbildning av polymerfilmene uten et metal lag. I et forsøk på å løse disse problemene, har nye karakteriseringsmetoder blitt utviklet. Det har blitt gjort bildeanalyse av felt-emisjon SEM bilder som avslørte en segregeringseffekt i både cellulose nanokrystall- og cellulose nanofibrill-holdige PVA filmer. Dette kom trolig av at nanocellulose foretrakk den vannholdige fasen relativt til den faste matrisen og trakk seg tilbake med vannet etter hvert som det fordampet under tørking. Videre, ble metoder med bruk av fokusert ione stråle-SEM (FIB-SEM) og reaktiv ione etsing (RIE) utviklet. FIB-SEM tverrsnitt på merkede og umerkede prøver resulterte ikke noen direkte observasjoner av nanocellulose, men hulrom man tror oppstår i overgangen mellom PVA og nanocellulose ble trolig sett. Bevaring av den porøse strukturen ble gjort med frysetørking i flytende etan og nitrogen. Prøver frosset i flytende etan som ble observert i FIB-SEM viste en betydelig økning i tversnittstrekk som trolig var de samme hulrommene som tidligere har blitt observert. Dette kan tyde på at metoden har delvis bevart den porøse strukturen. RIE av filmer resulterte i en økning av overflateruhet, og en passende etseoppskrift ble ikke bestemt. Derimot, ble det gjort observasjoner som indikerte at problemet kan være knyttet til oppvarming på overflaten under etsing. Bombardering av energiske partikler og eksotermiske overflatereaksjoner kan være årsaken til oppvarmingen som blir ytterligere forsterket av den dårlige termiske ledningsevnen til PVA. Lav-spennings SEM (LVSEM) var vellykket i å avbilde prøver uten metal lag med akselerasjonspenninger rundt 1.4 kV fordi dette området ga tilnærmet ingen oppladning av overflaten. Mye av arbeidet gjort har også blitt støttet av Monte Carlo simuleringer for å bestemme brukbarheten og startverdier for parametere i eksperimentene.

Preface

This master thesis is the result of the work carried out during the spring of 2016, the last semester of the 5-year Master's degree program in Nanotechnology at the Norwegian University of Science and Technology. The work was performed at the Biorefinery and Fiber Technology Group at the Department of Chemical Engineering.

Professor Øyvind W. Gregersen has been the main supervisor and PhD. Candidate Jonathan Ø. Torstensen has been the co-supervisor. The research has been a continuation of the project work done by the author in the fall of 2015 [1]. Experimental work was done at the NTNU Nanolab cleanroom facilities, at the Department of Chemical Engineering and the Electron Microscopy Lab at the Department of Material Science and Engineering at NTNU. All the work has been carried out independently by the author unless otherwise stated.

Trondheim, 22.06.2016

Henrik Riis

Acknowledgements

The work done during the semester has been challenged, interesting, at times frustrating and very rewarding. The work could not have been done without the help and guidance of several people. First of all, I wish to thank my supervisor Professor Øyvind Gregersen for your positive attitude, high standards to scientific work and openness to my suggestions. A special thanks to my "partner-in-crime" and co-supervisor Jonathan Torstensen. The past year has been immensely more rewarding with your encouragement and dedication. A special thanks to Vegar Ottesen, Kristin Syversen and Erik Roede for insights and suggestions during weekly meetings.

I would also like to thank the staff at NTNU Nanolab and Yingda Yu at the Electron microscopy lab at the Department of Material Science for instrument training and answering all my questions. Your help has been indispensable.

Last, but not least, I would like to thank all my classmates whom have made the last 5 years ten times more fun than I thought possible.

Contents

Glossary

BSE backscattered electrons.

CCS carbon capture and storage.
CNC cellulose nanocrystals.
CNF cellulose nanofibrils.

FE field emission.
FIB-SEM focused ion beam - scanning electron microscope.

LN liquid nitrogen.
LVSEM low-voltage scanning electron microscopy.

PVA polyvinyl alcohol.

RIE reactive ion etching.

SE secondary electrons.
SEM scanning electron microscope.

TEM transmission electron microscope.

UA uranyl acetate.

List of Figures

List of Tables

Chapter 1

Introduction

1.1 Motivation

The global emission of carbon dioxide (CO_2) has risen for many decades, and in recent years there has been an increasing awareness of the impact of greenhouse gas emissions with scientific models substantiating the claims [2–5]. Carbon Capture and Storage (CCS) is considered as one option for reducing global emissions [4, 6]. An example of a full CCS system is shown in Figure 1.1. The most common and mature capture technology is chemical absorption [5–7]. In a conventional coal-fired power plant capture with this technology amounts to 900-1170 kWh/tonne CO_2 captured [4,5]. This limits the use of CCS and makes it economically viable only for large emission sources with relatively high concentrations of CO_2 in their process streams. The capture process accounts for up to 80% of the total cost of CCS [7,8]. Therefore, large-scale implementation of CCS requires an efficient capture process to be economically viable. Membrane separation is a potential replacement for absorption schemes with several economic and environmental advantages [6, 9, 10]. These advantages include significantly lower energy requirements due to no regeneration step and lower costs of installation and operation. There are also no corrosive, explosive or toxic problems due to the absence of a liquid absorbent.

Currently, membranes can only compete with absorption schemes when CO_2 is present in quantities above 20% in the feed gas mixture. The key parameters for

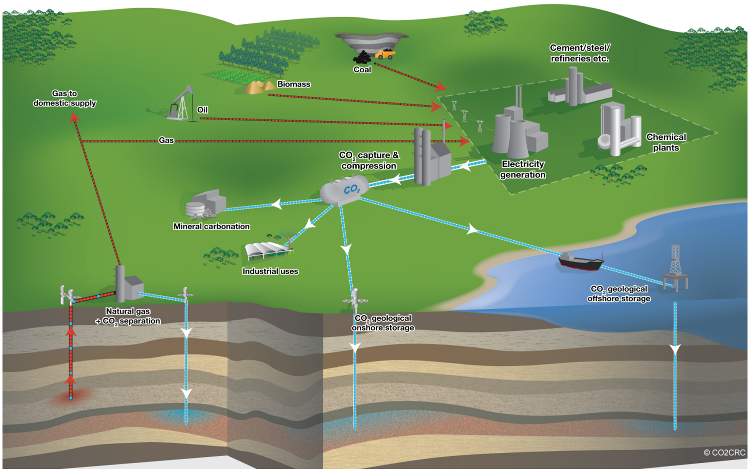

Figure 1.1: An overview of a potential CCS systems. CO_2 is captured from sources like electricity generation and chemical plants. It is transported and either consumed in industrial processes or stored in for example geological formations. Image provided by CO2CRC [11].

membrane performance are permeability[1] and selectivity[2]. Membranes governed by solution-diffusion transport[3] exhibit a trade-off between these two parameters [12, 13]. This trade-off is shown by Robson's upper bound (black lines in Figure 1.2). Membranes must have selectivities and permeabilities above the upper bound to replace absorption methods. New membrane technologies such as facilitated transport (FT) and fixed-site carrier membranes (FSC) are of interest to increase both the selectivity and permeability [14–18]. Facilitated transport selectively enhances the permeability of a targeted gas by incorporating a carrier in the membrane. This carrier reacts spontaneously and reversibly with the targeted gas and promotes transport. Polyvinyl alcohol (PVA) membranes have received significant attention in this field. Water can act as a carrier for CO_2 in such membranes. This raises the question of how to gain and maintain water in the membrane. Cellulose nanofibrils (CNF) and cellulose nanocrystals (CNC) have received much attention in the past decades as a new reinforcing material in polymer composites. They have many advantages over inorganic fillers includ-

---

[1] The permeability is the flux of a specie through a membrane.

[2] The selectivity is the ratio between the permeability of two species.

[3] Transport governed by Fick's law of diffusion.

ing favorable interactions with water making it an excellent filler particle in FT membranes.

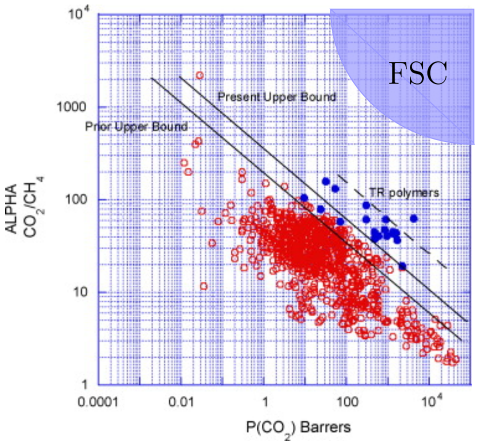

Figure 1.2: The Robeson upper bound is the minimum permeability (horizontal axis) and selectivity (vertical axis) needed for a membrane to be commercial viable. That is, to compete with existing CO_2 separation or scrubbing methods. Fixed-site carrier membranes can offer selectivities and permeabilities far above the upper bound. Figure adapted from [13].

1.1.1 Existing characterization techniques

A modern scanning electron microscope (SEM) can produce high-magnification images of surfaces or cross-sections of materials. Their greatest advantage is their intuitive real-space representation of morphologies over scattering techniques. Early work done by Favier and colleagues demonstrated the reinforcing effect of adding nanocellulose to a polymer matrix [19, 20]. SEM has since been the most common method to evaluate the distribution of nanocellulose [21–24]. The polymer-nanocellulose composite is submerged in liquid nitrogen and fractured. The low temperature and rapid cooling rate of liquid nitrogen makes the material very brittle and easier to fracture. It also has the benefit of not compressing the cross-section like scissors or a scalpel might do. Before imaging, the cross-section is covered with a thin metal layer to prevent charging caused by electron irradiation in the SEM. Composites may also be investigated with transmission electron microscope (TEM). The method is normally used to characterize each component separately, but has also been used to characterize the composite as a whole [25–30]. The advantage of TEM is the very high magnification achievable and single nanocellulose particles can be seen inside the matrix.

The prevailing method of SEM cross-sectional characterization has several drawbacks when a detailed morphology is wanted. The observations made are most often a difference in surface features between a neat polymer cross-section and one with nanocellulose. Although useful, there is no available information on individual nanocellulose distribution. Therefore, conclusions drawn in the literature rarely exceed the two extreme points of whether the nanocellulose is well dispersed or aggregated in the PVA matrix. Another issue is that the membrane is swollen under operating conditions. The current method does not preserve the swollen state prior to characterization. It is of great interest to understand the morphology of the membrane under operating conditions. Conventional SEM is not suited to investigate non-conductive samples without metal coatings. Metal coatings may conceal fine surface details, be impractical to use or in extreme cases deform the sample. Therefore, there is a need for imaging the composite without a metal coating. A last point is that images acquired only give 2-dimensional information about a 3-dimensional material. Gaining a better understanding of the composite requires exploring 3D techniques.

1.2 Aim of the work

The aim of this work has been to investigate characterization techniques for polyvinyl alcohol films with nanocellulose and develop novel techniques where existing ones come up short. There is a need for higher resolution methods that provide detailed information on morphology and distribution of a nanocellulose filler in both two and three dimensions. First, cross-sectional characterization by freeze-fracturing and SEM will be done. Earlier work done by the author during the project thesis showed this method may not be optimal investigating cross-sections of PVA/nanocellulose films [1]. However, as it is the prevailing method in the field, cross-sections will be made and imaged. An attempt will also be made to push the often qualitative analysis further with quantitative analysis with image processing software. Challenges here will be making flat cross-sections that expose nanocellulose clearly for software to identify them. Further, Focused Ion Beam-SEM will be used as a method for making cross-sections and to characterize the films in 3 dimensions. The instrument offers the possibility of making cross-sections by ion beam milling and investigating them by SEM simultaneously. Previous work by the author with ion milling showed that heating was an issue [1]. This along with contrast and resolution are challenges that need to be addressed.

Reactive ion etching (RIE) can remove entire surface layers by dry etching in a highly controlled manner [31]. Wet techniques are not available because PVA swells in polar solvents which most acids are [32]. It offers the benefit of no mechanical deformation brought on by sectioning with cutting tools or freeze fracturing. RIE is extensively used in the semiconductor industry for patterning and material removal, and is therefore well-studied on semiconductor materials. However, some process steps also include polymer coatings. The etching properties of these polymers are therefore available in the literature. Althought, PVA has not been used, parallels can be drawn and used as a starting point for making an etching recipe.

Investigating uncoated samples is also important to determine if there is a discrepancy between coated and uncoated samples. LVSEM is good way to overcome charging problems experienced on non-conductive samples in SEM. It has received increasing attention the last decades with the advancement of SEM technology. Decreasing the voltage has many benefits which will be covered in Chapter 2.4.4. The use of FIB-SEM also requires the imaging of non-conductive surfaces as ion milling exposes uncoated PVA.

There is also a need for sample preparation techniques for swollen samples if the swelled state is to be characterized. Work done by the author during the project thesis revealed more gentle drying methods such as chemical drying and critical-point drying to be too harsh for the PVA films [1]. They were destroyed in the process. Freeze drying and vacuum drying did not result in the film breaking apart, but thickness measurements revealed that the films were thinner than a control sample not dried. It was believed that this was a result of pore collapse. Liquid nitrogen was used as a cryogen and is known to have poor cooling rates compared to liquid ethane. Therefore, liquid ethane will be explored as a preparation method for studying samples in their swollen state.

Figure 1.3 shows an overview of the work done during the master thesis. The work has been done on PVA films directly, and not on membranes with a PVA layer dip-coated on top. This thesis aims to develop novel characterization methods for nanocellulose in PVA films and therefore, studying films will not affect the conclusions in this report. Additionally, films are easier to fabricate, and thicker making them easier to handle and characterize.

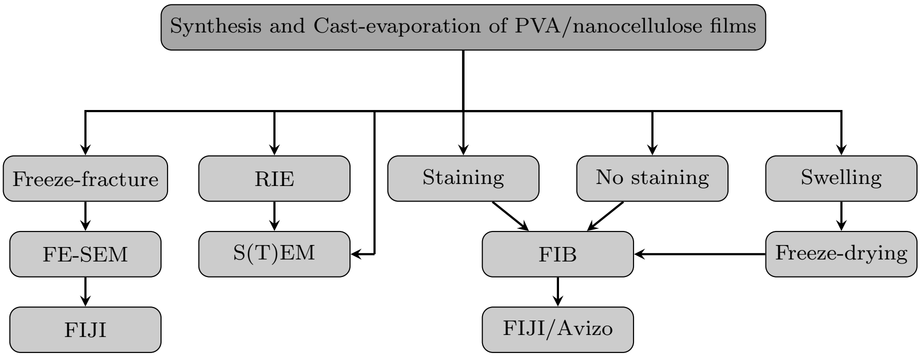

Figure 1.3: Overview of the work presented in the thesis.

Chapter 2

Theory

This chapter covers the relevant material properties needed for understanding the use and characterization nanocellulose and polyvinyl alcohol (PVA). The characterization instruments are also described in detail as a theoretical foundation is important for understanding functionality and possibilities. Some of the chapters below are based on earlier work done by the author [1].

2.1 Cellulose

Cellulose is a natural polymer that can be found many places in nature like in plants, trees, animals and bacteria. It is a desirable material in many applications as it is biodegradable, biocompatible, abundant as well as a renewable resource [33–35]. Cellulose can be regarded on many different length scales from the atomic scale all the way up to the arrangement in cell walls of trees. The basic repeating unit (monomer) is two glucose rings as shown in Figure 2.1. The C1 on one ring is bonded through an oxygen to the C4 on the other ring by a $\beta(1 \rightarrow 4)$ glucose bond. A single cellulose molecule, or chain, may consist of anywhere from 2 000 - 27 000 monomers depending on the source of cellulose [34]. A unique property of cellulose is the large amount of available hydroxyl and oxygen groups, six and three respectively per monomer, able to form intrachain and interchain hydrogen bonds.

Cellulose chains group together by hydrogen bonds and van der Waals forces to form elementary fibrils shown in Figure 2.2 which have both amorphous and crystalline regions. Elementary fibrils come together to form microfibrils. Ordering

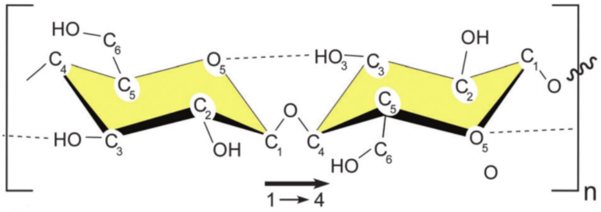

Figure 2.1: Cellulose is a polymer that consists of $\beta(1 \rightarrow 4)$ linked glucose rings as the smallest repeating unit forming linear chains. Hydrogen bonding by hydroxyl groups and oxygen allow for inter- and intrachain bonding. The dotted lines depict intrachain hydrogen bonds. Figure adapted from [36].

on many different length scales is a characteristic of natural cellulose materials and is one reason for its high tensile strength-to-weight ratio [34,37]. Microfibrils align in a highly organized hemicellulose and lignin matrix that make up cell walls in plant cells.

2.1.1 Nanocellulose

Nanocellulose can be prepared from cellulose. Using wood as an example, the goal is to i) remove wood constituents that are not wanted in the final nanocellulose and ii) reduce the dimensions of cellulose into the nanometer/micrometer range. There are generally three process routes to make nanocellulose: Mechanical, chemical and combined chemical and mechanical [34,35]. Purely mechanical methods rely on strong forces to pull cellulose fibers apart into fibrils with for example a homogenizer, grinder or microfluidizer. Grinding is the simplest way, but is very energy-demanding. The chemical and mechanical route combines the previous methods with a chemical pre-treatments like TEMPO-oxidization or carboxymethylation. A chemical process step alters the surface chemistry of cellulose to increase yield and/or reduce the energy requirements for making nanocellulose. It is also beneficial for swelling properties. Lastly, hydrolysis is a chemical method that uses acid treatment to dissolve fibers into nanocellulose. The process steps for hydrolysis and TEMPO-oxidation followed by mechanical fibrillation are shown in Figure 2.3.

By subjecting cellulose to strong mechanical forces, the natural fiber structure will be reduced to smaller fibrils. There are several top-down approaches to do this including all previously mentioned methods. High-pressure homogenization

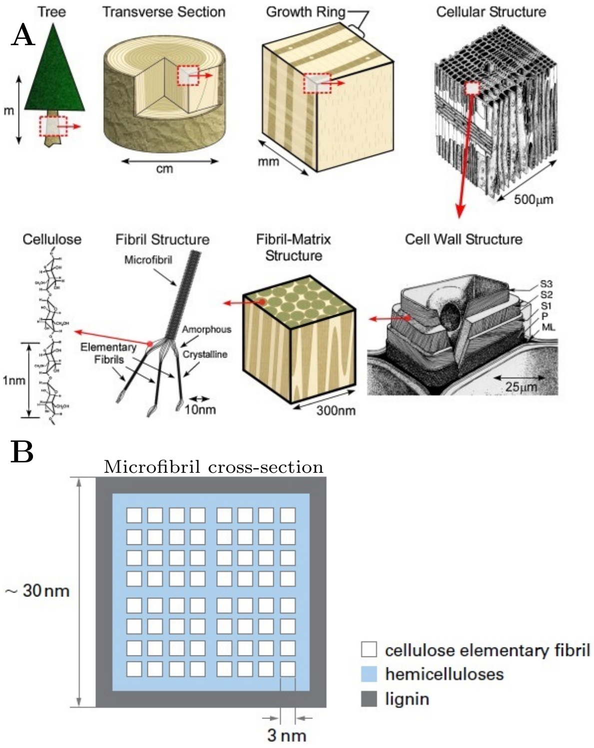

Figure 2.2: A. The hierarchical structure of cellulose in trees. B. The cross-section of a microfibril with the arrangment of elementary fibrils and surrounding hemicellulose and lignin. Each elementary fibril consists of individual cellulose chains in ordered (crystalline) or disordered (amorphous) domains. Figure adapted from [33].

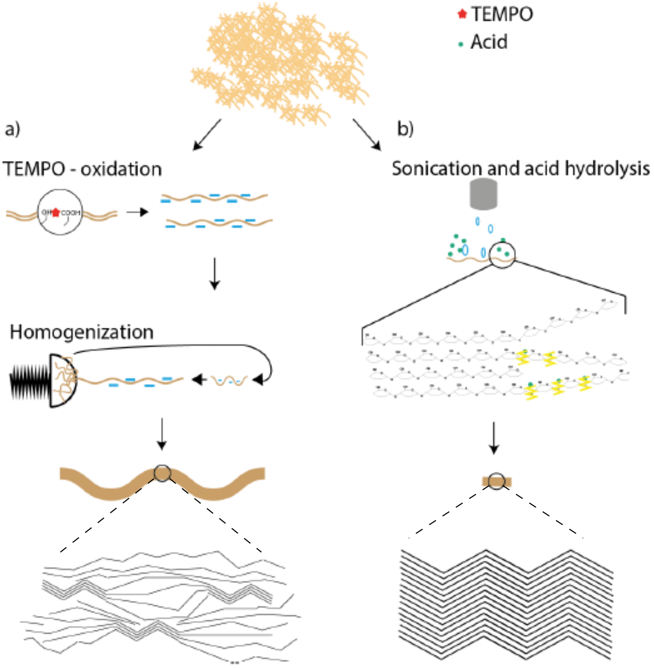

Figure 2.3: Two chemical approaches to creating nanocellulose with a pulp of cellulose fibers as precursor. a) The pulp is TEMPO-oxidized to introduce negatively charged acid groups separating the fibrils. The fibrils are then passed through a homogenizer to further reduced the size to produce cellulose nanofibrils (CNF). b) The amorphous parts of the cellulose fibers are hydrolyzed through acid treatment and sonication. The process creates crystalline nanocellulose particles (cellulose nanocrystals (CNC)). Figure adapted from [38].

produces CNF by mechanical shear forces that pull fibers apart. A slurry of cellulose is pumped to high pressure, in the range of 500-1000 bar and passed through a spring-loaded valve that opens and closes rapidly [34, 39]. This subjects the fibers to a large pressure drop with shear and impacting forces causing them to tear apart [34]. The process is repeated until the desired fibril size is reached.

TEMPO-oxidization, as seen in Figure 2.4, selectively oxidizes the primary C6 hydroxyl group to a carboxylic acid group [40]. The reaction can penetrate into cellulose fibers, but not into microfibrils. Therefore, only the surfaces of microfibrils are oxidized. The carboxylic acid groups cause electrostatic repulsion between microfibrils, and an increase in osmotic pressure, which help overcome hydrogen bonds and van der Waals forces. The reaction proceeds by adding NaClO (primary oxidizer) to an aqueous suspension of cellulose with TEMPO (catalyst and oxidizer) and NaBr (additional catalyst). Figure 2.4 shows the catalytic cycle and role of each species. Carboxymethylation is another common chemical treatment [34]. In this process, the hydroxyl groups are substituted by carboxymethyl groups.

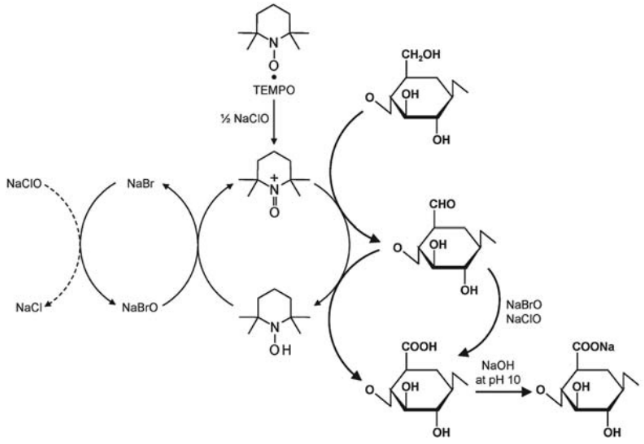

Figure 2.4: The TEMPO-oxidization reaction scheme showing the role of each chemical in oxidizing the C6 hydroxyl group to an anionic carboxylate group with a sodium counter-ion. Figure from [40].

The literature is inconsistent with nomenclature regarding nanocellulose, but efforts have been made by TAPPI to establish international standards [41]. However, a common distinction is made between CNF[1] and CNC. The main difference

---

[1] CNF is also referred to as micro- or nanofibrillated cellulose(MFC and NFC respectively).

between them is that CNF has both crystalline and amorphous regions similar to cellulose fibers whereas CNC largely consists of crystalline regions as shown in Figure 2.3. The morphology of CNF varies greatly depending on the pretreatment and mechanical method used to make them and the cellulose source. CNF made by TEMPO-mediated oxidation and high-pressure homogenization is usually 12-15 nm in diameter and up to several micrometers long [34]. CNC is made by acid hydrolysis. An acid, like sulfuric acid, dissolves the amorphous regions of a cellulose fiber leaving crystalline regions with possibly amorphous regions at both ends. The resulting morphology is also dependent on several parameters like reaction time and temperature, acid-to-pulp ratio and cellulose source. The diameters are in the same range as CNF, but the length is normally between 100-500 nm [35]. The reason CNC is shorter is that the acid-hydrolysis process cleaves a fibrils into smaller segments. Reducing the diameter of fibrils to nano-sized range increases the specific surface area drastically and thus the amount of surface hydroxyl groups. These hydroxyl groups are the reactive sites of cellulose, making CNF and CNC considerably more reactive than larger cellulose fibers [36].

2.2 Polymers

Polymers are macromolecules made by joining smaller molecules in various chain formations. These smaller molecules are called monomers. A polymer can be made from a single monomer, homopolymer, or from several different monomers, heteropolymer [42]. Heteropolymers can have more specific names depending on the sequence of the monomers in the chain. Polymers are regarded as amorphous or crystalline, but no polymer is completely one or the other [42,43]. The performance of polymers is strongly determined by several properties such as chemical composition, structure of monomer unit, polymerization degree or chain length or molar mass, and its distribution, crosslinking, supermolecular structure, crystallinity, stretch orientation etc.

PVA is a thermoplastic synthetic polymer that is soluble in water. It is a saturated polymer meaning the chain of carbon atoms are linked only by single carbon bonds. It has many desirable properties such as being easy to process, biodegradable, biocompatible, non-toxic and easily forms films [37]. PVA has the possibility to form hydrogen bonds because of the many hydroxyl groups as shown in Figure 2.5. This enables strong interactions between PVA and nanocellulose. The same hydroxyl groups also enable swelling in water [44].

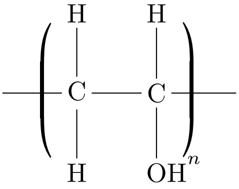

Figure 2.5: The chemical structure of polyvinly alcohol.

2.3 Nanocellulose-water interactions

High specific surface area and high density of surface hydroxyl groups strongly influences the interaction between nanocellulose and water. Interactions with liquid and gas phase water are both important. The rheological behavior of CNC and CNF in water is important because both are present in solution prior to dip coating[2] or cast-evaporation. Interactions with water vapor is critical for membrane functionality during operating conditions. In polymer science, the increase in volume due to absorption of a solvent (water in this case) is called swelling.

Swelling is governed by thermodynamics and can be modeled in many different ways [45–47]. The free energy of the system can be divided into the contributions from each effect. When an ionic hydrogel is placed in a solvent, there are three contributions to the free energy of the system [47].

$$\Delta G = \Delta G_{mix} + \Delta G_{el} + \Delta G_{ion} \tag{2.1}$$

The three right hand terms are the contributions of mixing, elastic-retractive energy and ionic free energy.

2.3.1 Preservation of Water-rich, Porous Structures

When water evaporates from pores and microcavities inside a gel or film, significant pore collapse can occur if the material is not strong enough to withstand the large capillary forces [48, 49]. The meniscus formed during evaporation in pores subjects the walls to a tensile stress that is dependent on pore size and the surface energy (tension) of the liquid and solid phase. While in use, the membrane will have a considerable water content. However, examination techniques require the

---

[2] For membrane applications, the PVA/nanocellulose film is dip-coated on a support membrane.

PVA/nanocellulose films to be dry, in most cases very dry because many instruments require vacuum. Thus there is a need for preservation of the native state of the samples. Freeze-drying is a common way to mitigate pore collapse. By sublimating the ice rather than evaporate the water, a vapor-liquid interface can be avoided. In freeze-drying, samples are rapidly cooled by a cryogen followed by drying in a vacuum chamber. Freezing is recognized as the most important step in most cryotechniques and is not a straightforward process [50]. The native state of a sample could be disrupted if the freezing rate is not sufficiently high as nucleation and growth of ice crystals may occur. Ice has a lower density than water and therefore expands in the solid state relative to the liquid phase. In order to preserve the native state, the water should be frozen in an amorphous state as to prevent the crystal growth. This requires very high cooling rates, around 10^3 – 10^4 K/s [50, 51]. Liquid nitrogen is a common cryogen that has a cooling rate of 80 K/s [50]. This rate is not sufficient for freezing water amorphously. Figure 2.6 shows cooling rates of liquid ethane as a function of volume to area ratio the sample cooled. The desired cooling rates can be achieved in this cryogen if a sample has the right shape and size. Once water has been frozen amorphously, it must be kept above its devitrification temperature of 143℃ [51]. Otherwise, the ice will start to crystallize and grow.

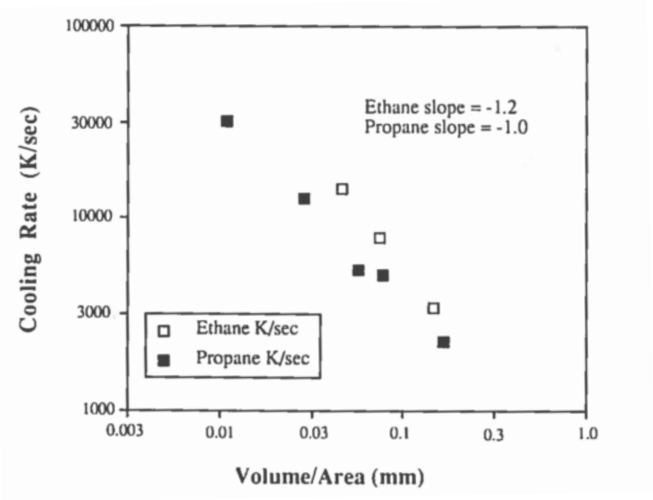

Figure 2.6: The cooling rates of liquid ethane and liquid propane as a function of volume/area ratio of the sample being cooled. Figure taken from [50].

2.4 The Scanning Electron Microscope

The source of a scanning electron microscope (SEM) emits a beam of electrons that is focused into a tiny spot on the sample surface by several lenses and aperatures as in Figure 2.7. An image is formed by scanning the region of interest line by line and collecting electrons emitted by the sample with a detector. An image is generated by intensity measurements of electrons by the detector at each point in the region of interest.

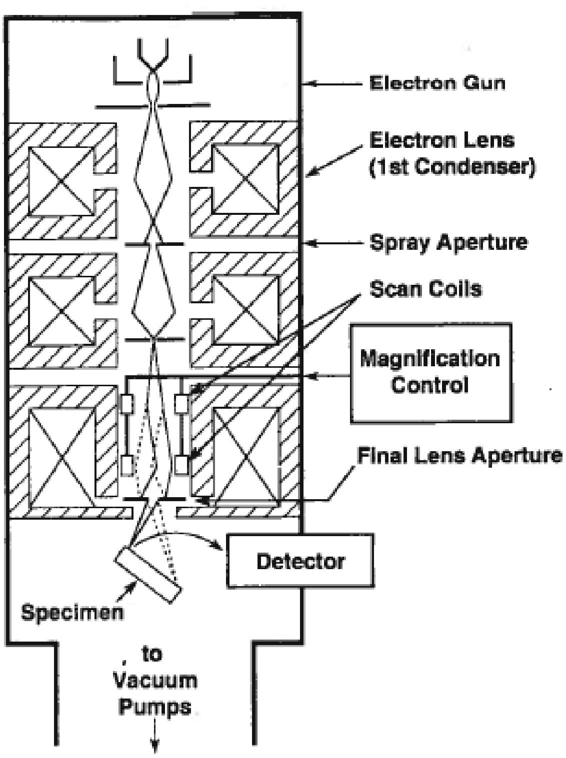

Figure 2.7: An overview of a SEM column with lenses and aperatures. The scan coils deflect the beam to each scan point. The placement of the detector varies between SEMs and with the type of detector. Figure adapted from [52].

2.4.1 Electron Sources and Acceleration Voltage

All SEMs used in this report have cold field electron emission sources. This is a common source for high-resolution SEM compared to thermionic emission sources used in conventional SEMs. Field-emission sources have higher brightness, longer lifetimes and narrower energy spreads resulting in higher achievable resolution [52]. The electrons are emitted from the tip of a tungsten "needle" by a strong voltage difference, V_1 in Figure 2.8 at room temperature. This is why the source is called *cold* field because heat is not used to assist in electron emission, only an electric field. V_1 gives the electrons at the tip enough energy to overcome their work function[3] and tunnel into vacuum. The voltage V_2 is called the acceleration voltage and sends the electrons towards the sample.

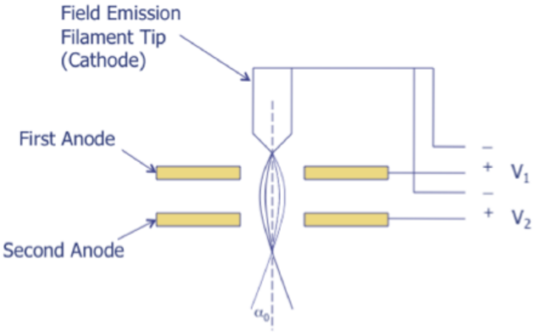

Figure 2.8: Schematic diagram of a field emission tip. V_1 is called the extraction voltage and extracts electrons from the tungsten tip. V_2 is called the acceleration voltage and accelerates the electrons through the column towards the surface. Figure taken from [52].

2.4.2 Electron Beam - Specimen Interactions

Electrons in the beam, also called primary electrons, interact with the sample in a volume called the interaction volume. A schematic representation of the typical teardrop shape of the interaction volume is shown in Figure 2.9. The exact size and shape will depend on sample composition as well as incident beam energy [52]. Primary electrons will collide with atoms and electrons in the interaction

---

[3] The energy required for an electron to tunnel into vaccum from a solid.

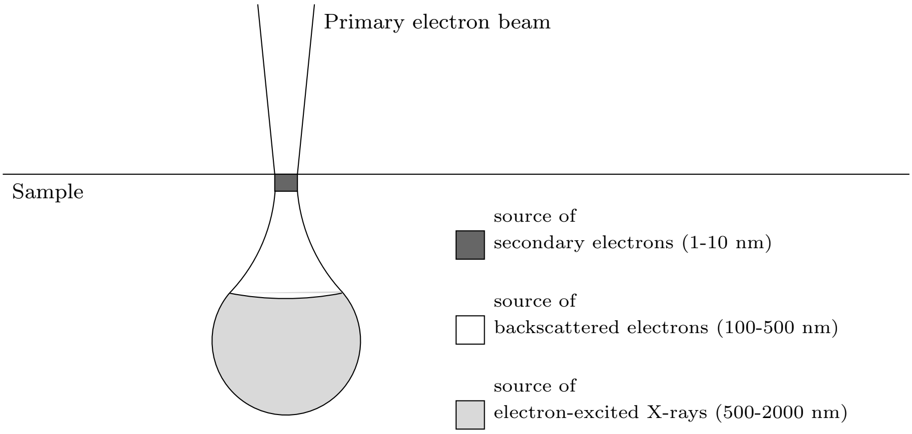

Figure 2.9: Sample interaction volume in a SEM. The interaction volume of secondary electrons is significantly smaller than backscattered electrons due to the large difference in kinetic energy. Depths noted in the figure are for PVA at an acceleration voltage of 5 kV. The depth will increase with acceleration voltage and decrease with the atomic number of the sample.

volume. These are called scattering events and are governed by complicated physical processes. These processes will not be discussed here and the interested reader is referred to the literature [52–54]. In short, two events may occur, elastic and inelastic scattering. These can change the direction and energy of primary electrons. Elastic scattering gives rise to backscattered electrons (BSE) while inelastic scattering produces several distinct signals including secondary electrons (SE). A single primary electron undergoes many scattering events before either losing all its energy[4] and coming to rest within the sample or exiting the sample through a surface. The distance between two successive collisions is called the mean free path and is calculated by

$$\lambda = \frac{A}{N_0 \rho Q} \tag{2.2}$$

where A is the atomic weight of the sample (g/mole), N_0 is Avogadro's number, ρ is the sample density (g/cm^3) and Q is the scattering cross-section. Higher acceleration voltage (higher initial energy) will cause the beam electrons to penetrate deeper into the sample. The number of scattering events per unit distance

---

[4] Not precisely true as it loses energy down to kT

traveled is a function of parameters such as the average atomic number and density of the sample and will affect the size of the interaction volume. Determining the precise interaction volume is difficult. However, an estimate of the interaction volume in a specific material system and for a specific acceleration voltage can be done with Monte Carlo simulations [55, 56]. A knowledge of the interaction volume is vital to understand what volume the detected signal is coming from.

Backscattered electrons

BSE are primary electrons that undergo elastic scattering (angles ≥ 90°) with atoms in the sample. The probability of scattering is called a scattering cross-section. The scattering cross-section (Q) for scattering events with angles larger than ϕ_0 is

$$Q(\geq \phi_0) = 1.62 \times 10^{-20}(\frac{Z^2}{E^2})cot^2(\phi_0/2)[(events \geq \phi_0)/electron(atoms/cm^2)] \tag{2.3}$$

where Z is the atomic number of the sample and E is the electron energy. Numerous scattering events cause primary electrons to deviate enough from their path to escape as BSE through a surface and subsequent collection by a detector. This is shown in Figure 2.10. The energy range of the electrons are from 50 eV to E_0, the primary beam energy. Electrons below 50 eV are defined as secondary electrons [52]. The backscatter coefficient is a measure of how many primary electrons are detected as backscattered electrons and is defined as

$$\eta = \frac{n_{BSE}}{n_B} \tag{2.4}$$

where n_{BSE} is the number of backscattered electrons and n_B is the number of primary electrons. η is largely insensitive to incident beam energy, but does display some complicated behavior below 5 keV [52]. Fortunately, experimental work and simulations has led to empirical equations for estimating the backscatter coefficient for beam energies between 1 and 40keV.

$$\begin{aligned} & \eta(Z,E) = E^m C && (2.5) \\ \text{where,}\quad & m = 0.1382 - (0.9211\sqrt{Z}) \\ & C = 0.1994 - 0.2235(lnZ) + 0.1292(lnZ)^2 - 0.01491(lnZ)^3. \end{aligned}$$

Monte Carlo simulations can also be used directly to determine η of more complicated material systems [55, 56].

Secondary Electrons

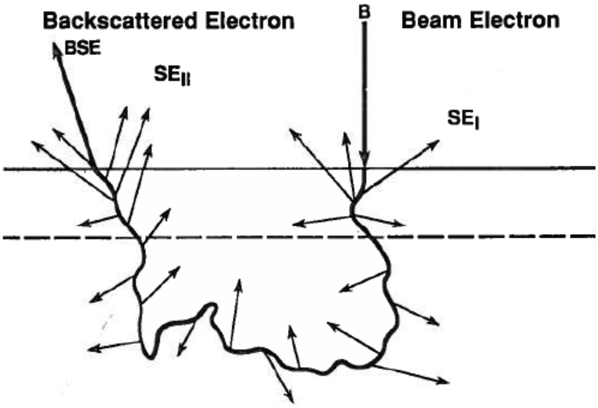

Figure 2.10: The generation of BSE and SE by primary electrons. The continuous, thick line is the trajectory of a primary electron which is scattered multiple times and finally escapes as a BSE. The arrows indicate scattering events that generate SE. Secondary electrons that are detected are therefore generated by two sources, primary electrons (SE_1) around the beam spot and by backscattered electrons (SE_2) as they escape. SE_2 electrons are generally considered noise as they originate from areas not in close proximity to the scan point. Note that BSE can generate further noise if they strike the chamber walls and generate SE_3. Figure adapted from [52].

SE are the result of inelastic scattering events. Primary electrons collide with electrons in the outer shells of the atoms in the sample giving them enough energy to be ejected. The SE will travel in the sample and if close enough to the surface, escape into vacuum and be caught by the detector. The SE coefficient is

$$\delta = \frac{n_{SE}}{n_B} \tag{2.6}$$

where n_{SE} is the number of SE emitted by the sample. SE are defined to be all electrons emitted by the sample with a kinetic energy between 0 and 50 eV

[52]. This does mean that some backscattered electrons may be detected as a secondary electron if their energy is low enough upon leaving the sample, but the contribution is so small that it is inconsequential. A consequence of their low kinetic energy is that only SE close to the surface may escape. Figure 2.10 shows that SE generated deeper than 10 nm rarely have the energy to escape the sample. Secondary electrons is therefore essentially a surface imaging technique. SE emission is highly sensitive to incident beam energy. When the beam energy is low, most of the SE will be generated within the escape depth because the majority of the incident electron trajectories are also within the escape depth [52]. However, at higher beam energy the incident electrons penetrate further and the majority of trajectories is below the escape depth.

As with BSE, SE coefficients can be modeled with semi-empirical models assuming some simplifications. Specifically for polymers, the SE coefficient can be expressed as

$$\delta = KE^{-0.725}. \tag{2.7}$$

E is the acceleration voltage and K is a constant that can be written in a number of different ways, but is based on material parameters [57].

2.4.3 Contrast

Contrast is the difference in signals that makes an object distinguishable from its surroundings. It is defined as

$$C = \frac{S_2 - S_1}{S_2}, \qquad S_2 \geq S_1 \tag{2.8}$$

where S_1 and S_2 are signals from two chosen points of interest. Since the signal is proportional to the backscatter coefficient (η) for the BSE signal, a good approximation to Equation 2.8 is

$$C = \frac{\eta_2 - \eta_1}{\eta_2}. \tag{2.9}$$

Equation 2.3 and 2.9 shows that contrast from BSE depend strongly on atomic number because of the increased probability of scattering events, approximately as Z^2 [52]. This is the reason why BSE gives compositional contrast. A difference in average atomic number between points of interest will result in a difference in signal and ultimately contrast. Secondary electrons give topographical contrast. Figure 2.11 shows that SE generate deep in the interaction volume on a flat surface have no possibility to escape. However, when the surface is not smooth, these electrons have additional surface area to escape through. The detector will collect more electrons from these points compared to the smooth areas. This will result in a signal difference and therefore contrast. BSE are also affected by this and may produce topographical contrast.

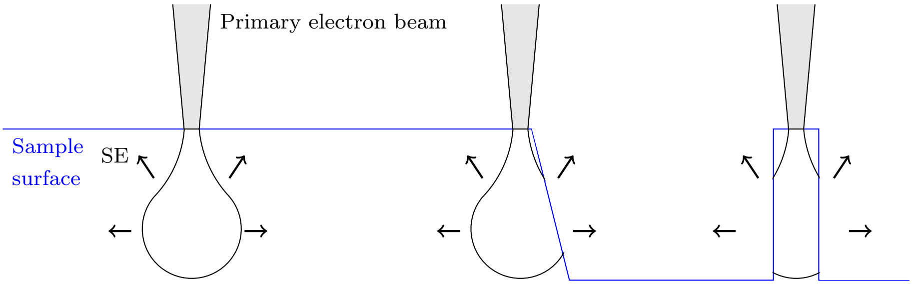

Figure 2.11: An example of how topographical contrast is produced by secondary electrons. On a flat surface, as to the left, SE generated in the bulk below the escape depth cannot escape. When the surface has topography, SE in the interaction volume have additional surface(s) to escape from as in the two right examples. Therefore electrons which normally are trapped on a flat surface, now escape and contribute to an increased signal from such points.

2.4.4 Low-voltage SEM for polymers

Polymers are renowned for their resistance to characterization by microscopy [42, 57, 58]. They are generally non-conductive and also quite sensitive to beam-induced radiation damage. Few general and straight-forward techniques exist to image composites made of polymers due to difficulty in achieve contrast between filler and matrix, charging and beam-induced damage [57]. All of these problems can be overcome (or partially mitigated) by using low-voltage SEM (LVSEM). The high brightness inherent to the field-emisision gun source allows for sufficient signal production despite low acceleration voltage and beam current. The definition of LVSEM is imaging with an acceleration voltage below 5 keV.

Charging

When imaging a non-conductive sample in a SEM, charging may occur. Charges trapped in the sample will generate an electric field that rapidly modifies the trajectories of newly arriving primary electrons. This process will happen over and over until a steady-state has been reached [58]. Using conservation of charge (Kirchhoff's law) the following equation is valid for a sample under irradiation.

$$I_S = I_P - I_{BSE} - I_{SE} = I_P(1 - \eta - \delta) \tag{2.10}$$

I_S is the specimen current flowing to ground and I_P is the beam current. I_{BSE} and I_{SE} is the loss of electrons from backscatter and secondary emission respectively. I_s is set to zero when a sample is non-conducting because no current is flowing through the sample to ground. Depending on the value of η and δ, the backscatter and secondary electron coefficient respectively, the local charge on the sample can either be positive or negative. Charge introduces image distortion like the appearance of sample drift. Fluctuations in image intensity also appear where negative charge produces bright areas because incoming primary electrons are repelled and positive charge produces darker regions.

Charging can be overcome by coating the sample with a thin conductive layer like Au, Pt, Pd etc, but in some cases a coating is unwanted. The reason can be that a coating layer will conceal contrast or cover structures of interest. The metal coating will also have a topography or structure of its own that can result in misleading images at high resolutions. A typical example is that gold is unsuitable as a coating for high-resolution work due to large grain sizes [42, 53]. Another approach is to reduce the acceleration voltage because this increases SE emission as seen from Equation 2.7. If the voltage is reduced sufficiently, a point is reached where Equation 2.10 balances with I_s set to zero. This point is called the zero-charging point, also referred to as E_2. Figure 2.12 demonstrates that in E2 the amount of emitted electrons equals the amount of incident electrons. At this acceleration voltage, the sample does not need to be conductive as there are no excess electrons that need to be removed. In reality, the voltage needs to be reduced below E_2 [58]. However, this is not a problem as the zero-charging point for a certain material is found by experimentation [59].

Contrast and resolution

The reduction in beam energy, and therefore reduction in interaction volume and electron range, affects the signals produced by BSE and SE. Backscattered emis-

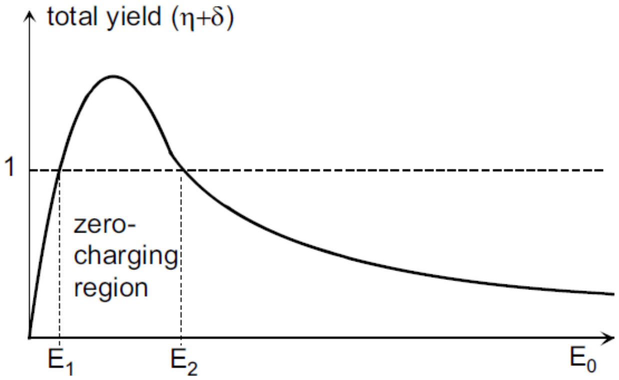

Figure 2.12: The amount of emitted SE (δ) and BSE (η) electrons per incident electron as a function of acceleration voltage. The theoretical point of E2 is where zero charging will occur as the amount of emitted electrons equals the amount of incident electrons. At higher acceleration voltages, the sample will charge negatively while at lower voltages the sample will charge positively. E_1 is also a point where zero charging occurs, however the low acceleration voltage required to reach this point makes it of little relevance experimentally.

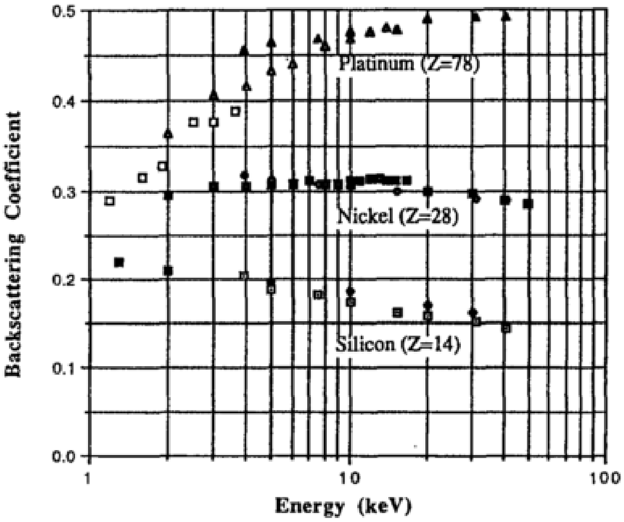

Figure 2.13: The backscatter coefficient for three different elements as a function of incident beam energy. At lower voltages, high Z elements reduce their coefficient while low Z elements increase theirs. This leads to similar coefficients between elements and reduced contrast. LVSEM is in the range where the coefficients converge. Figure taken from [59].

sion decreases for heavy elements at low voltages, but increases for light elements. This leads to most materials having a backscatter coefficient in the range of 0.2-0.3 at 1 keV and the contrast between them reduced. Figure 2.14 demonstrates this for three elements. Contrast in secondary electron images increase because of two effects. As described above, more signal is generated at lower acceleration voltage due to beam trajectories. The second effect is that small surface features previously "washed out" will become more visible. When the beam energy is high, a large part of the SE signal originates deeper in the sample, making the signal from small surface features small. Lowering the voltage, increases the signal from the surface features. Resolution is increased for both SE and BSE as the interaction volume and electron range is significantly smaller. At low enough voltages, BSE resolution can surpass SE as the signal depth of BSE becomes shallower than SE. Staining is commonly used at low voltages because of the reduced compositional contrast from BSE. It is worth noting that compositional contrast has been reported for SE at low voltages. Due to the shallow penetration depth at low voltages, build-up of carbonaceous material on the sample can be very detrimental. Carbon exists everywhere, even in the vacuum chamber. A layer only a few nanometer thick can alter the backscatter coefficients sufficiently to eliminate contrast between two areas that in theory should have contrast. Therefore, care must be taken to limit carbon build-up. This can be done by avoiding contamination prior to imaging and also to pause the beam whenever imaging is not necessary.

Signal-to-Noise Ratio

Noise is the largest limiting factor in low-voltage SEM making the signal-to-noise ratio critical [60]. In order to increase this ratio high enough to acquire meaningful images, the beam current and scan time, that together determine the beam dose, must be increased at the expense of image resolution, increased charging and increased sample damage. Probe size[5] is also increased at lower voltages adding to the challenge [52].

Beam-induced damage

The majority of the energy from the primary beam is converted to heat at the scan point and in the interaction volume [57]. The beam dose, which determines the number of electrons each scan point receives, is a critical parameter. This is especially detrimental to polymer samples as heat conduction is closely linked

---

[5] The spot size of the electron beam as it hits the surface of the sample.

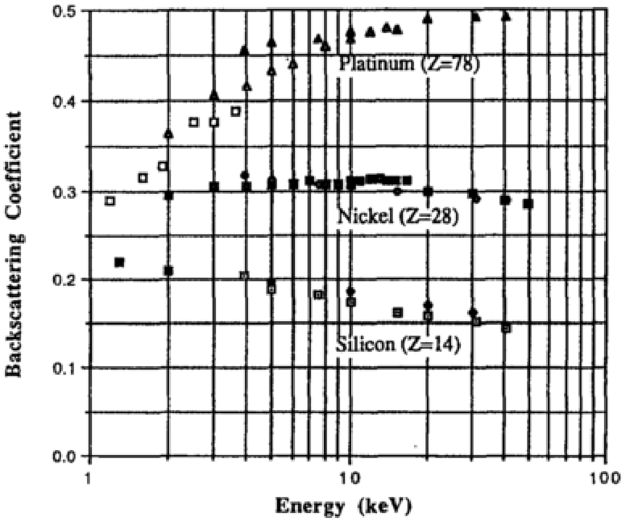

Figure 2.14: The backscatter coefficient for three different elements as a function of incident beam energy. At lower voltages, high Z elements reduce their coefficient while low Z elements increase theirs. This leads to similar coefficients between elements and reduced contrast. Figure taken from [59].

to electric conduction. Therefore, heating is confined locally. Beam-induced damage is not quantified adequately for polymers and there is some disagreement in the literature. One paper claims that generally below 2 kV damage becomes insignificant [57]. This allows beam dose to be increase significantly without causing the damage it would at higher acceleration voltages. Another paper claims that there is a steady increase in sample damage at low voltages followed by sharp decrease. This is based on the stopping power per unit length which shows the same trend [59]. Figure 2.15 shows beam damage caused by an electron beam. Heat causes the polymer collapse.

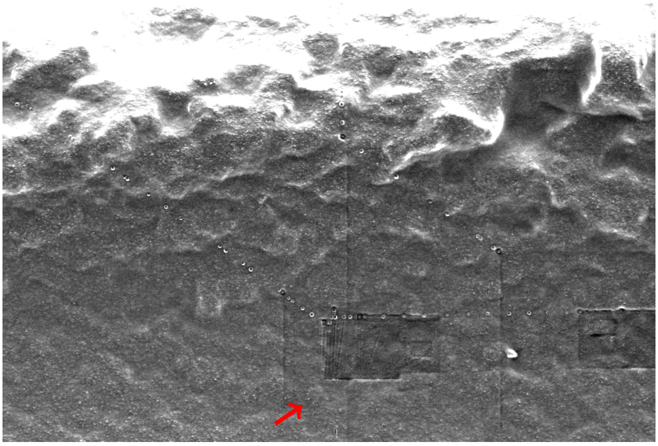

Figure 2.15: Example of beam-induced damage to a PVA/nanocellulose film. The squares show that areas scanned at high magnification collapse, distorting and concealing surface features. The effect increases with magnification and acceleration voltage. The diagonal line of bubbles appear when manually increasing magnification sequentially instead of instantaneous switching between low and high magnification.

2.5 Dual-Beam FIB-SEM system

A Dual-Beam FIB-SEM consists of an electron column and an ion column integrated in the same vacuum chamber. The electron column is mounted directly above the sample and functions as a SEM described in Chapter 2.4. The ion column is mounted at an angle to the electron column. A schematic of the instrument is seen in Figure 2.16. The ion beam is extracted from a liquid metal ion source which is a tungsten tip is coated with liquid gallium [61]. Surface tension and an electric field form the Ga into a Taylor cone with a very small diameter, around 4 nm. Ga ions are extracted with a strong acceleration voltage and passed through several apertures and lenses that focus the beam. The process is similar to how an electron source functions. The beam is subsequently scanned across the surface. The FIB has four modes of operation: milling, imaging, deposition and implantation. Several modes can happen at the same time, so parameters must be optimized to enhance the desired mode. This section will only cover milling as imaging, deposition and implantation are of little relevance for the current study.

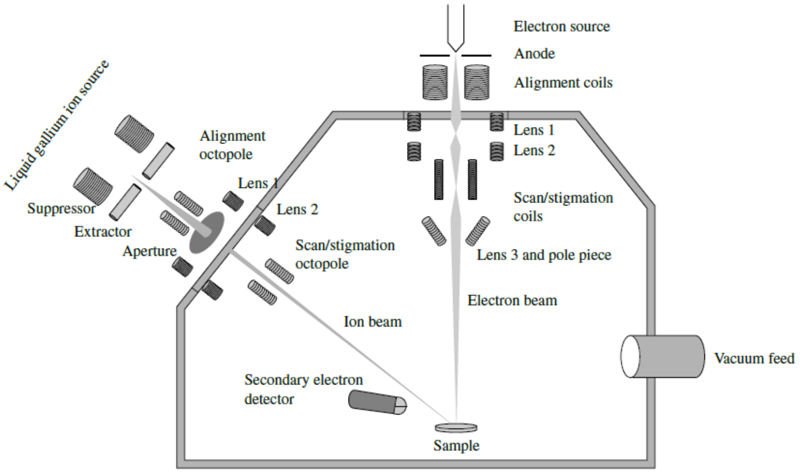

Figure 2.16: Schematic overview of a Dual-Beam FIB-SEM. Figure taken from [62].

Milling

Milling occurs when the relatively heavy Ga ions strike the surface of a sample causing atoms and molecules to be expelled from their position in a sputtering effect. High kinetic energy of incident ions are transferred to stationary atoms in the sample giving them enough energy to be ejected. Some ions will remain implanted in the sample while the rest including the sputtered material is pumped away by the vacuum system. The large size of ions compared to electrons make interactions with atoms much more probable. Sputtering may cause sample damage like vacancies, amorphous regions and contamination by implanted Ga-ions [61].

2.5.1 Slice and View

Slice and View is a special technique available only to an integrated FIB-SEM system. It is used to investigate a 3-dimensional volume with very high precision and high resolution in all directions. The technique is shown in Figure 2.17. The ion beam removes a predetermined section from the volume of interest and the electron beam acquires an image of the revealed face. The name of the technique originates from the ”slicing” of the ion beam and the ”viewing” of the electron beam. This is repeated until the entire volume of interest has been imaged. In order to use the ion beam and the electron beam at the same point, the sample must be at eucentric height. This is the height inside the sample chamber where the two beams meet. Prior to slice and view, in situ sample preparation is required. Software is used to reconstruct the 3-D volume from the images. Slice thickness together with image size (in pixels) and magnification determine the resulting resolution of the technique. However, due to both the random nature of electron motion in materials making the interaction volume greater than the probe size and SEM instrument limitations, there is a fundamental limit to the obtainable resolution.

2.6 Staining

Incorporating a heavy element into a sample by chemical or physical methods is called staining. The purpose is to gain backscatter contrast between regions where it otherwise would not be present. In FIB-SEM, the need for backscatter contrast is vital because flat surfaces milled by the ion beam are imaged. There are two main types of staining, positive and negative [63]. A positive stain will adsorb into the regions of interest through a chemical interaction or preferential absorption. A BSE image will show the area as bright compared to the background. When selective absorption is not possible, or if the chemical composition of different species in a sample are too similar, negative staining may be used. A negative stain will diffuse into a sample and ideally not react with any chemical species. Negative staining will make the background bright and for example filler particles in a matrix dark due to a lower concentration of stain in them. A negative stain can be made positive by washing the sample for an appropriate amount of time.

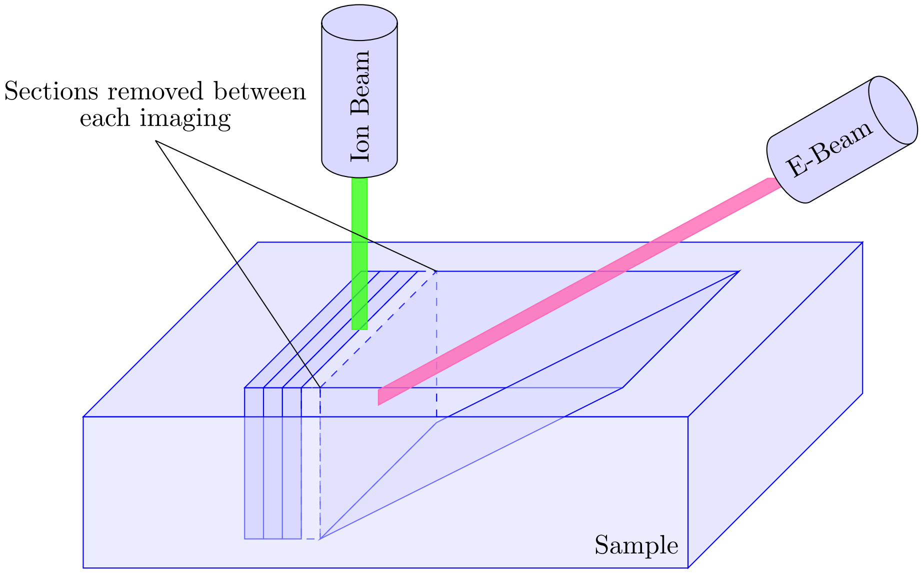

Figure 2.17: The basic principle of ”slice and view” with a FIB-SEM. First, the focused ion beam mills a large trench so the electron beam can image a cross-section. Subsequently, the ion beam removes small sections with pauses for imaging by the SEM. This technique can be used to create a 3-D model using computer software, or simply give qualitative cross-sectional information about a sample.

Staining has been common for investigating biological samples and some of these techniques have been modified to investigate polymers [42]. There is now a range of stains available for polymers depending on the chemical composition of the polymer, the instrument used for examination and which properties are being investigated.

Uranyl Acetate as a Stain

Uranium is the 92nd element in the periodic table making it very heavy and suitable for staining. It is used as both a positive and negative stain as uranyl acetate [63].

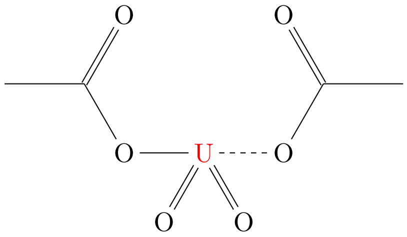

Figure 2.18: Structural formula of uranyl acetate dihydrate.

Staining by Ion-exchange

Ion exchange is a well-known phenomena where a solid material is able to take up ions from a solution and releasing an equivalent amount back in the solution. Mechanical or chemical treatments introduce negatively charge groups on the cellulose fibers/fibrils that have positively charge counter ions (X^+) to preserve charge neutrality [64]. These ions are free to exchange with other cations (M^+) in the surrounding solution by

$$M^+ + R^- X^+ \longleftrightarrow R^- M^+ X^+$$

where R is a functional group like carboxylic acid. If a heavy element is chosen as M^+, and successfully exchanged, the average atomic number of cellulose will increase significantly. The increased atomic number will increase the backscatter coefficient compared to unstained cellulose.

2.7 Reactive Ion Etching

Reactive ion etching (RIE) is a dry[6] etching technique that uses a chemically reactive plasma to remove material from a surface. A plasma is an ionized gaseous medium and can be created by applying an electric potential to a gas. The plasma may contain atoms, molecules, ions, electrons and different radicals depending on parameters such as gas mixture, gas flow, voltage bias, pressure etc. A variant of the RIEis the inductively-coupled plasma (ICP)-RIE. This setup has two voltage generators shown in Figure 2.19 as compared to only one in a regular RIE. The ICP generator strikes plasma in the gas mixture and the RF generator creates a bias which extracts and accelerates ions and radicals towards the sample surface.

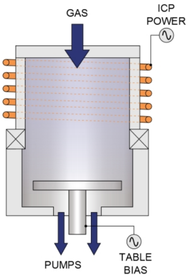

Figure 2.19: Schematic representation of an inductively-coupled plasma (ICP) reactive ion etcher (RIE). The ICP power regulates the plasma formation and hence its density. The table bias, or in some cases called the RF generator, determines the energy of the plasma striking the surface.

Material can be removed from a surface physically or chemically as seen in Figure 2.20. Both processes may occur at the same time. Physical etching, also known as sputtering, has been covered in Chapter 2.5. An additional note must be made of the anisotropic nature of physical etching due to the incident angle of ions on the surface. Chemical etching occurs because radicals in the plasma react with surface atoms and molecules and create volatile products that are pumped away by the vacuum system. Because this process relies on chemical reactions, it can be much more selective towards which material on a surface is etched. Sputtering does not have this property. However, chemical etching is generally equal in all directions.

---

[6] Etchant not in liquid phase.

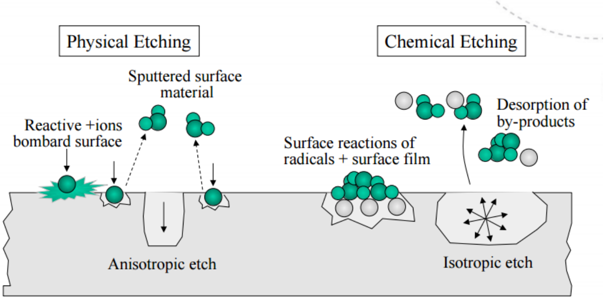

Figure 2.20: The difference between physical and chemical etching. The physical method relies on the kinetic energy of positive ions to bombard the surface and dislodge atoms. Chemical etching employs a reactive plasma of radicals that adsorb on the surface and chemically react with the substrate. The product(s) desorb whereby removing atoms from the surface. Figure 16.12 adapted from [65].

2.7.1 Fluoride-Polymer interactions

Plasma chemistry and its interactions with a polymer surface are complex. This is because many different chemical species exist in a plasma and each one can interact with each other and a surface in a number of ways. To simplify matters, in a fluoride containing gas like SF_6, the chemically active species will be regarded as the fluorine radical, $F^\bullet$. In reality, the discharge contains a large number of ions and radicals [66].

Energy is transferred from the plasma to a solid through optical radiation (only UV spectrum is of interest to polymers as other wavelengths are weakly absorbed), fluxes of neutral particles and ionic particles [32]. High-energy particles and UV-radiation in the discharge can dissociate bonds in the polymer as well (also called chain scissioning). C-C and C-H bonds can be broken creating volatile species that desorb from the surface. Preferential bond breaking is not possible as the bond strength are so closely related (370 kJ/mol for CH3-CH3 and 435 kJ/mol for H-CH3 for example) [67]. Equation 2.11a shows hydrogen abstraction by a fluorine radical. This creates a highly reactive dangling bond on the polymer and is the primary etching mechanism for saturated polymers [68]. Equation 2.11b shows fluorine addition. This addition may passivate the surface and cause resistance to further etching. Substitution of radical groups is an exothermic reaction and happens spontaneously. The heat produced can cause thermally-initiated chain scissioning [67]. The addition of fluorine weakens the other bonds of the carbon because it is significantly more electronegative than carbon and promotes further addition.

$$\mathrm{F}^\bullet + \mathrm{R{-}H} \longrightarrow \mathrm{F{-}H} + \mathrm{R}^\bullet \tag{2.11a}$$

$$\mathrm{R}^\bullet + \mathrm{F_2} \longrightarrow \mathrm{F{-}R} + \mathrm{F}^\bullet \tag{2.11b}$$

Chapter 3

Materials and Methods

3.1 Materials

Polyvinyl alcohol was purchased from Sigma-Aldrich (CAS-number 9002-89-5). It had a weight average molecular weight of 89 000 - 124 000 g/mol and was 89% hydrolyzed. Cellulose nanocrystals were purchased from the University of Maine [69]. They are produced from wood pulp by sulfuric acid hydrolysis. The resulting particles were rod-like with approximate diameter of 5 nm and 150-200 nm long. Cellulose nanofibrils were made from lignocellulosic mass purchased from Norsk Skog Saugbrugs.

3.1.1 TEMPO-Oxidation and Homogenization of Cellulose Mass

The lignocellulosic (LC) mass was oxidized at room temperature with 99% TEMPO (Sigma Aldrich CAS: 2564-83-2), sodium bromide and sodium hypochlorite. A solution of 0.0125g/g LC mass TEMPO and 0.125g/g LC mass NaBr was prepared in deionized water and added to a given amount of mass that had been stirred for 10 minutes. The resulting solution was diluted to 1.33 vol% and stirred for another 5 minutes. Oxidation was done by adding 0.0127 mol NaClO once per minute. pH was maintained at 10.5 by addding NaOH. The reaction was deemed complete when the pH remained unchanged for 10 minutes. Then, the solution was adjusted to pH 7 by 0.5M HCl. The final mass was vacuum filtered and repeatedly washed with deionized water until conductivity was below

5 µS/cm.

Homogenization was done using a Rannie 15 type 12.56X homogenizer (APV, SPX Flow Technology, Silkeborg, Denmark), with one pass at 600 bar, followed by another pass at 1000 bar. The mass had been diluted to 0.8 wt % prior to homogenization. Viscosity measurements indicated an approximate diameter of 15 nm and length of 200 nm. TEMPO-oxidation and homogenization was not done by the author.

3.1.2 Preparation of PVA/Nanocellulose films

Films were made by cast-evaporation in a perti dish. PVA solutions were made by adding 3 wt% PVA to deionized water while stirring. The solution was put in a heat cabinet at 90° for 3h followed by 24h on a roller. Then, the solution was filtered through a 5 µm filter using a syringe.

Nanocellulose (if applicable) was added in appropriate amounts to de-ionized water. The solution was stirred until it appeared homogeneous, approximately 10-20 mins. To get the desired film density, approximately 60 mL of solution was added to a petri dish. The dish was left to dry in room temperature without a lid until all the solvent had evaporated (This takes approximately one-two weeks).

Preparation of Si-wafer for PVA film

Polyvinyl alcohol (PVA) films were also made on silicon wafers. A silicon wafer was chosen as it is known to be atomically flat [70]. A 2 inch Si-wafer was washed with ethanol. As this was a preliminary study, the wafer was not plasma cleaned to remove any organic contamination as it was not deemed necessary. The wafer was put in a vacuum desiccator with 100% silane (1H,1H,2H,2H-perfluorooctyltriethoxysilane) solution. Silane groups bond well to the silicon surface and have long, fluorinated tails which exhibit low surface energy [71]. This will reduce the adhesion between the film and the wafer. The desiccator was pumped for 15 minutes to achieve vacuum, turned off and left for 1 hour with the silane solution. Silane evaporates inside the desiccator and forms a thin layer on the surface of the wafer. The exact pressure was not known because there was no pressure gauge. The wafer was then put in a petri dish and a PVA film was made on it by the previously described procedure.

Table 3.1: Summary of sample names of the different film compositions characterized.

Sample name	*Film Composition*	*Cellulose content in weight percent of PVA*	*Note*
PVAf	PVA	-	
0.5CNC		0.5% CNC	
4CNC		4% CNC	
0.5CNF		0.5% CNF	
4CNF		4% CNF	
Cs-stained		4% Cs-stained TEMPO-cellulose	Made with Cs-stained cellulose by protocol 2
CNC	100% CNC		
CNF/Cs-stained	50% CNF/ 50% Cs-stained TEMPO-cellulose		Made with Cs-stained cellulose by protocol 1
Teflon-PVA	PVA		Film made on top of silicon wafer
Si-PVA	PVA		Film made in teflon petri dish

3.1.3 Preparation of Cellulose Nanocrystal films

A solution was made with approximately 3 wt% cellulose nanocrystals (CNC). The solution was adjusted to pH 9 with 0.05M NaOH and stirred overnight at 800 rpm. 50g of the solution was poured into a petri dish and dried at room temperature.

3.1.4 Sample Preparation

Ion-exchange with Cesium

Unfibrillated[1] TEMPO-oxidized cellulose was used for ion exchanging Na^+ counter ions with Cs^+. Cs was chosen based on its affinity for the carboxylic acid group [72]. The affinity of various counter ions was as follows: $H^+ > Zn^+ > Ca^+ > Mg^+ > Cs^+ > K^+$ Na^+. Cs is monovalent so it would not induced agglomeration of cellulose and a heavy element that will give sufficient compositional contrast. Ion exchange was done by two different protocol.

Protocol 1 was made by adjusted a solution of TEMPO-cellulose to pH 9 with NaOH. 0.1 M CsCl was added in a molar ratio 2:1 between Cs og acid groups. The solution was stirred for approximately 4 hours and washed on filter paper with deionized water until the conductivity was below 5 µS/cm.

Protocol 2 was made by adding 5.74g of TEMPO-cellulose (dry mass) to 1000g of deionized water and run for 10 000 revolutions in a disintegrator to straighten out fibers. CsCl was added to the solution in a molar ratio of approximately 60:1 between Cs^+ and carboxylate groups [73]. The solution was stirred mechanically (with drill and magnet stirrer) for 6.5 h and washed on filter paper with deionized water until the conductivity was below 5 µS/cm.

Uranyl Acetate staining

PVA films with and without nanocellulose were stained with uranyl acetate (UA) at the Cellular and Molecular Imaging Core Facility at St. Olav's Hospital. A 1% UA solution in 87.5% ethanol and 12.5% water was centrifuged at 10 000 rpm for 10 minutes. A large droplet of the solution was placed on a parafilm in a dish and each sample (2 x 2 mm) was placed into the droplet for two or ten minutes. The samples were removed and filter paper was used to gently swab away residual solution followed by air drying for 5 minutes.

---

[1] Cellulose that has not been exposed to mechanical methods.

After examining samples stained by the first protocol, a modified version was also used. PVAf, 4CNC and 4CNF samples were stained in 0.2 ml test tubes. Each type of film was stained for 10, 20 and 30 minutes in 100 µl 1% (in 87.5% ethanol and 12.5% water) and 2% UA (in 75% ethanol and 25% water). After soaking for the designated duration, the UA solution was removed from the test tube and air dried.

Freeze-drying in Liquid Ethane and Liquid Nitrogen

Samples that were kept at 95% relative humidity and 23°C for 24 hours were freeze-dried with the setup shown in Figure 3.1. The freezing vessel (3 in Figure 3.1) was filled up about half way with liquid nitrogen. Gaseous ethane was introduced from a gas canister (2) into the metal rectangular prism (5) in the center of the vessel. Due to the temperature in the prism, the gaseous ethane solidified and a gentle tap provided enough energy to liquefy the ethane. One sample at a time was submerged into the liquid ethane using a sample holder (6) for approximately 10 seconds. The sample was immediately transferred to the sample holders for vacuum drying (4) which had been kept full with liquid nitrogen. When freezing several samples, the sample holders were continuously filled with liquid nitrogen as it evaporated. The sample holders were inserted into the vacuum drying vessel (1) and left there for 24 hours. The vacuum pressure was unknown as there was no pressure gauge. Samples were then kept in a desiccator until characterized.

Samples frozen in liquid nitrogen were submerged in nitrogen for approximately 10 seconds held by a pair of tweezers and placed in the sample holder for vacuum drying and vacuum dried with the same procedure as liquid ethane freezing.

3.2 Methods

SEM characterization was done on two field-emission microscopes, a Zeiss Supra 55 VP and a Hitachi S-5500. Samples were either sputter coated with 5 nm of Pt/Pd (80%/20%) with a Cressington 208 HR B sputter coater or left uncoated depending on what was being investigated. The samples were mounted on holders using carbon or copper tape. When cross-sections were investigated using FE-SEM, the samples were freeze fractured in liquid nitrogen (LN-fracturing) prior to being coated and mounted.

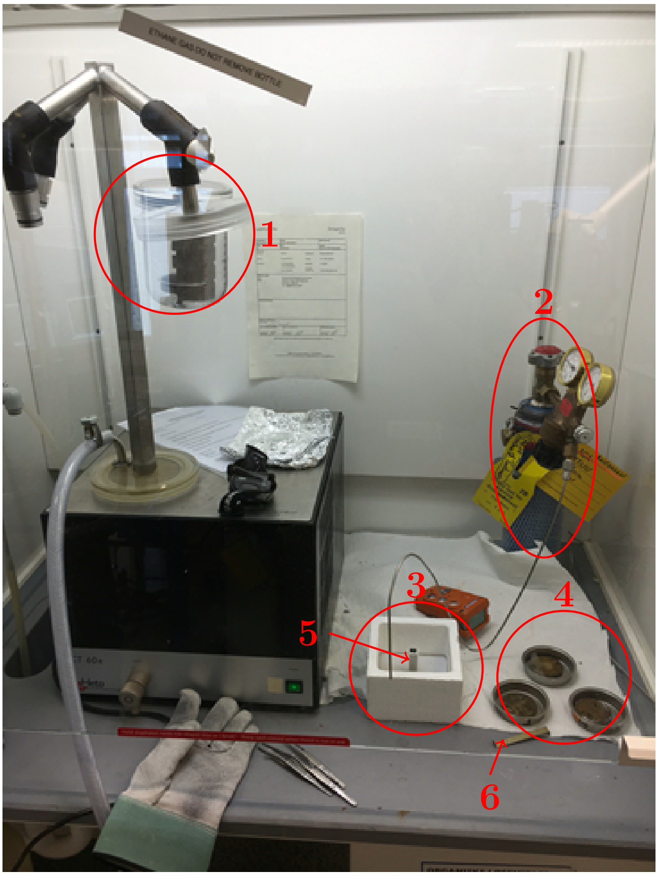

Figure 3.1: Experimental setup for freeze-drying samples in liquid ethane and liquid nitrogen. 1. Vacuum-drying vessel 2.Gas canister with ethane 3. Freezing vessel 4. Sample holders for vacuum drying 5. Liquid ethane vessel 6. Sample holder for freezing.

3.2.1 FIB-SEM

FIB-SEM was done on a Helios NanoLab DualBeam from FEI. Samples were mounted on a sample holder with carbon or copper tape and sputter coated with 10 nm of Pt/Pd (80/20) in a Cressington 208 HR B sputter coater. In the instrument chamber, the sample was positioned at eucentric height (Figure 3.2A) which is at a working distance of 4.1 mm. A "horse-shoe" pattern was milled into the film with the ion beam using an acceleration voltage of 30 kV (unchanged for all experiments) and a beam current of 0.92 nA (Figure 3.2B). The shape was made using two rectangular milling patterns and one cross-section pattern. The cross-section was cleaned with consecutively lower beam currents. FEI's Auto Slice and View software was used to perform slice and view. The software mills a fiduciary mark to use as a reference point which is shown in Figure 3.2C. Before each section was milled, an ion image is captured where the mark is used for alignment.

3.2.2 Reactive Ion Etching

Polymer film etching was performed on a Plasmalab System 100 RIE from Oxford Instruments which is an *inductively-coupled plasma* (ICP) RIE. Samples were placed on a 20.3 cm diameter (8 inch) sapphire wafer on the RF electrode. Fomblin oil was used between the wafer and the sample to improve heat conduction. The RF power was set to 25 W and the ICP generator to 250 W. The etching was performed with Ar (25 sccm[2]) and SF_6 (10 sccm) for a designated duration.

Table 3.2: Samples etched with SF_6/Ar gas mixture from the top side and bottom side of the film.

Sample name	*1 minute, 30 seconds etch*	*3 minute etch*
2PVA	✓	
4CNC	✓	✓
4CNF	✓	✓
Si-PVA	✓	
Teflon-PVA	✓	

† Insert

---

[2] Standard cubic centimeters per minute

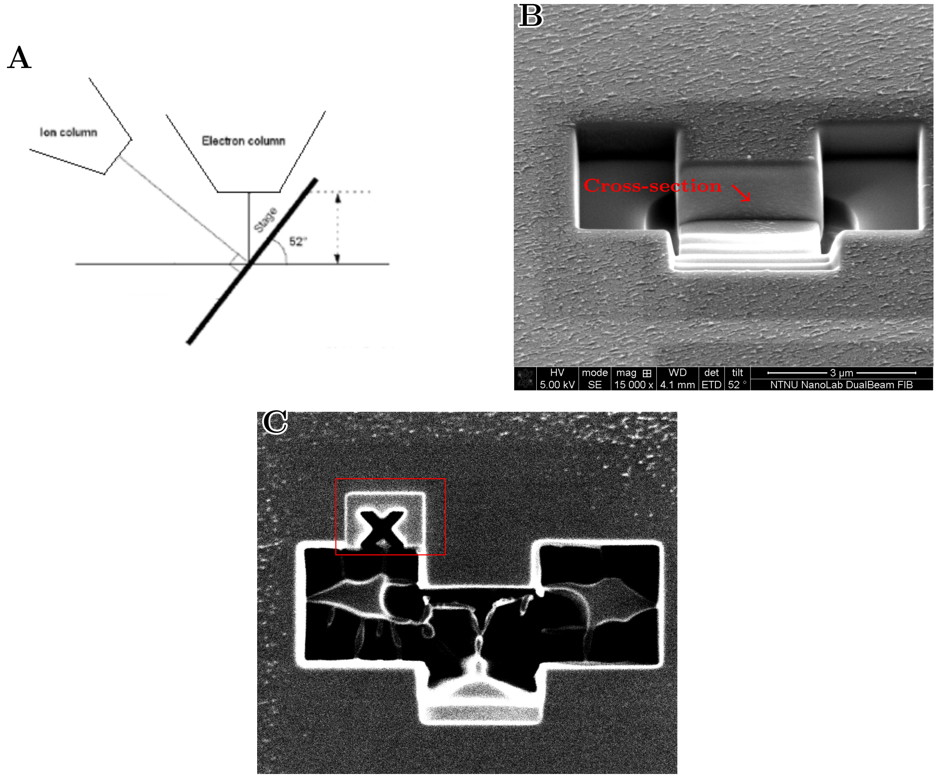

Figure 3.2: A. The eucentric height in a FIB-SEM is the height that the ion beam and electron beam intersect. This allows the beams to be used at the same point on the sample. It is measured from in distance from the electron column and is 4.1 mm in the FIB-SEM used in this work. B. Example of the milling pattern used to examine cross-sections with FIB-SEM. A cross-section pattern was milled with desired width, height and depth. Two trenches were milled on both sides of the cross-section with rectangular pattern. The purpose of the trenches is to increase the signal from the cross-section face and limit redeposition of milled material. C. A fiduciary mark is milled by the slice and view software for alignment before each slice is milled. The mark is the cross in the red square.

Etch rate measurements

Samples were put on a sapphire wafer with fomblin oil. Half the sample was covered with polyamide tape, but the tape was only adhered to the surface of the wafer, not the sample. The sample was etched as described above and the tape removed. Etch depth was then measured as the height difference between the etched and unetched area with a Dektak 150 profilometer from Veeco. The etch rate was calculated by dividing etch depth with etch duration. CNC and PVA films were used to measure etch rates.

3.3 Software

The software used throughout the work is presented below with specification of the method and function of various tools used.

3.3.1 Monte Carlo Simulations

Casino v3.2.0.4 was used for Monte Carlo Simulations [74–77]. The software is developed for studying electron trajectories in solids. The Monte Carlo method uses randomly generated numbers to predict the magnitude of certain events. In the case of simulating electron trajectories, several key parameters determining its trajectory are gotten by random numbers [55]. These parameters are for example mean free path (Equation 2.2) and the scattering angle (ϕ from Equation 2.3). The probability of an electron traveling a distance s is

$$p(s) = exp(-s/\lambda). \tag{3.1}$$

where λ is the mean free path. The distance an electron travels before scattering, called the step length, is then gotten by

$$step = -\lambda \; log_e(RND) \tag{3.2}$$

where RND is a randomly generated number. This is done over and over until the energy of the electron has reached 50 eV because backscattered electrons (BSE) are being simulated, or the electron escapes through a surface. One such trajectory will not represent a ”real” trajectory. However, averaging many such trajectories will give a good understanding of reality.

PVA and cellulose nanofibrils (CNF) were simulated separately to determine BSE coefficients and depths. First, the desired material was made in the program by making a cube with sides of 1 µm and assigning material parameters as shown in Figure 3.3. The parameters specified in the software are listed in Table 3.3.

Table 3.3: Material parameters used when simulating backscatter coefficients and depths in Casino.

Material	*Chemical formula*	*Density*
polvinyl alcohol	C_2H_4O	1.25 g/cm^3
TEMPO-cellulose nanofibrils	$C_6H_{10}O_5Na_{0.1}$†	1.55 g/cm^3

† Weight fractions were specified as 0.4307 (C), 0.059 (H), 0.4913 (O) and 0.019 (Na).

Then, the number of simulated electrons was set to 40 000 to get an appreciable number of data points. The incident beam probe size was set to 1 nm which is a low, but obtainable probe size for a field emission (FE) source [78]. The simulation tracks electron trajectories and formats them into various distributions and data sets. A graphical output is shown in Figure 3.4. The blue cube is PVA irradiated by an incident electron beam (blue vertical line) and the trajectories of escaped BSE are shown as red lines. Note that only a small fraction of the trajectories are displayed.

3.3.2 FIJI

FIJI was used for segmentation and cross-sectional analysis [79, 80]. When applicable, the menu selections in FIJI are specified in parenthesis. Segmentation was done prior to making 3D models of slice and view experiments. More sophisticated segmentation software is available, but the limited use made FIJI the preferred choice. Sequential images were put into stacks (Image > Stacks > Images to Stack) and sections outside the area of interest cropped out. The threshold (Image > Adjust > Threshold) was adjusted manually to make regions of interest white and the background black.

Concentration profiles of nanocellulose near the top and bottom surface of cross-sections were done in FIJI. An area of 400 x 400 pixels^2 (2.78 x 2.78 µm^2) was selected at the edge of the cross-section in each image. The contrast of selected area was enhanced (Process > Enhance Contrast) with default settings. Mosaic particle tracker 2D/3D plugin in FIJI was used to identify nanocellulose in the images. This plugin was used instead of segmentation as it was superior in identi-

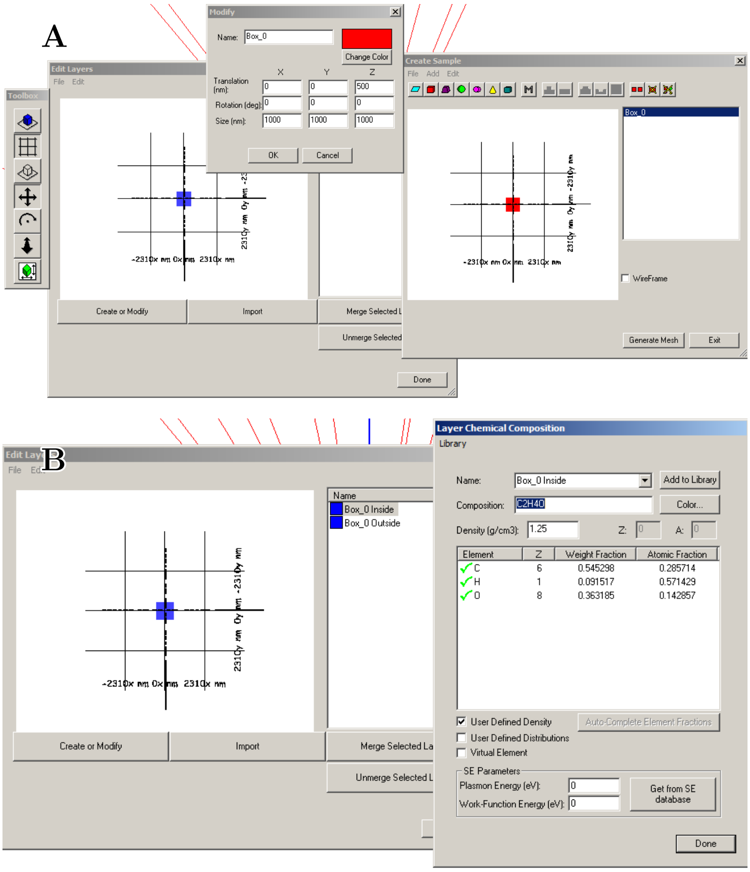

Name: Box_0

	X	Y	Z
Translation (nm):	0	0	500
Rotation (deg):	0	0	0
Size (nm):	1000	1000	1000

Name: Box_0 Inside

Composition: C2H4O

Density (g/cm3): 1.25   Z: 0   A: 0

Element	Z	Weight Fraction	Atomic Fraction
✓ C	6	0.545298	0.285714
✓ H	1	0.091517	0.571429
✓ O	8	0.363185	0.142857

☑ User Defined Density

☐ User Defined Distributions

☐ Virtual Element

SE Parameters

Plasmon Energy (eV): 0

Work-Function Energy (eV): 0

Figure 3.3: Interface in Casino used to set up the desired material and its properties. A. The size and shape of the material is input. Both PVA and nanocellulose were made as 1x1x1 µm boxes positioned with their surface at 0,0,0 in the software coordinate system. B. Material properties are assigned to each material made in A. PVA shown in the image is simply entered as its chemical formula. The density was entered manually.

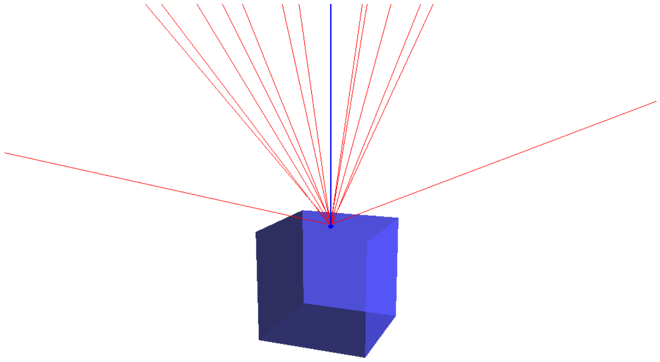

Figure 3.4: A graphical representation of simulation of BSE using Casino. The blue vertical line is the incident electron beam, the blue cube is PVA and the red lines are a small fraction of the escaped BSE trajectories.

fying nanocellulose. Each image that was processed was binned[3] into 30 equally sized bins representing a depth interval in the film. The number of particles identified in each bin was assigned as the number of nanocellulose observed at the bin depth.

3.3.3 Avizo

Avizo v8.0.1 is a commercial software application developed by FEI for scientific data analysis. It was used to make three dimensional volume representations of consecutive scanning electron microscope (SEM) images from FIB-SEM. The images were imported into the software already segmented by the method described above. The size of each voxel was specified for the software to know the dimension of the images and the distance between each image. The y-direction must be corrected for the angel of observation by scaling the observed length by 1.27.

---

[3] Data binning is a method for grouping more or less continuous values into one value for each bin.

Chapter 4

Results

The objective of this thesis was to characterize the structure of polyvinyl alcohol (PVA) films with nanocellulose. The films are intended as the active layer in a membrane for CO_2 gas separation. The desire to understand nanocellulose distribution in PVA stems from their primary function in the membrane to retain water. Water is vital to the operation of the membrane as it reacts with CO_2 and promotes its transport across the membrane. Therefore, an even distribution of nanocellulose in PVA both laterally and vertically is desired.

Characterization was first done by cross-sectional SEM which is the established method in the PVA/nanocelluse composite field [21–24]. The cross-sections were made by fracturing samples in liquid nitrogen. Work done by the author during the project thesis indicated that this type of fracturing creates highly variable cross-sections [1]. However, it was done on samples where the active layer thickness was approximately 1 µm thick. The literature shows many examples were freeze-fracturing makes nanocelluose identifiable in SEM cross-sections [21–24]. The information obtainable from these SEM micrograph are limited.

4.1 Cross-sectional Characterization

A common way to investigate the distribution of a filler in a composite, in this case nanocellulose in PVA, is to examine a cross-section. The cross-section must be made in such way as to not produce artifacts in the size-range of the filler particles. Nanocellulose is quite small and may therefore be challenging to characterize accurately in a cross-section. Before exploring novel characterization methods on this material system, a thorough understanding of the benefits and limitations of existing methods is important. PVA films with different nanocellulose weight percent and type were prepared as described in Chapter 3.1.2. Cross-sections of PVA, 0.5CNC, 0.5CNF, 4CNC and 4CNF were made by LN-fracturing and characterized by FE-SEM at 3kV acceleration voltage. All samples were coated with 5 nm Pt/Pd. Figure 4.1 shows a cross-section of typical PVA/nanocellulose film with a magnified image of the cross-section close to the surface. Most cross-sections made by LN-fracturing produced smooth areas and rough areas on the micrometer scale. The area in the cross-section close to the film surface were consistently the roughest. There were sections towards the center that also appeared rough, but flat and smooth cross-section a few micrometers from the surface was rarely seen.

More micrographs were taken to identify the appearance of nanocellulose in cross-sections. For the method to be usable, nanocellulose must be reliably identifiable in cross-sections. Cross-sections of PVAf, 0.5CNC and 4CNC are shown in Figure 4.2 and 4.3 respectively. White dots were seen in the cross-sections of 0.5CNC and 4CNC samples, but not PVAf. The concentration of dots appeared to increase from 0.5CNC to 4CNC. It was also of interest to determine if there was a difference between cellulose nanocrystals (CNC) and cellulose nanofibrils (CNF) as both are candidates for use in polymeric membranes. The micropgrahs in Figure 4.4 showed that CNC and CNF look similar when characterized by FE-SEM. Cross-sections of films containing CNF did however show some larger white dots that were not generally seen in CNC films. When increasing the magnification, somewhat darker dots also became visible in addition to the bright dots.

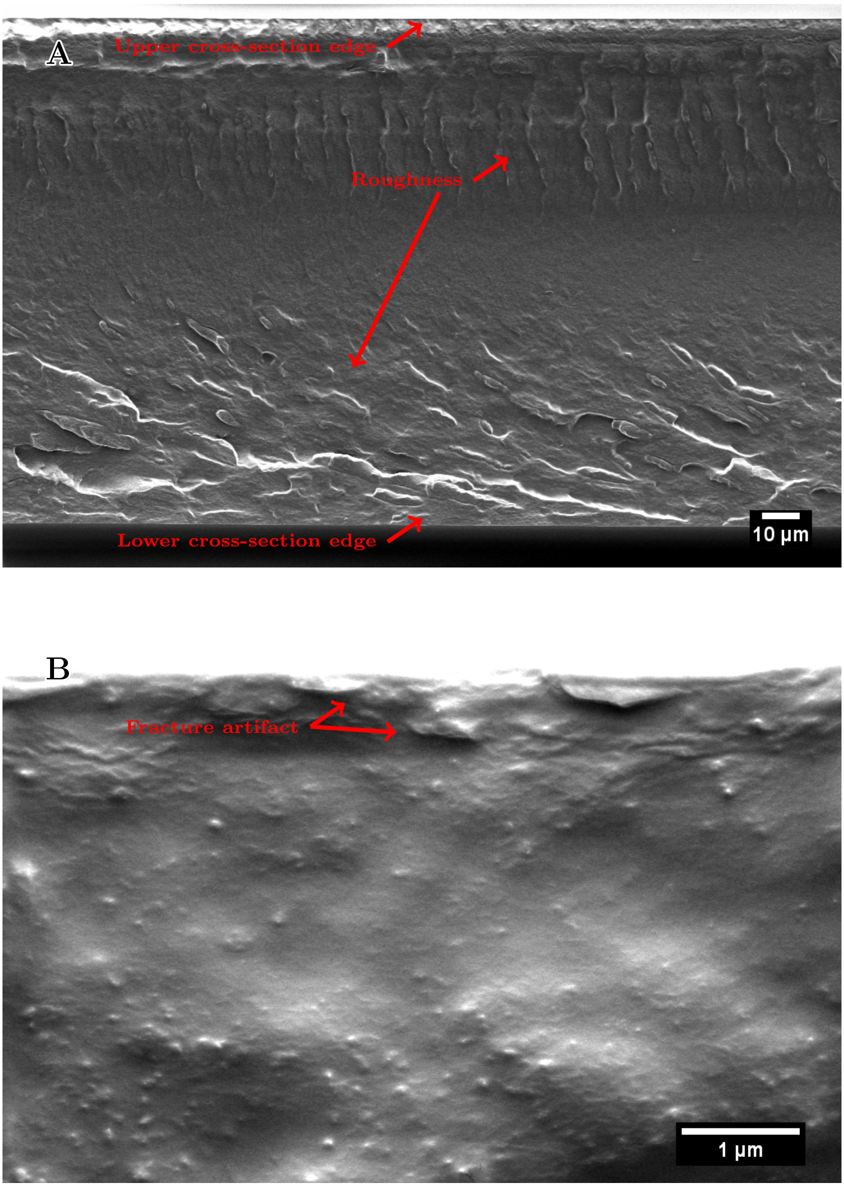

Figure 4.1: Cross-sections of 4CNC prepared by LN-fracturing and imaged at 3 kV with 5 nm Pt/Pd layer. A. Generally, cross-section prepared by this method had smooth and flat sections towards the center of the film. Closer to the edges, micrometer roughness appeared (arrows). The exact appearence of the roughness was different for each fractured cross-section. B. High-magnification images close to the surface showed an uneven and severely disorder cross-section (arrows) within two micrometers of the surface.

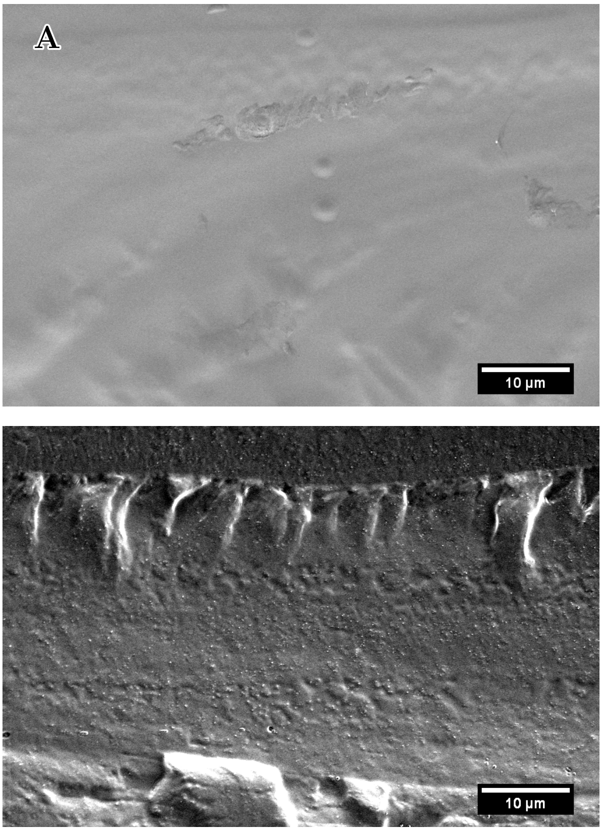

Figure 4.2: Cross-section prepared by LN-fracturing of PVAf (A) and 0.5CNC (B). The surface of A appeared generally smooth with no white dots visible. The surface of B showed many bright white features.

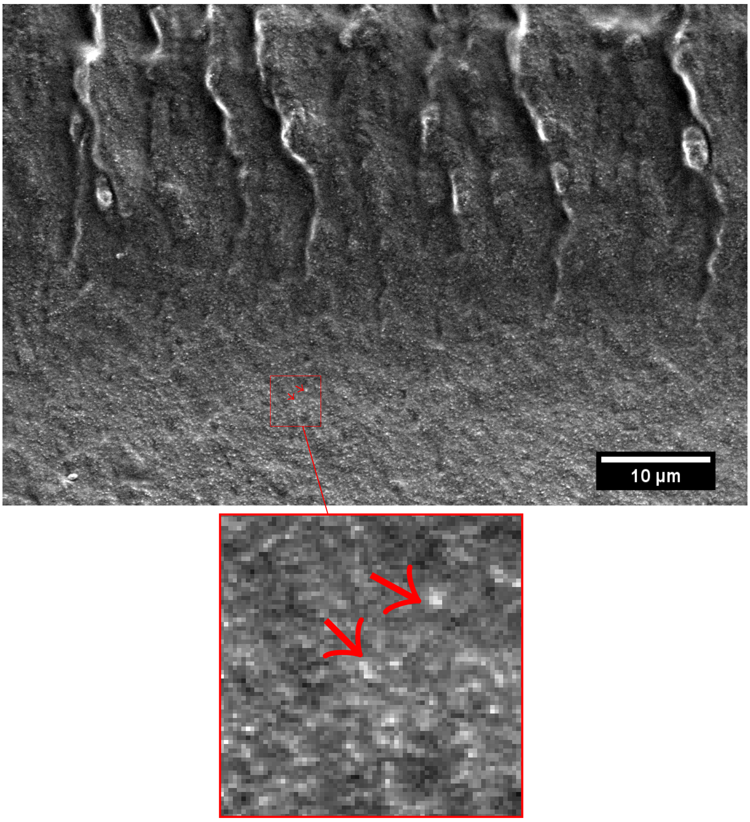

Figure 4.3: Cross-sections prepared by LN-fracturing of 4CNC. The large scale roughness was the same as seen in Figure 4.1. The magnified area shows the white dots observed in the cross-section (arrows). They appeared evenly distributed. The dots were not visible in PVAf in Figure **??**A.

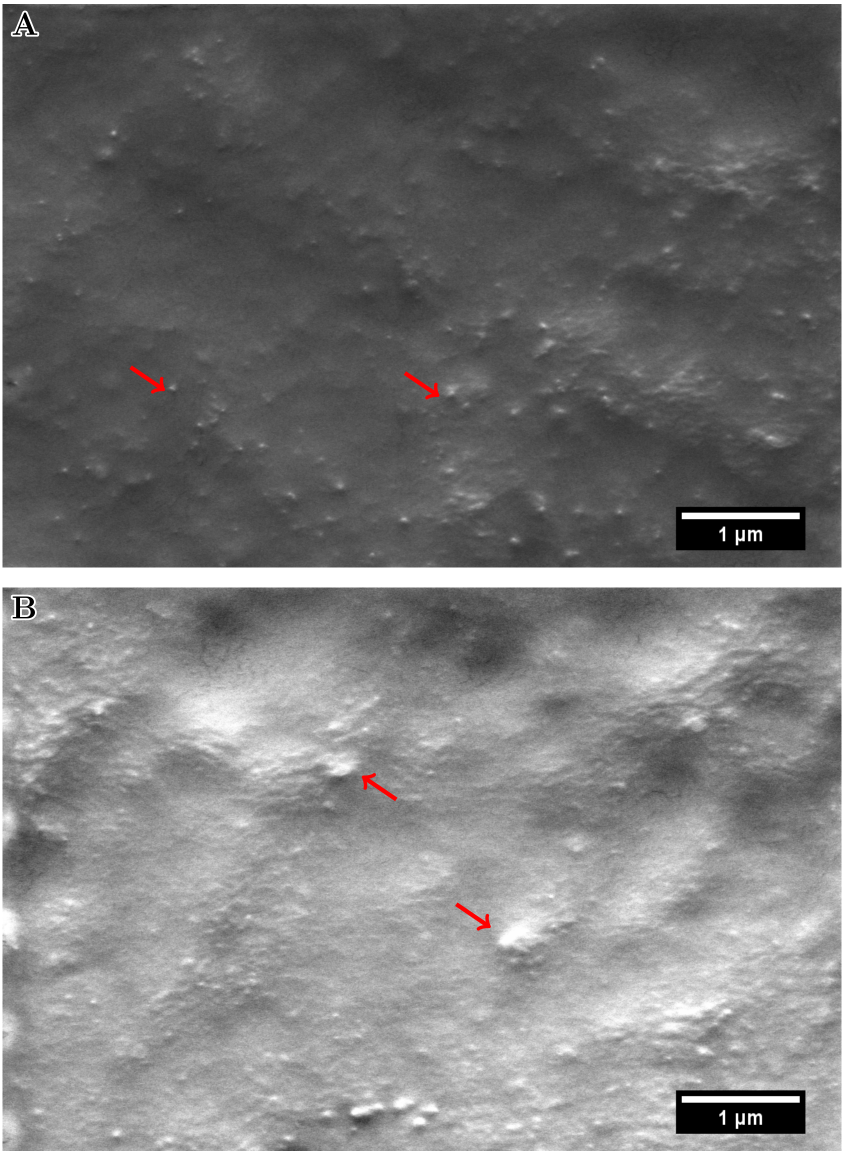

Figure 4.4: LN-fractured cross-sections of A. 4CNC and B. 4CNF. The smaller white dots indicated by arrows in A, also shown in Figure 4.3, were seen in both cross-section. Additional dots that were somewhat darker became visible at higher magnification. Micrographs of CNF films often showed some larger dots, indicated by arrows in B, that were generally not seen in CNC films.

After evaluating the results of the previous images, the next step was to characterize the distribution of nanocellulose. An even distribution of nanocellulose is key because it is directly related to membrane performance, both mechanically and chemically. From a purely qualitative viewpoint, this was done by looking at micrographs taken across the whole film thickness. Sequential, overlapping micrograhps were taken across the entire film in the lateral direction of 4CNC and put together in a composite image, also called mosaic. A mosaic is shown in Figure 4.5 where nearly the entire cross-section is shown. The white dots appeared evenly distributed throughout the entire mosaic.

Capturing higher magnification micrographs near the top and bottom of the films can reveal any segregation effects arising during drying. Therefore, micrographs taken at these points were examined. Figure 4.6 shows that there appeared to be a difference in nanocellulose particle concentration between the top and bottom of cross-sections. Also, there appeared to be a lack of nanocellulose particles near the edge of the cross-sections. However, this was based on purely qualitative assessments.

In order to further examine the possibility of segregation, a quantitative method was developed. Micrographs were taken at the top and bottom surface of 4 wt% CNC and CNF films. The method described in Chapter 3.3.2 was used to identify and quantify nanocellulose particles in the cross-section. Based on the results, concentration profiles of two bottom surfaces and one top surface from each type of film were made. Figure 4.7 shows CNF profiles and Figure 4.8 shows CNC profiles. There was observed no significant difference between top and bottom surfaces. The method did appear to consistently recognize more CNF than CNC.

The total number nanocellulose particles identified per area was also calculated in Table 4.1. This was also done for two micrographs taken from the center of the film in addition to the top and bottom surface. The results showed that there appeared to be an increasing concentration in identified nanocellulose from the top to the bottom. This difference was large for CNF, but less pronounced for CNC.

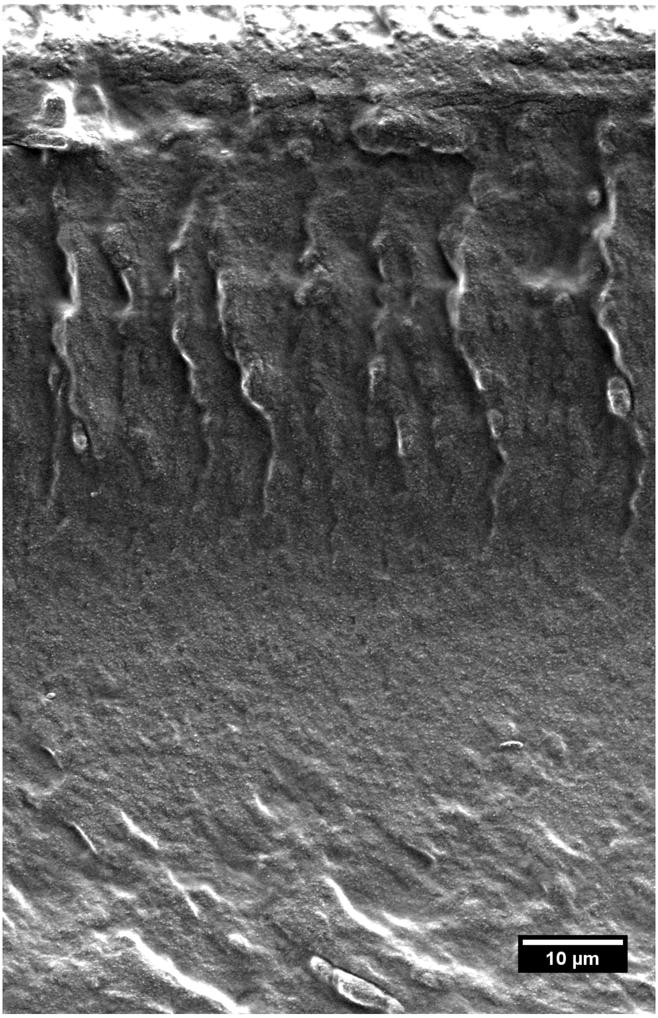

Figure 4.5: Mosaic of 4% CNC film made from four images put together. The white dots appeared homogeneously distributed throughout the film at this magnification.

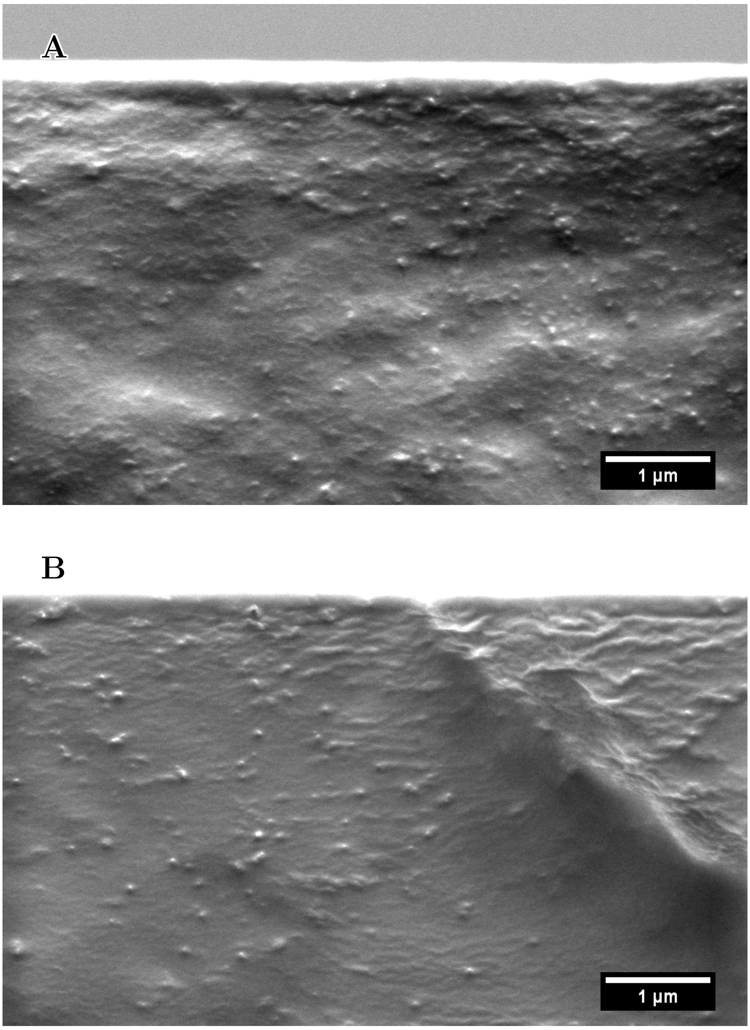

Figure 4.6: SEM micrographs taken at the bottom (A) and top (B) edge of the cross-section of a 4CNC film. The concentration of CNC particles (white dots) believed to be seen in A appeared to be higher than in B. This was observed as a general trend for both CNC and CNF films. Note that B has been rotated for easier comparison to A.

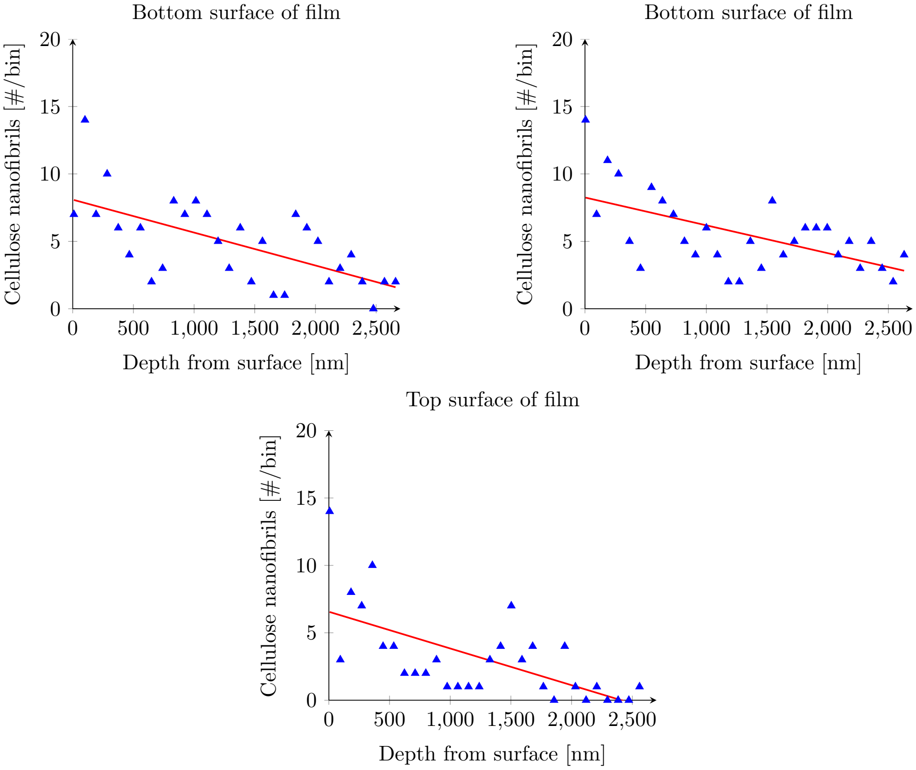

Figure 4.7: Concentration profiles from top and bottom surface of a PVA film with 4 wt% CNF. Each blue value corresponds to the number of CNF recognized in each bin. One bin had an area of approximately 0.25 µm^2. The red line is the regression line for each data set.

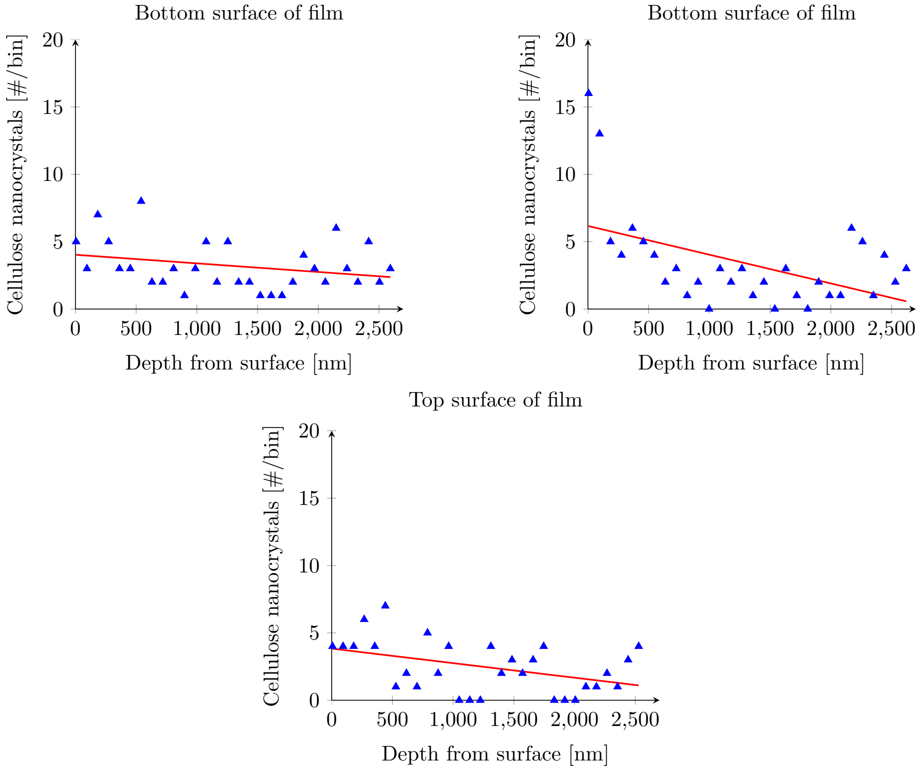

Figure 4.8: Concentration profiles from top and bottom surface of a PVA film with 4 wt% CNC.Each blue value corresponds to the number of CNF recognized in each bin. One bin had an area of approximately 0.25 µm^2. The red line is the regression line for each data set.

Table 4.1: The number of nanocellulose per area for 4CNC and 4CNF. The values were calculated from nanocellulose identified by the FIJI plug-in Mosaic particle tracker (details in Chapter 3.3.2). A segregation effect was seen for both types of nanocellulose, but was considerably larger for CNF.

Surface	*CNC/area (#/μm^2)*	*CNF/area (#/μm^2)*
Top	9.5904†	11.9232†
Middle	9.9792	15.7464
Bottom	12.7656	20.1528

† Value calculated from only one image.

4.2 Low-Voltage SEM imaging

Backscattered electrons (BSE) give compositional contrast as covered in Chapter 2.4.2. Surface or cross-section features make distuguishing between nanocellulose and artifacts challenging. If compositional contrast can be used, nanocellulose and PVA will more easily be told apart. Therefore, Monte Carlo simulations were done in order to determine if and how much contrast is achievable. Another challenge is imaging non-conductive surfaces. The simplest remedy is a thin metal coating. However, it is difficult to see the difference between metal layer artifacts and film surface features. Therefore, imaging PVA/nanocellulose films uncoated is desirable. In addition, FIB-SEM exposes a new and uncoated cross-sections during regular milling and slice and view. Finding parameters like beam current, acceleration voltage and image-capture settings enabling uncoated imaging of PVA/nanocellulose films is important. As explained in Chapter 2.4.4, low-voltage SEM is ideal for overcoming charging effects that arise from irradiating non conductive samples. Uncoated imaging may also be desirable for RIE characterization if a layer by layer investigation is possible. Before uncoated LVSEM was attempted, a theoretical approach with Monte Carlo simulations and semi-empirical equations were used to find a starting point for acceleration voltage. Then followed a practical approach with uncoated samples in LVSEM to determine more specific values of beam current, acceleration voltage and image-capture settings.

4.2.1 Theoretical approach with Monte Carlo Simulations

Achievable contrast in LVSEM

Casino was used to simulate PVA and TEMPO-CNF undergoing electron irradiaiton. PVA and TEMPO-CNF were simulated separately to get the values from each material. The simulation output directly gave BSE coefficients and they are plotted in Figure 4.9. Each data point was the result of 5 simulations from which an average and a standard deviation was calculated. Backscatter coefficients alone do not indicate if there will be contrast between two components. Therefore, the contrast, as defined by Equation 2.9, was also calculated. Contrast below 0.10 (10%) is considered difficult to see [52]. The calculations showed that, although coefficients were small and similar in value, contrast in the entire LVSEM regime should be sufficient between PVA and CNF. When imaging non-conductive samples, it is common to apply a thin metal coating to prevent charging as explained in Chapter 2.4.4. Casino can simulate any material, so a 5 nm metal layer of Pt/Pd (80/20 wt%) was added on top of PVA and TEMPO-CNF. BSE coefficients and the resulting contrast is in Figure 4.10. The coefficients became much larger, and stayed relatively equal as in Figure 4.9. However, the contrast became very low.

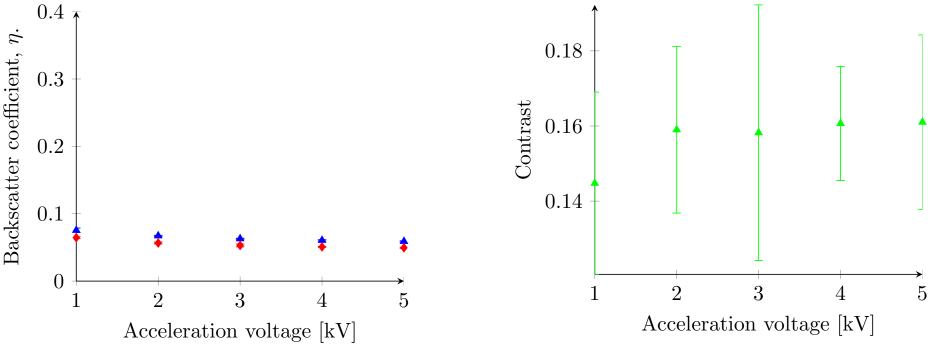

Figure 4.9: Simulated backscatter coefficients (TEMPO-oxidized nanocellulose (▲) and PVA(◆) and the contrast (▲) between TEMPO-oxidized nanocellulose and PVA. Casino was used to simulate the interaction of an electron beam with PVA and TEMPO-CNF by Monte Carlo methods. The number of BSE that escape through the surface are counted and the coefficent is calculated by Equation 2.4 automatically. The contrast was calculated by Equation 2.9. The standard deviations were calculated from 5 independent simulations.

Interaction volume

Simulations to determine the depth of BSE and the surface radius around the beam point from which they escape were also done. These two values will give an indication of the interaction volume. Casino results gave the normalized count of BSE from each picometer-size depth interval. The count is the number of electrons that the detector detects and these counts are normalized so the total sums up to one. In order to not have the depth falsely large by statistical anomalies, the maximum depth was defined as the depth reached by 90% of the escaped electrons. The depths are given in Figure 4.11 for PVA and TEMPO-CNF. They showed that the depth increases with acceleration voltage and was similar for the two materials.

Surface radius data was given as normalized counts per nm^2. In order to apply the same methodology as above with a 90% cut-off, the data was replotted as normalized counts per radius. The radius of the electrons that accounted for 90%

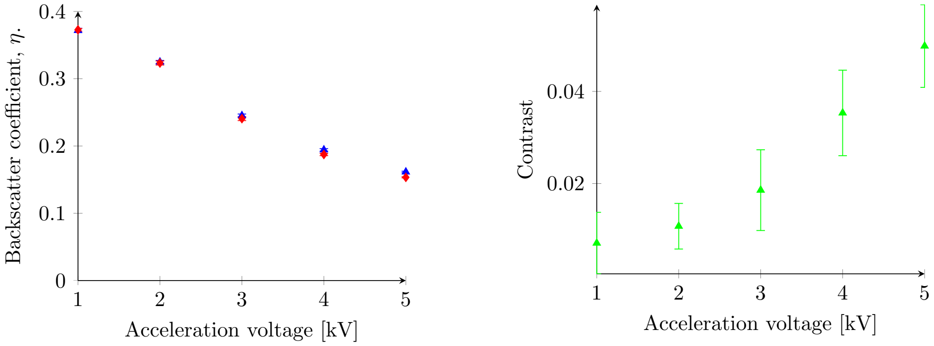

Figure 4.10: Simulated backscatter coefficients for TEMPO-oxidized nanocellulose (▲) and PVA(◆) with a 5 nm layer of Pt/Pd (80/20) on top. Backscatter contrast (▲) between TEMPO-oxidized nanocellulose and PVA by simulation. Casino was used to simulate the interaction of an electron beam with PVA and TEMPO-CNF by Monte Carlo methods. The number of BSE that escape through the surface are counted and the coefficent is calculated by Equation 2.4 automatically. The contrast was calculated by Equation 2.9. The standard deviations were calculated from 5 independent simulations.

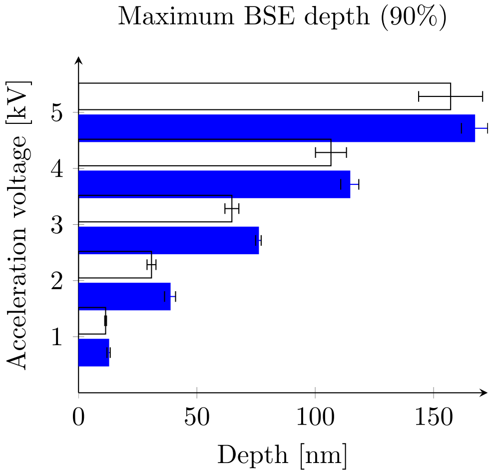

Figure 4.11: Simulated maximum depth of 90% of the BSE that escaped through the surface. The blue bars show the depth in PVA and the white bars show the depth in CNF. The depths were similar for both materials.The standard deviations were calculated from 5 independent simulations.

of the signal was taken as the surface radius. This was only done for PVA because it was assumed that most of the interaction volume would consist of PVA and the similarity in density and average atomic number would make the difference small. Table 4.2 shows the calculated interaction volumes when approximated as a cylinder and the surface radius of the escaped BSE at different acceleration voltages. The volume increased nearly an order of magnitude for each kV increased.

Table 4.2: The interaction volume of PVA at different acceleration voltages. Casio was used to simulate the surface radius and depth of backscattered electrons. A cut-off point was set when the normalized hit count reached 90% both for the radius and depth. The interaction volume was approximated as a cylinder.

Acceleration Voltage (kV)	*Surface radius(nm)*	*Standard deviation*	*Interaction volume (nm^2)*
1	20.5	0.45	0.10 x 10^5
2	67.5	0.40	3.17 x 10^5
3	133.9	1.45	24.28 x 10^5
4	222.7	1.43	91.81 x 10^5
5	331.6	5.26	291.49 x 10^5

Zero-charging point

From Equation 2.10, it was understood that zero charging would occur when the coefficients of secondary electrons (SE) and BSE were equal to one. Simulating SE required knowledge of the work function of the material. This is both difficult and time-consuming to measure accurately [81]. Therefore, Equation 2.7 was used to calculate the SE coefficients and Equation 2.5 was used to calculate BSE coefficents of PVA. Figure 4.12 shows the contribution of BSE and SE to the total emission. It is worth restating that these coefficients are defined as the number of emitted electrons per incident beam electron. Therefore, a coefficient should be regarded as an emission coefficient. The total emission was equal to one at approximately 1.5 kV.

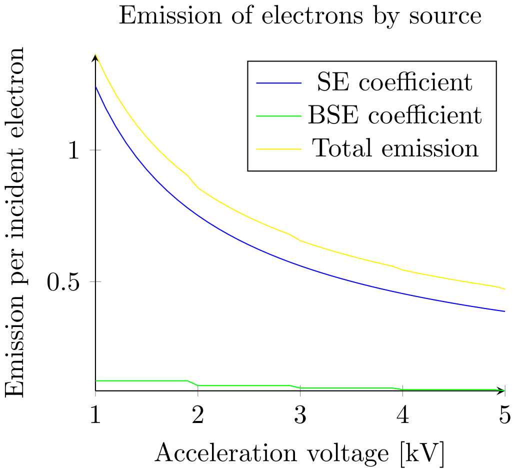

Figure 4.12: SE, BSE and total emission from PVA at different acceleration voltages. The data points were calculated from semi-empirical equations (Equation 2.7 for SE and Equation 2.5 for BSE). The point of interest was if, and where, the total emission equals one. This acceleration voltage would in theory result in zero charging of the imaged sample. The total emission was equal to one at approximately 1.5 kV.

4.2.2 Practical Approach to determine zero-charging point

An important aspect of LVSEM is the balance between signal-to-noise ratio, beam-induced damage and charging. All three subjects were described in Chapter 2.4.4. If the sample receives a too large electron dose, either by too high beam current or slow scan rate, beam damage and charging may occur. However, decreasing the beam current too low or scanning too fast will result in low signal-to-noise ratio and images that will provide little information. A method for increasing signal-to-noise ratio despite low beam current and fast scan rate is frame integration. Integration limits the noise by averaging the pixel value[1] for each pixel across a predetermined number of images, also called frames. The noise decreases with the square root of the number of frames integrated, but after a certain number of frames further reduction becomes insignificant. Due to image drift, either mechanical or electrostatic, there is a limit to the number of frames that can be integrated. For example, if a pixel in frame 1 drifts to the neighboring pixels location in frame 26, it will from frame 26 and beyond be averaged with this pixel instead. This will make the final integrated image blurry and therefore limits integration to 25 frames. Therefore, the optimal number of frames to integrated was explored. Figure 4.13 shows an uncoated PVA film with 4 wt% CNF captured with intergration of 64, 128 and 256 frames at the same scan rate, beam current and acceleration voltage.

The optimal acceleration voltage for LVSEM was also explored. The goal was to find the acceleration voltage, or voltage range, that would produce zero charging. Uncoated samples of 4CNF taken from 1.1 to 1.5 kV are shoen in Figure 4.14. An acceleration voltage of 1.4 kV resulted in the least distorted, and best, image.

---

[1] The value is a number between 0 and 255 which denotes the intensity or greyscale value. 0 is black and 255 is white.

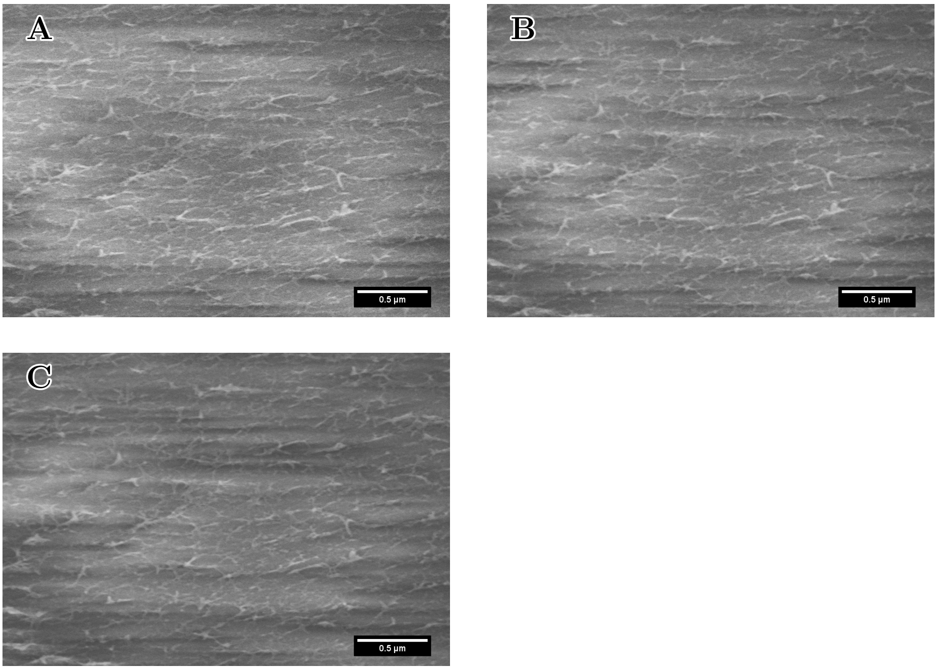

Figure 4.13: SEM micrographs of an uncoated surface of 4CNF showing the effect of the number of frames integrated: 64 (A), 128 (B) and 256 (C). The acceleration voltage was 1.3kV and the beam current was 2µA.

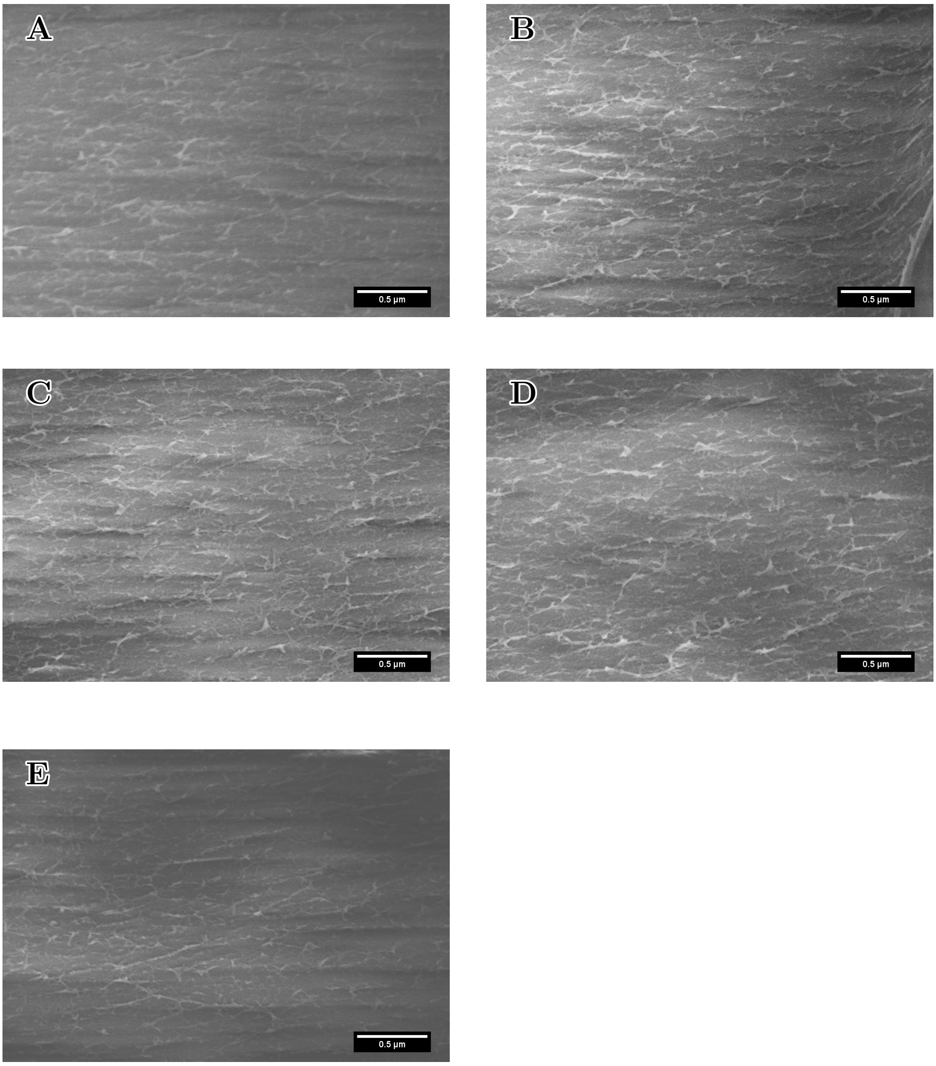

Figure 4.14: Uncoated surfaces of 4CNF captured with an acceleration voltage of 1.1 kV (A), 1.2 kV (B), 1.3 kV (C), 1.4 kV (D) and 1.5 kV (E) in SE mode. The beam current was set to 2µA and the images were taken using a fast scan rate and frame integration of 128 frames.

4.3 Characterization of PVA/Nanocellulose films by FIB-SEM

FIB-SEM has generally been used on biological samples and in the semiconductor industry. Therefore, few approaches and parameters exist in the literature for non-conductive polymers. Preliminary experiments were done to determine milling parameters. Then, slice and view experiments were done to characterize the 3-dimensional morphology.

The pattern used for all FIB-SEM experiments is shown in Figure 3.2B. The area called the cross-section is indicated. This was the area that would be investigated for nanocellulose. Figure 4.15 shows the benefit of increased signal from milling rectangles on each side of the cross-section. This pattern was milled at 30 kV with beam currents of 0.46, 0.92 and 2.8 nA. These exact currents were used as they predetermined options on the instrument. Using a beam current of 2.8 nA resulted in striations in the cross-section shown in Figure A.11. Lower currents like 0.92 and 0.46 nA largely produced patterns of equal quality to each other and free of striations. Following the pattern milling, the cross-section was cleaned twice.

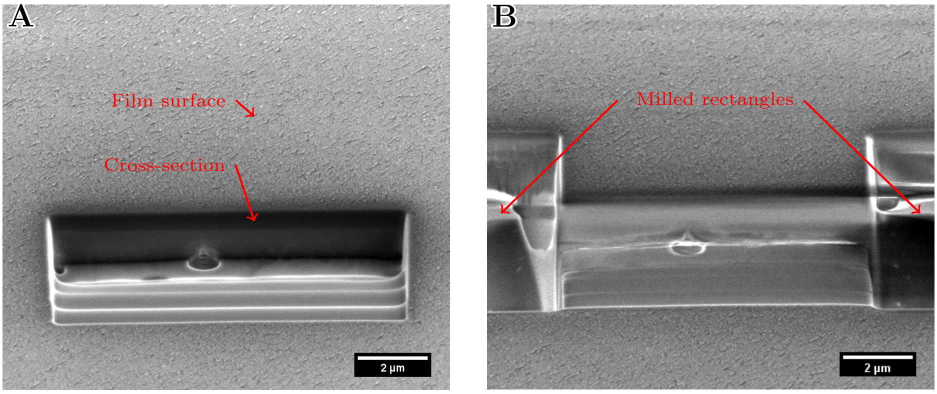

Figure 4.15: Pattern milling in FIB-SEM. The micrograps were taken at 3 kV with a beam current of 43 pA. A. Only a cross-section pattern was milled. The face of the cross-section was darker. B. Two rectangles were milled on each side resulting in the face appearing brighter.

4.3.1 FIB-SEM of Unstained Nanocellulose

The next step was investigating the cross-section for nanocellulose. Observations done in cross-sections were variable. Sometimes a featureless cross-section was seen with no discernible objects or contrast. Other times, features were seen. Figure 4.16 shows one such occurrence. The features seen had dark centers and bright perimeters. The shape and size of features observed varied a great deal. There appeared to be no correlation between milling and imaging parameters and observed features. However, no features were seen in PVAf samples. All objects were seen in films containing nanocellulose.

Using the parameters listed above and methods described in Chapter 3.2.1, several slice and view experiments were conducted. In preparation of slice and view, a layer of 50 nm of platinum was deposited on top of the polymer surface. As with previous cross-sections milled with FIB-SEM, faces were either smooth showing no features or contrast, or they revealed objects that persisted through one or many images. Figure 4.17 shows a series of consecutive images taken with 40 nm thick slices milled away by the ion beam between each image.

Based on 25 images captured in the same series as the six images in Figure 4.17, a 3D model was constructed from the 2D micrographs with Avizo. The reconstruction can be seen in Figure 4.18.

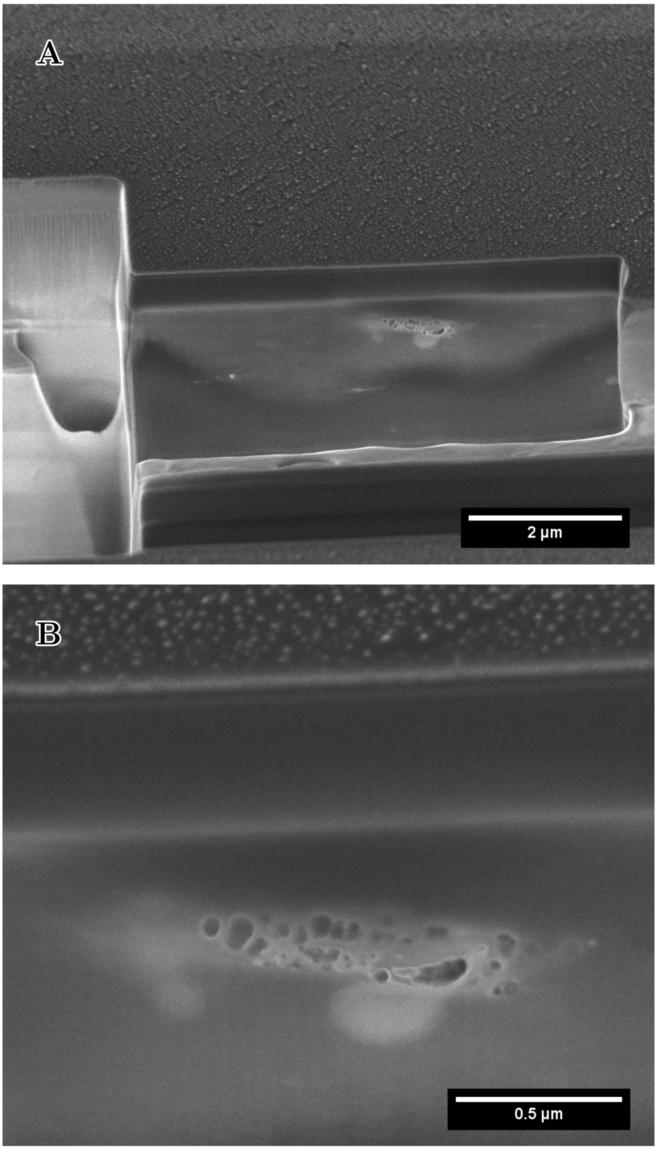

Figure 4.16: An feature identified in a FIB-SEM cross-section. The images were taken in SE mode with an acceleration voltage of 2kV. A. A cross-section was milled in a 4CNF film from the bottom surface. A thin section of the cross-section was milled away with an ion beam at 30kV and 48pA. B. High-magnifcation image of the object seen in the cross-section in A.

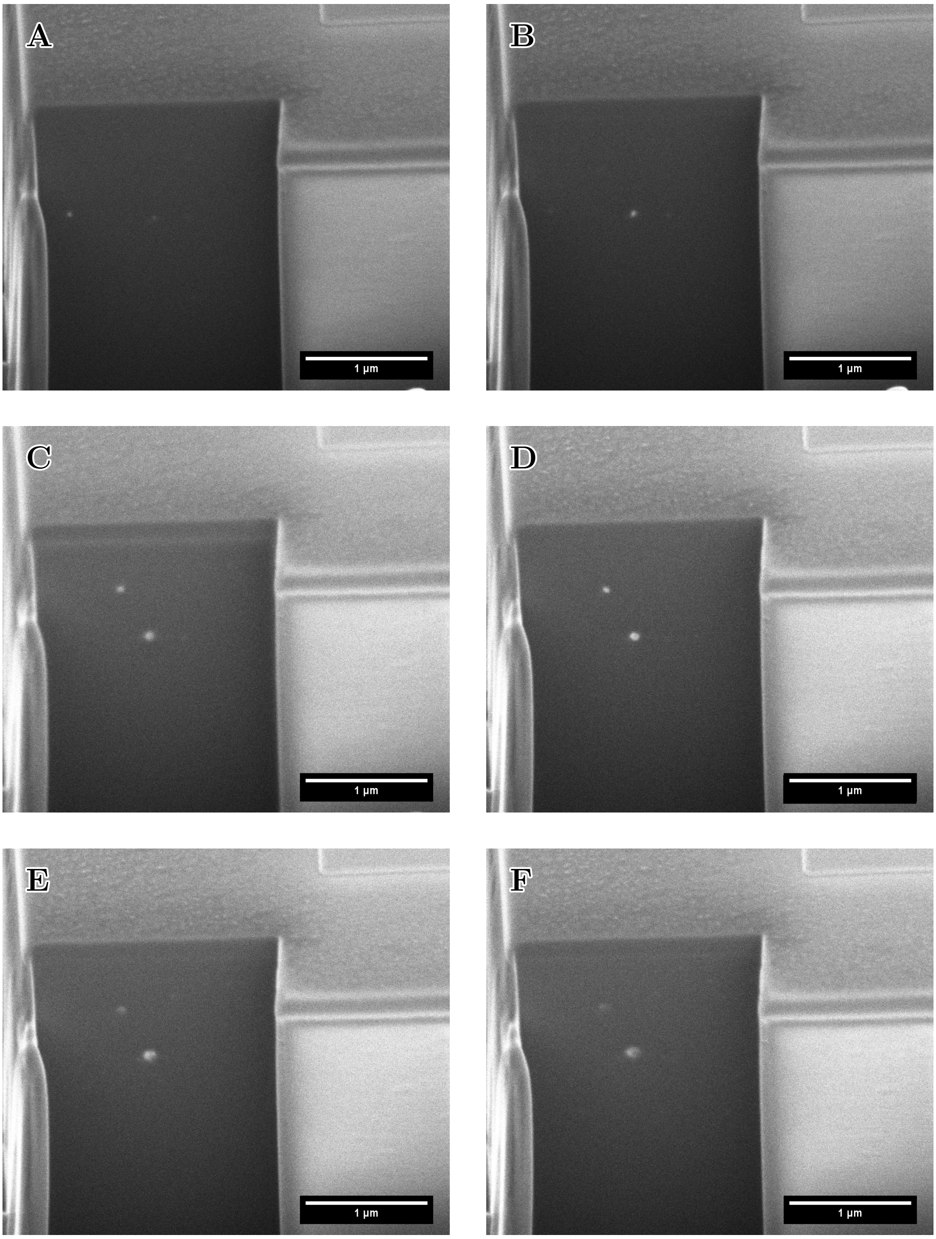

Figure 4.17: Slice and view of 4CNF with FIB-SEM. Sequential slice and view SEM micrographs were taken with an acceleration voltage of 1.4 kV and a beam current of 86 pA in SE mode. The images were captured with 1 µs scan time and 4 frames integrated. A slices was removed between each image with an ion beam using an acceleration voltage of 30 kV and beam current of 48 pA. Objects were visible in the cross-section that persisted through several images.

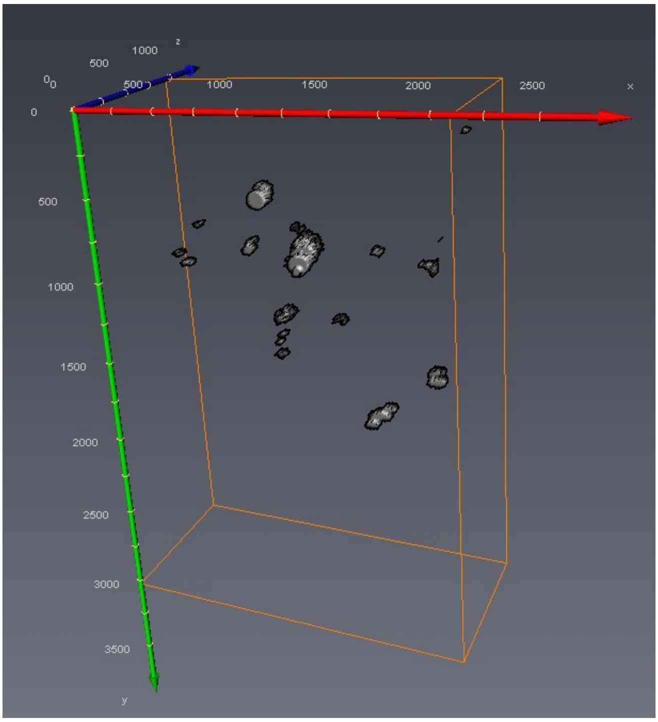

Figure 4.18: 3-D model of sequential SEM micropgraphs of a PVA film containing 4 wt% CNF. The units in the figure are in nm.

4.3.2 FIB-SEM of Stained Nanocellulose

The lack of consistent observations of features in FIB-SEM cross-sections required steps to be taken. Nanocellulose was most likely seen in conventional cross-sections with a good distribution making poor contrast a likely source of no nanocellulose in FIB-SEM cross-sections. During freeze fracture, the difference in material properties between PVA and nanocellulose will cause topography effects that are observed in SE mode. FIB milling does not cause any such topography effects and therefore require the use of BSE mode. Staining is a common method to overcome poor contrast and increase the BSE signal from one material relative to another. First, a novel staining technique was attempted. Ion-exchange has been extensively studied, also for cellulose, but not for the purpose of staining. TEMPO-oxidation of nanocellulose results in anionic carboxylic acid groups in the surface. The counter-ion to these groups is usually Na^+ or H^+. Cesium was attempted ion-exchanged for sodium. Cellulose stained by protocol 1 (Chapter 3.1.4) was made into a film with 50 wt% stained cellulose and 50 wt% CNF. The surface was then imaged with LVSEM to see if any contrast was visible. Unfibrillated cellulose was stained so there would be a visual difference between the stained cellulose and unstained CNF. Figure 4.19 shows a SE and BSE image of the same area on such a film. The larger fibers seen were most likely the Cs-stained fibers. The appeared clearly in SE mode and were just barely discernible in BSE mode.

Another attempt was made to ion-exchange Na with Cs, protocol 2. This time, 4 wt% unfibrillated cellulose was added to a PVA film. The cross-section was examined by FE-SEM. The very rough nature of the cross-section made BSE mode very challenging. A flat surface is desired to eliminate topography from contributing to contrast. Also, charging was a severe problem.

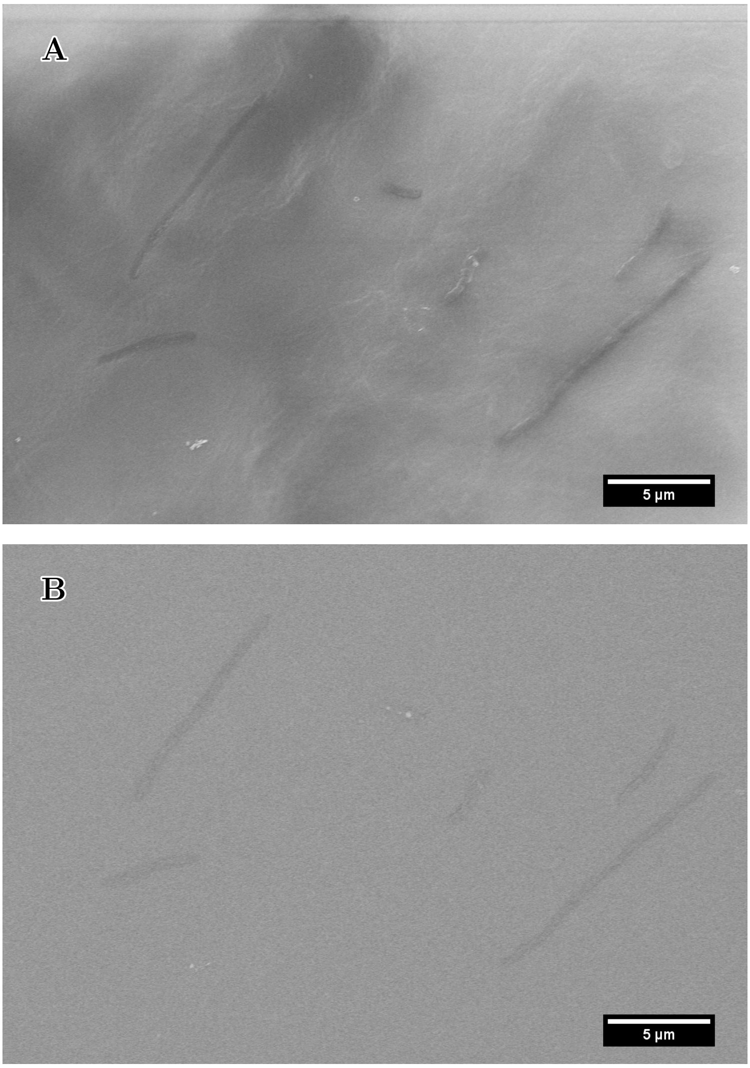

Figure 4.19: [Cs-stained films]Cs was ion-exchanged in TEMPO-oxidized cellulose that was not homogenized. A film was made by 50 wt% of the Cs-stained cellulose and 50 wt% CNF. A. The uncoated surface of the film imaged in SE mode a 1.6 kV acceleration voltage. B. The same area and acceleration voltage in A imaged in BSE mode.

Staining was also attempted with an established stain. The choice fell upon uranyl acetate (UA) which has been used on cellulose materials previously. Most protocols employ water as a solvent making the staining protocol less than ideal. Visual inspection of samples in 2% UA for 30 mins showed the distinct yellow color of uranyl acetate. Whether it had coated the surface or absorbed into the film was not possible to see. Figure 4.20 shows a cross-section of a 4CNC stained for 30 minutes in 2% UA. A difference was seen between the upper region of the cross-section which produced a strong signal and the lower region which produced a weaker signal. At the interface between the two regions, some features were seen as they appeared darker than the surrounding area.

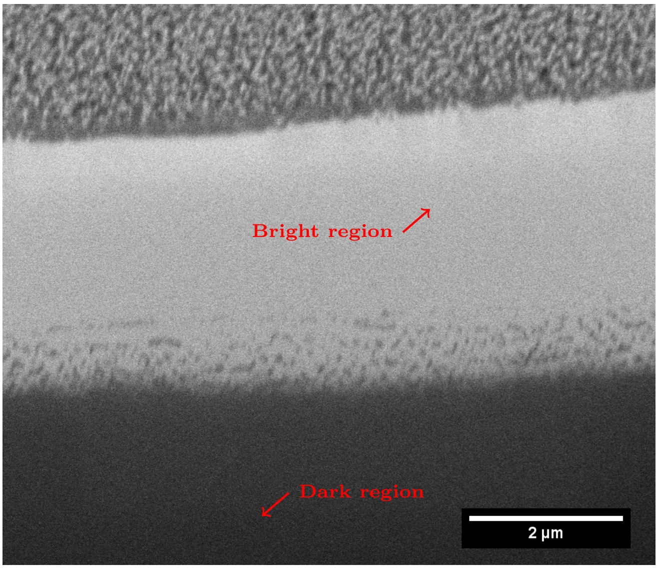

Figure 4.20: The top of a FIB-SEM cross-section of a UA stained sample. The image was taken in BSE mode with 2kV acceleration voltage and 0.69nA beam current. An increased BSE signal was detected from the upper 4 µm. At the boundary between the high and low signal areas, an area was seen where some parts produced low signal while other produced a high signal.

Staining was done for short durations as well. The 4CNF sample in Figure 4.21 was stained for 2 minutes and the cross-section yielded a more homogeneous signal. Some features were observed that appeared darker than the surrounding material with a bright appearance around the edges.

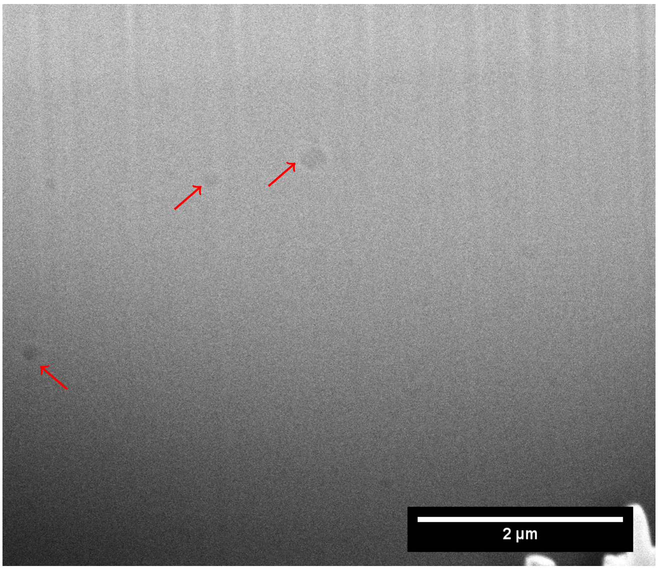

Figure 4.21: FIB-SEM cross-section of 4CNF stained with 1% uranyl acetate for 2 minutes. SEM image taken in BSE mode at 2 kV acceleration voltage. Some darker areas were observed in the cross-section. The vertical lines were striations caused by milling on a rough surface.

4.4 Characterization of PVA/nanocellulose films by Reactive Ion Etching

Reactive ion etching (RIE) was another novel characterization technique used on the PVA films. By etching a controlled depth from the surface, different layers in the film can be exposed. If a distinction can be made between nanocellulose and PVA, the distribution can be determined. First, the etch rates of PVA and CNC were determined. Then, the method was applied to different films.

4.4.1 Determining etch rates in different gas mixtures

Proper interpretation of etched films requires knowledge about the etch rates of nanocellulose and PVA. If PVA etches considerably faster than nanocellulose, the method may work well for characterizing a certain depth. Etching beyond this depth would yield less credible results as nanocellulose from earlier layers would still be visible when exposing layers below. It is therefore desired that etch rates be similar. The general procedure for measuring etch rates is to mask some portion of a sample, etch and use either a profilometer or cross-sectional SEM to measure the etch depth.

Etch rates were measured on pure PVA and CNC films. The first attempt at measuring etch rates consisted of covering roughly half the sample with polyamide tape and etching as described in Chapter 3.2.2 for 45 seconds. After etching, the tape was removed and the height between the two areas measured with a profilometer. Figure 4.22 shows the step height between the etched and unetched surface. Also shown in Figure 4.23 is the control sample which was not etched, but prepared and characterized in the same manner as the etched films. The etch step measured on the samples was roughly 150 nm. The control sample showed approximately the same step edge height. After evaluation of the results, cross-section examination was attempted by fracturing the films in LN. This was also unsuccessful.

A successful method was found by using polyamide tape, but not exposing the adhesive surface to the PVA and CNC film. The tape was fastened to the larger wafer the films were etched on, but not to the films themselves. The measured etch depths and durations are given in Table 4.3. Due to the large surface roughness, as seen to the left in Figure 4.23, several attempts were needed for a proper measurements to be made.

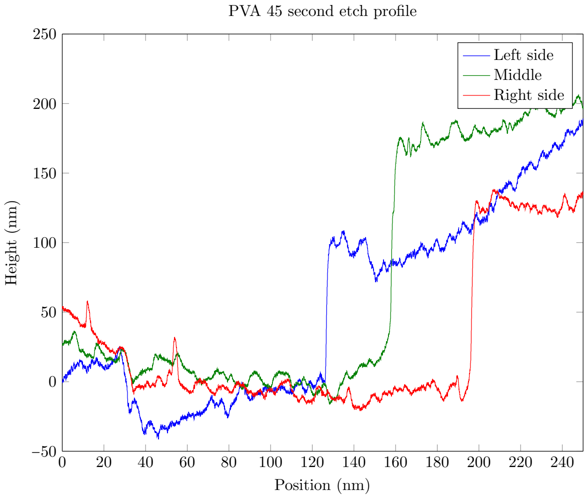

Figure 4.22: The height difference on a PVA surface after taping half with polyamide tape. The step height (the vertical steps seen at 120, 160 and 180 nm on the x-axis) of samples etched for 45 seconds. Three height profiles were measured with a profilometer, one on the left side, right side and in the middle. The data has been leveled to exclude drift.

Table 4.3: Measured etch rates for different durations and gas mixtures for PVA and CNC. The etch depths were measured with a profilometer.

	CNC		**PVA**	
Gas mix /Duration	45 sec	90 sec	45 sec	90 sec
Ar/SF$_6$	200 nm/min	190 nm/min	233 nm/min	
Ar	-	-	-	
Ar/SF$_6$/O$_2$	210 nm/min			

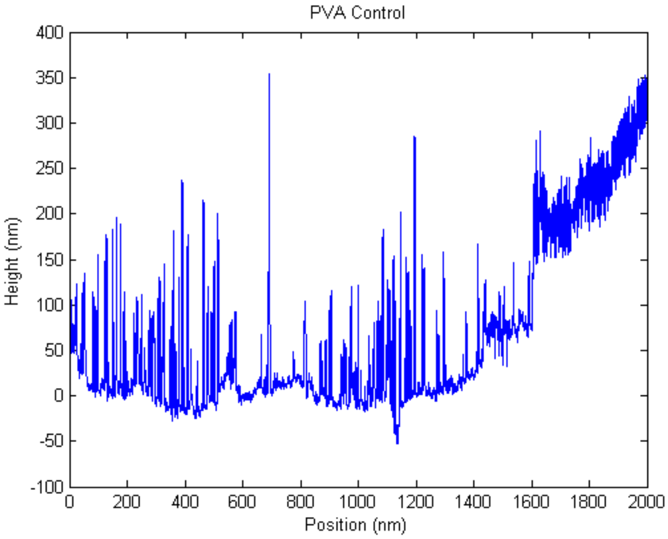

Figure 4.23: Control sample that was not etched. The polyamide tape was fastened to half the sample, left to rest and removed before measuring. A height difference (seen at 2600 nm on the x-axis) of approximately 150 nm is seen. Placeholder for tikz plot. The very rough surface of PVA films made in regular petri dishes was also seen.

4.4.2 Surface roughness

Film surface roughness was a problem when measuring etch rates and predicted to be a problem when investigating the distribution of nanocellulose by etching. Therefore, the origin of the surface roughness was investigated in order to reduce it. It was believed that the top surface exposed to air would be rough, but the surface towards the bottom of the petri dish would be fairly smooth. SEM micrographs of unetched 4CNF in Figure 4.24 show the bottom and top surface. There was a distinct difference in surface texture and smoothness with the bottom surface showing semi-ordered fibril-like features and the top surface being relatively smooth.

There were several possible explanations for the texture seen in Figure 4.24. Therefore, micrographs of the bottom surface of PVA films made according to Chapter 3.1.2 in a regular petri-dish and in a teflon petri-dish were taken. The micrographs are in Figure A.4 in the Appendix. Alternative casting substrates were explored to reduce the surface roughness of cast-evaporated films. A PVA was film cast on a silicon wafer in a petri dish as Si-wafers are very flat. The surface of Si-PVA cast-evaporated towards the silicon wafer surface is in Figure 4.25 and appeared very smooth compared to PVA films cast in regular petri dishes.

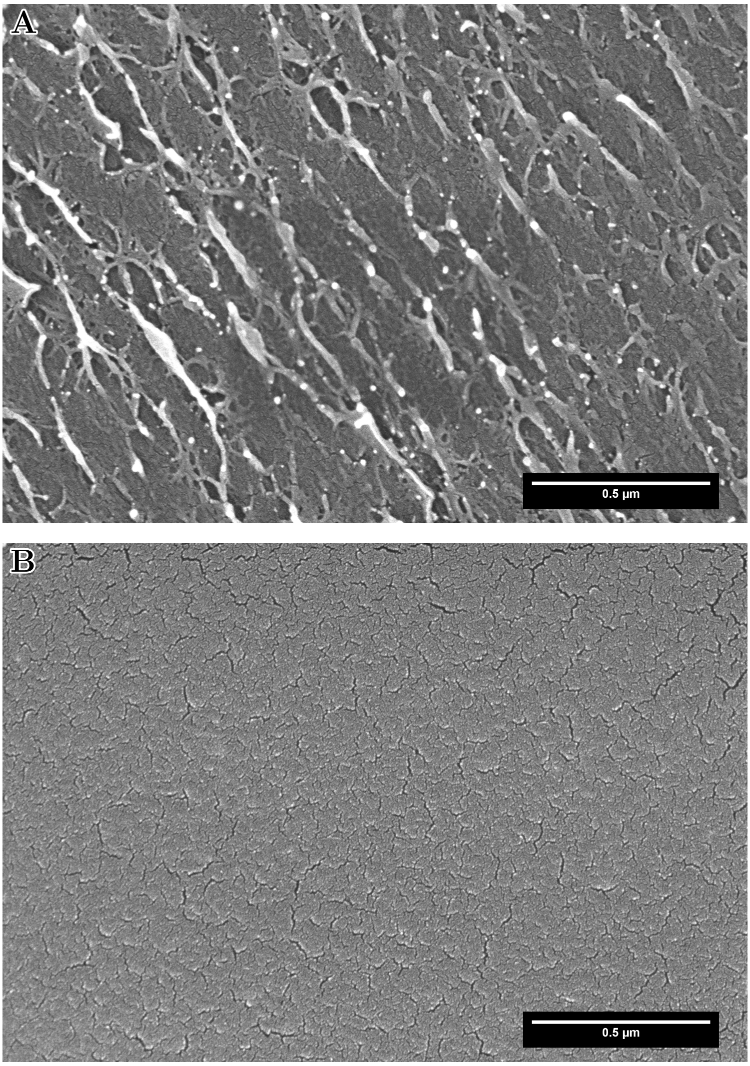

Figure 4.24: SEM micropgraphs of the surface against the petri-dish (A) and the surface against air (B) of a cast-evaporation 4CNF film. The films were coated with 5 nm of Pt/Pd. The surface roughness of A was clearly seen and appears to be slightly ordered. The surface of B appeared smooth.

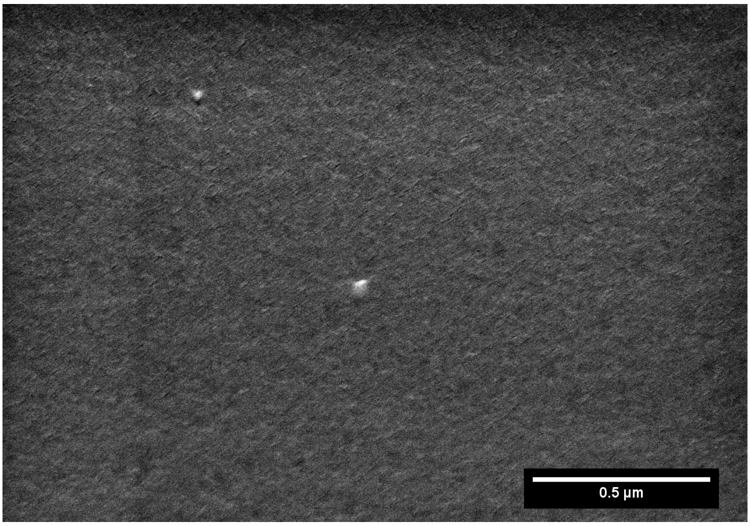

Figure 4.25: The surface of a PVA film cast-evaporated on a silicon wafer covered with silane. The surface was very smooth and particles and defects had to be located to be able to focus. Some surface texture was observed, but the sensitivity of PVA to electron radiation and the long duration required for focus made these very difficult to see.

4.4.3 Etched films

Based on the knowledge of etch rates and initial surface roughness, several films were etched for 1 minute, 30 seconds and 3 minutes. The long etch durations were chosen to possibly etch past the surface roughness that would disguise the nanocellulose and to investigate if the technique was applicable to characterizing the entire active layer in the membrane which is expected to be approximately 1 µm. Overview of which samples were etched and the durations are given in Table 3.2. A typical result of etching the bottom surface of the films is in Figure 4.26. This was the surface facing the bottom of the petri dish during drying. For the sake of readability, only an example is given here and the remaining micrographs are given in Appendix A.1.1.

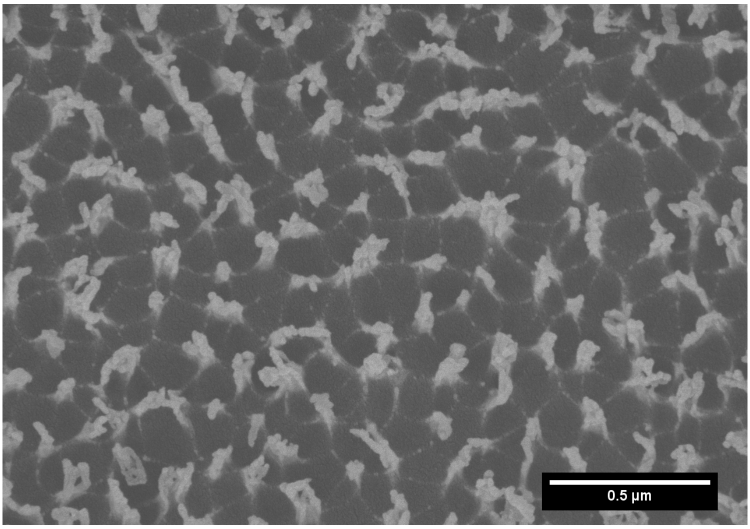

Figure 4.26: The bottom surface of 4CNF film etching for 1 minute and 30 seconds with SF_6 and Ar gas. The surface texture can resembled that of unetched samples like Figure 4.24A.

The micrographs showed very rough surfaces and revealed the need to etch films with less initial roughness on the surface. It was believed that these would yield less rough surfaces after etching. If not, the films would give insight as to how the method should be further improved. Therefore, Si-PVA and Teflon-PVA were etched for 1 minute and 30 seconds with SF_6 and Ar as previous results indicated that these films were smoother than PVA cast in regular petri dishes. The etched bottom surface of Si-PVA in Figure 4.27 did indeed show a less rough surface.

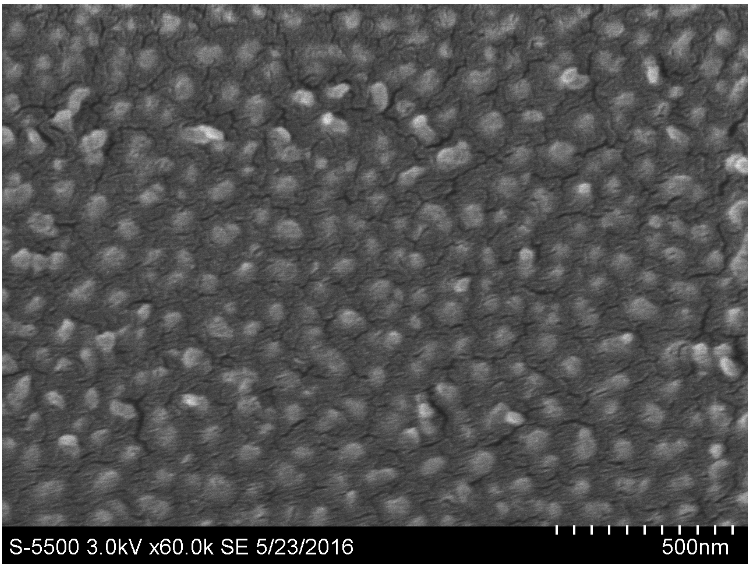

Figure 4.27: Bottom side of SiPVA sample etched for 1 minute and 30 seconds. The surface appeared smoother than the surface in Figure 4.26.

4.5 Freeze-drying with Liquid Nitrogen and Liquid Ethane

The importance and issues of characterizing porous films were covered in Chapter 2.3. Earlier work done in the project thesis discovered that drying methods like critical point drying and chemical drying were not usable on PVA/nanocellulose films. It was hypothesized that swelling caused by ethanol soaking resulted in severe mechanical stress followed by disintegration of the PVA/nanocellulose films. Freeze-drying preserved the film, but the initial thickness was reduced. It was believed this was the result of pore collapse. In order to reduce or eliminate the film collapse, freeze-drying in liquid ethane was established as a method. The method has been used previously, but not by the authors group/university.

Liquid nitrogen (LN) is commonly used to freezing samples. A high cooling rate is desirable to vitrify the sample, that is to prevent water crystals from nucleating and growing [50, 51]. A problem with LN is the Leidenfrost phenomenon.

Upon contact with the sample surface, nitrogen is at its boiling temperature and surrounds the sample with an insulating gas layer. This reduced the achievable cooling rate significantly ($0.5 \times 10^3 K/s$) [82]. Liquid ethane does not have this property as it is at its melting temperature and can effectively cool much faster. Depending on surface area to volume ratio, cooling rates above 10 000 K/s have been observed experimentally [50].

PVA films with 4% CNF were swelled in 95% relative humidity for 24 hours and freeze-dried in both liquid nitrogen and ethane. The samples were immediately transferred to a vacuum chamber for drying. A FIB-SEM cross-section of 4CNC freeze-dried using liquid ethane is in Figure 4.28. Fibril-like objects were seen in the cross-section.

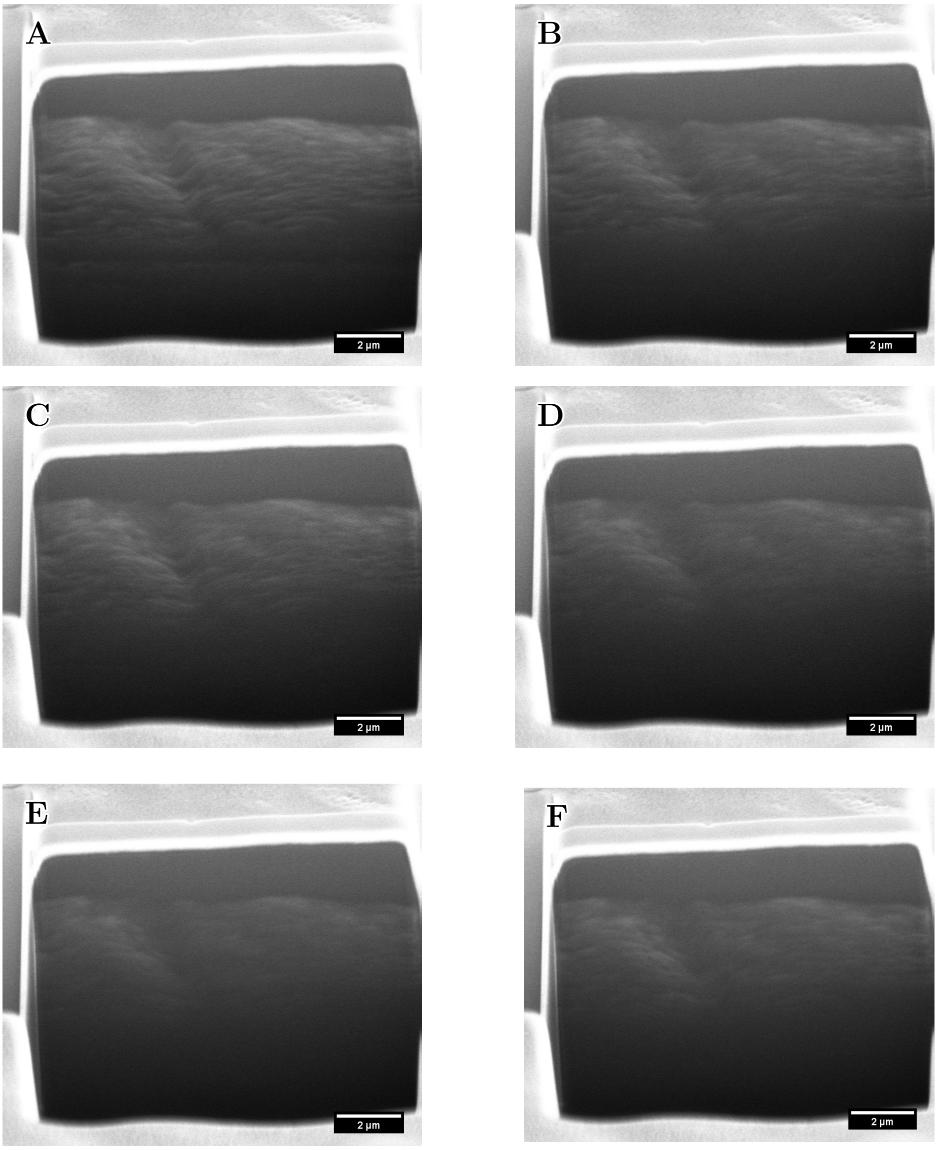

Figure 4.28: FIB-SEM cross-section of a 4% CNF film freeze-dried with liquid ethane. The images were taken between milling away 20 nm slices with the focused ion beam.

Chapter 5

Discussion

5.1 Cross-sectional Characterization

The conventional method of freeze-fracturing was done to both use the technique to characterize the films and to extend the technique to give quantitative information. Figure 4.1 showed that fracturing in liquid nitrogen produced usable cross-section. Some areas of the cross-section were smooth and flat which is desirable for image processing. This allows for software to automatically identify nanocellulose if it is visible in the cross-section. There appeared to be no trend in cross-section quality for weight percent or type of nanocellulose added. Cross-sections of many of the different films studied in this report is shown in Figure A.1 in the appendix. Areas closer to the bottom or top surface of the films frequently showed more unevenness and texture. This was most likely due to the fracturing process not instantaneously breaking the film into two, but compressing the surface on one side and stretching it on the other prior to fracture. This could present a problem when applying the technique to thinner films like the active layer in a membrane. Previous work done by the candidate showed a highly variable quality of cross-sections when the films were on a support membrane [1].

5.1.1 Nanocellulose in LN-fractured cross-sections

It seemed very likely that nanocellulose appeared as white dots in the cross-sections after examination of PVAf, 0.5CNC and 4CNC in Figure 4.2 and 4.3. This was concluded as PVAf showed no such dots while both 0.5CNC and 4CNC contained a large number of them. Also, a significant increase of white dots was seen from 0.5CNC to 4CNC which further confirms the hypothesis since the weight percent of cellulose nanocrystals (CNC) was 8 times larger for 4CNC than 0.5CNC. The white dots probably appeared because when fracturing a composite, the filler particles/fibrils will often not fracture. They will rather remain on one of the fracture faces protruding from the surface. This means that LN cross-sections often underestimate the amount of nanocellulose present as some particles will remain in the cross-section face not imaged. This will reduced the apparent number of nanocellulose. The findings were in agreement with work done by others on the same material system [21–23, 25]. Whether or not the dots were single or agglomerated CNC was difficult to determine. The dots were larger than expected from the reported size of CNC used in this study which was 5 nm in diameter (Chapter 3.1). This would favor the interpretation of partially agglomerated CNC.

Cellulose nanofibrils (CNF) also appeared as white dots similar to CNC in LN-fractured films. Additionally, there was a tendency of larger white particles/dots to appear (Figure 4.4). This could indicate more agglomeration of CNF than CNC in polyvinyl alcohol (PVA). The size of CNF was reported to be 15 nm in diameter and should therefore appear larger. However, the size of the white dots, with the exception of the aforementioned larger particles, did not appear larger. This would further substantiate the likelihood that white dots seen both in CNC and CNF films were agglomerates as a size difference should have been observed if they were single nanocellulose particles.

The composite image in Figure 4.5 made of several images taken across the height of a 4 wt% CNC film indicated an even distribution of nanocellulose laterally and vertically. The white dots appeared in equal concentration throughout the film. Close-up SEM micrographs taken of the cross-section near the near the edges in Figure 4.6, indicated that nanocellulose may be present in lower concentrations than elsewhere in the film. This was observed for both CNF and CNC. The strong interactions between water and nanocellulose could explain this. Drying during cast-evaporation was assumed to occur from top to bottom as the top was exposed to air. It was therefore conceivable that nanocellulose had a preference for the water phase relative to the solid phase and receded with the water as it evaporated. Also, micrographs taken at the bottom of films containing CNF showed protruding bulges which could be segregated and agglomerated CNF. An example is shown in Figure A.2 in the appendix. Such bulges were not seen in films containing CNC. It could also have been a fracture artifact, but the top of cross-sections showed no such bulges yet had many fracture artifacts as seen in Figure 4.1B. Earlier work has shown that segregation of CNC can occur, but the experiments were not done on this material system [83].

Most studies do not proceed further than qualitative analysis of the distribution of nanocellulose in cross-section. Therefore, an attempt was made to quantify the amount present by image processing. This was deemed possible as LN-fractured surfaces had some areas that were smooth and because nanocellulose was believed to be bright white dots with a high contrast to the surrounding PVA. The use of such a method would be especially interesting because a qualitative analysis seemed to indicate some agglomeration and/or segregation of nanocellulose. The results showed a modest increase in number of CNC from top and bottom of the film. CNF showed a significant increase from top to bottom. This corresponds well with the observed bulges at the bottom of CNF films. This could be mean the nanocellulose did infact recede with the water front as it evaporated. However, because LN-fracturing makes uneven and rough cross-sections near the surfaces of the film, the number of images suitable for image processing was low. In order to produce conclusive results, more images with usable cross-sections need be processed. Concentration profiles in Figure 4.7 and 4.8 did not show any large difference between the lateral distribution of nanocellulose near the top and bottom surface. The higher concentration at the surface could be explained by the software recognizing fracture artifacts as nanocellulose. The profiles did show that the method appeared to recognize more CNF than CNC.

The qualitative approach was adequately successful, but several steps in the process should be improved for conclusive results. First of all, a more reliable fracture method should be developed. LN-fracturing is currently the best method, but the fact that the quality of the cross-sections near the surfaces is unknown until SEM observation limits the use of image processing. Even in the images used for image processing in this report were not optimal. Unevenness caused areas with nanocellulose seen to the naked eye to not be recognized by the software due to insufficient contrast. Another issue was briefly touched upon earlier about some nanocellulose remaining on the ”other” cross-section after fracturing. Not being able to count these, will reduce the number of apparent nanocellulose.

The sensitivity of PVA to electron beam damage also posed a challenge. It limited the time available for adjusting focus and other parameters for the best possible image. Rough adjustments were done in an area adjacent to the imaged area, but fine adjustments were still required. Beam damage was a problem as it deforms and ”wrinkles” PVA. These artifacts were falsely recognized by the FIJI plugin as particles and as such increase the number of apparent nanocellulose. Figure A.3 in the Appendix shows an example of a pure PVA film and the artifacts that the software recognized as nanocellulose particles.

5.2 Low-Voltage SEM

5.2.1 Contrast in LVSEM

Contrast above 0.10 (10%) is generally deemed easy to see in SEM [52]. Simulations done in Figure 4.9 showed uncoated samples should give 0.16 contrast between nanocellulose and PVA at 2 kV. This meant that the two materials could be told apart with backscattered electrons (BSE). The simulated values were based on the interaction volume being entirely made up of one material. During actual imaging, nanocellulose was generally not expected to make up the entire interaction volume because of its small volume. Calculations done in Table 4.2 showed the interaction volume at 2 kV was approximately 3×10^5 nm^2. By calculating the approximate volume that would be occupied nanocellulose, and re-calculating the backscatter coefficient, η, a more realistic contrast can be calculated. This has been done in Appendix A.2.1. The contrast between this volume and the neighboring volume consisting of only PVA was then 0.081. The contrast was now in a range deemed difficult to see and will require special steps to resolve [52].

The constant value of backscatter coefficients in Figure 4.9 compared well with theory stating that backscatter coefficients are not dependent on acceleration voltage. However, when coating with a thin metal layer, the coefficients changed quite significantly. This can be explained by the interaction volume increasing as the acceleration voltage was increased. Pt/Pd have higher atomic numbers than PVA and nanocellulose, and therefore have higher coefficients. As the volume increased, the weight percent of PVA or nanocellulose increased and the coefficient decreased. Although metal coating allows for the use of higher acceleration voltages and beam currents, the BSE signal will not be any different for PVA compared with nanocellulose. The contrast between nanocellulose and PVA with a 5 nm Pt/Pd coating was very low, approximately 0.01 at 2kV. This demonstrated that metal coatings were not suitable when using BSE mode.

It should be noted that although TEMPO-CNF was used in simulations, the contribution of the acid groups with a sodium counter ion changed the average atomic number very little and approximately the same BSE coefficients can be used for cellulose in general including CNC.

5.2.2 Uncoated Imaging in LVSEM

Calculations to find a zero-charging point for PVA were done (Figure 4.12), and the point was found to be around an acceleration voltage of 1.5 kV. These calculations were confirmed by practical observations from Figure 4.14. There was a gradual reduction in image distortions from 1.1keV to around 1.3 and a nearly distortion-free image for 1.4keV. The distortions were most likely charging effects caused by a positively charged surface. At 1.5keV the distortions started to rise again. Results compare well with literature that states that the real zero-charging point actually lies below the theoretical value E2 point, inside the positive charging region [58]. It is worth noting that variations in local surface roughness determined the exact acceleration voltage which will give the best image. Figure 2.11 demonstrates that topography increases emission. This was exemplified by the return of dark areas in Figure 4.14E. The area imaged was changed between each acceleration voltage as surface damage and carbon deposition becomes troublesome after spending some time irradiating the same area with electrons.

The micrographs in Figure 4.14 were acquired with image integration of 128 images on fast scan rates with an image resolution of 1280x960 and a beam current of 2µA. Based on figure 4.13, the optimal number of integrated frames was determined to be 128. The noise was reduced from 64 to 128 frames, but the further decrease from 128 to 256 was not that substantial. The micrograph of 256 integrated frames was also more unclear than the previous micrographs of 64 and 128 integrated frames. Scan rate and beam current determine the beam dose the sample receives. It is desirable to keep this dose as low as possible as explained in Chapter 2.4.4. This beam current was close to the lower limit of the instrument. The lowest setting of 1 uA would be preferable with respect to charging and sample damage, but the signal to noise ratio was too poor to give good enough images. The fast scan rate was chosen because slower scan rates resulted in blurred images due to drift.

Figure 4.24A shows a metal-coated surface. Comparing it to the images in Figure 4.14, note the difference in scale bars, the surface texture appeared similar. The details in Figure 4.24A were more pronounced. The metal coating allowed a higher beam current, longer scan time and higher acceleration voltage. All of these parameters contributed to a clearer image. The magnification limit for uncoated samples, while still giving clear enough images to be examined, was found to be around 60 000x. This was highly dependent on surface roughness. Therefore, surface investigation using secondary electrons (SE) mode on such samples was better with a metal coating than without. However, as discussed earlier, a metal coating cannot be used for BSE mode or may be impractical, and uncoated samples are still preferred for this use.

5.3 Nanocellulose in FIB-SEM cross-sections

FIB-SEM characterization is challenging when the material in question is non-conductive and highly susceptible to beam damage both from the ion source and the electron source. The pattern used for cross-section investigation and slice and view is shown Figure 4.15. The images show the benefit of milling trenches, or rectangles, on each side of the cross-section. The cross-section face appeared much brighter after the rectangles were milled. Electrons escaping from the cross-section surface may be absorbed by the sidewalls perpendicular to the face. By removing these walls, the electrons can be collected by the detector. If the pattern milling was done with currents above 0.92nA, it caused surface roughness so sever that even the Pt layer cannot prevent striations in the cross-section. An example of striations is shown in Figure A.11 in the appendix. Once striations are formed, they were likely to persist in the cross-section despite milling away slices many times. Lower currents did in fact produce better cross-sections. Better cross-sections entail a smoother face and the top of the cross-section bordering the surface making a 90° angle. However, it took significantly more time. The technique must be usable on a large enough volume to be of value. Good cross-sections were equally obtainable by milling at 0.92nA and cleaning the cross-section with lower currents which took less time.

Metal layer deposition limited the surface damage and striations. Metal layers was added twice. First, a layer was added prior to FIB-SEM with a sputtercoater. The layer was 10 nm thick. This was done both to get a conductive surface and also to limit initial ion beam damage during pattern milling. This thickness was generally enough, but in some cases were lengthy imaging adjustments were required, the surface became very rough.

Imaging parameters were largely determined during LVSEM experiments and these were used for FIB-SEM as well. However, experience on the FIB-SEM, and during LVSEM on the STEM, showed that beam current, acceleration voltage and number of frames integrated had to be optimized for each session. It was mostly likely charging behavior and mechanical drift that varied between sessions and therefore limited using the same parameters for each sample. Determining the exact nature of the charging was

5.3.1 Unstained samples

Objects were seen in cross-sections on several occasions. The objects, as seen in Figure 4.16 and 4.17 could be several things including nanocellulose. Regardless of the origin of these objects, the observation alone demonstrates that the technique was usable on PVA films. One of the presumed problems was if nanocellulose could be resolved due to its size. LVSEM showed that there was a limit to the resolution due to drift, sample damage and charging. The observations made largely refute this assumption. It is still undetermined if nanocellulose in fact gives high enough contrast to PVA, but the resolution needed was obtained despite the non-conductive nature of PVA. Additionally, a 3D model was made of the images captured during the experiment shown in Figure 4.17. The automatic generation of such a model was contingent on high contrast between nanocellulose and PVA.

A possible explanation for not seeing nanocellulose in unstained FIB-SEM cross-sections is that there simply was too poor contrast between PVA and nanocellulose. The discussion of simulation results revealed that the contrast between PVA and nanocellulose was in a range deemed difficult to see. This would make viewing the cross-section at 1 kV much more desirable as the interaction volume is smaller than the volume of a CNF Reducing the interaction volume by reducing the acceleration voltage was attempted, but the same results as for uncoated LVSEM were seen. However, the reduced signal-to-noise ratio and drift at voltages below 1.5 in the FIB-SEM maked this difficult.

Features seen in 4.16 and 4.17 were approximately the same size and shape of CNF. Some objects in Figure 4.17 had cross-sections around 70-100 nm, which could indicate agglomerated CNF. Although micrographs were captured with SE, this mode can generate compositional contrast at low voltages. A natural question was if it was CNF, where was the remaining CNF expected to be seen in the cross-section. This probably meant that the features were not CNF. Other possible explanations were voids or contaminates from the cast-evaporation process. Voids were the mostly likely explanation as these may occur during casting or at the nanocellulose/PVA interface. The observation of voids was considered to be a good observation. If these were present around the PVA/nanocellulose interface, identifying the voids was an indirect observation of nanocellulose. It was hypothesized that such voids would be more apparent when more gentle drying methods such as freeze-drying were used. Contaminates as undissolved PVA or foreign particles could also be an explanation. Although normal care and practice was used, the films were made in a regular chemistry lab, and not clean room conditions.

5.3.2 Stained samples

The challenge of staining nanocellulose in PVA films can be seen as three-part. Firstly, the similar chemical nature makes it difficult to use a positive stain. Both are rich in hydroxyl groups and a positive stain often targets such groups. An oxidative stain like RuO_4 would therefore not work as it would stain both PVA and nanocellulose. Secondly, the densities are similar.This makes staining by absorption challenging. A stain will distribute itself equally in the two materials. Thirdly, PVA is highly soluble in water and alcoholic solvents. Many staining protocols use such solvents to stain a sample. Ion-exchange of Cs^+ was an ideal method to overcome all three problems. CNF would be stained separately and in solution prior to film casting. However, this was unsuccessful as shown in Figure 4.19. If stained with Cs, the larger fibers seen should be brighter than the background. The darker appearance was mostly likely a topography effect. BSE can give topography contrast like SE described in Chapter 2.11. The lack of compositional contrast may indicate that Na^+ was not successfully replaced by Cs^+. Calculations done in Appendix A.2.2 showed that ion-exchanging should have produced significant contrast. The contrast at 2 kV was around 0.37 which is well above the 0.10 limit mentioned earlier. Even exchanging only half of the Na ions would have given a contrast of 0.25. It was assumed that addition of NaOH increased the Na content to such a degree that Cs^+ could not bind to the acid groups. Therefore, a another protocol was tried without pH adjustment. pH adjustment was done to extend the fibers in solution. Successful ion exchange protocols have been done at low pH [73]. Although this work stated that electronegativity was a good indicator of ion exchange affinity, other work has stated Cs ions have higher affinity than Na ions [72]. As the second protocol did not yield any contrast in the cross-sections, the lower electronegativity of Cs^+ (0.79) compared to Na^+ (0.93) may be an explanation [84]. Another reason could be the extensive washing of the mass after ion exchange. Although this was done with deionized water, perhaps Cs^+ was exchanged with H^+. H^+ has both higher electronegativity, 2.2, and higher affinity.

Staining with uranyl acetate (UA) gave highly variable results. Some cross-sections investigated look like Figure 4.20. A layer approximately 4 µm thick from the surface had significantly higher contrast than the rest of the cross-section. At the interface between the bright and dark region, an area with dark features in the bright background was observed. Staining with UA could produce these images if UA was not absorbed all the way into the film. Figure 4.20 may therefore show the interface between the stained and unstained region. However, further investigation of UA stained samples is needed to determine this more conclusively. The shallow penetration depth of UA may be deceptive. The solubility of PVA in water and ethanol may make layers of PVA dissolve during staining. If this happened, the result would be a partially stained sample as seen in Figure 4.20 which was stained for 30 minutes. Acetone was considered as a possible solvent as PVA dissolves very poorly in it. However, it was disregarded for fear that UA would not diffuse into the PVA/nanocellulose films. This is because UA diffuses most likely with the help of the solvent, and when it does not penetrate into the film, the worry is that UA will not either. In the end an established protocol was chosen with a large degree of ethanol as a solvent.

The sample in Figure 4.21 was only stained for 2 minutes and was therefore exposed to water for only a short duration. No such interface between a bright and dark region was observed. The overall brightness of the cross-section was also lower. Occasionally, the same voids observed in earlier FIB-SEM cross-sections were observed. The stronger signal around the feature suggested these areas had been empty and the UA stain had accumulated in them. The darker center may indicate the presence of a slightly different substance then the exterior and that a void around the material limited the diffusion of UA into it. Both these observations further confirm the likelihood that these were voids around nanocellulose.

5.4 RIE as Characterization Technique

The recipe for ICP-RIE was based on educated guess-work, and must therefore be considered a starting point for optimization in every step. However, this was beyond the scope of the preliminary studies in this report to establish if the technique was applicable to this material system. Some experimentation was done with gas mixtures when determining etch rates in order to determine the role of each gas component.

Measuring Etch rates with different gas mixtures

Measuring etch rates was not straightforward. The polyamide tape used to protect areas of the films adhered quite strongly to the film. Figure 4.22 and 4.23 showed that although fairly plausible etch depths were obtained from the samples, the control sample also showed a large step height. The height was the same order of magnitude as the etch depths measured. This large error was probably caused by the tape pulling on the un-etch surface when it was removed. Additionally, the tape would be very difficult to remove from a CNC or CNF films without damaging them as they are very brittle and fracture readily. Cross-sectional examination was unsuccessful because freeze-fracturing of PVA films creates poor cross-section near the surface of the film as was discussed earlier. Therefore measuring a height difference in the sub micrometer range was not possible. CNC films were also too fragile to reliably fracture at the desired area.

The etch rates measured were similar which was good for the goal of layered characterization of the films. The etch rates were close to optimal as the goal was to etch PVA at the same rate as nanocellulose in order to expose it and observe it in SE mode. The accuracy of the measurement is not high, but adequate for this application. The step edge between the unetched and etch surfaces was identified in an optical microscope. These images are shown in Appendix A.13. However, some of the error sources should be mentioned. Firstly, not fastening the etch mask directly on the films opened up for the possibility of the film moving slightly and not creating a perfect step edge. The second source of error was film curling. Strain from cast-evaporation and heating during etching caused some films to curl. The reactive ion etching (RIE) used had a temperature controller set to 20°C, but poor contact between the film and the wafer may cause some heating. The profilometer functions best when the sample is flat, aside from the height variations to be measured. Lastly, the surface roughness was a source of error.

The higher etch rate observed for 45 sec compared to 90 sec in Table 4.3 was most likely due to O_2 being used in the recipe before. O_2 is known to etch organic material and some may have remained in the etching chamber even after pump and purge cycles. Good practice is usually to conduct a ”dummy” run with no samples using the recipe of choice. This ensures that the chamber is ”contaminated” with gases used in the desire recipe, not the gases leftover from the previous process. The results could also be statistical variation between runs. After this result, a dummy run was done before the start of each etch session if O_2 had been used prior to the session. The instrument mainly holds fluoride containing gases making the contamination of other gases less likely to affect the etch rate. A dummy run is time-consuming as the whole recipe takes roughly 20-30 minutes with vacuum pumping and purging of toxic gases being the time consuming steps. Therefore it was not implemented before all session. Only etching with Ar produced non-measurable etches. This is supported in the literature, refer to Chapter 2.7.1 for details, that either O or F is the etching gas. Optical images did not show any step edges.

5.4.1 Nanocellulose on etched surfaces and Surface roughness

The surface roughness and identification of nanocellulose on an etched surface are directly related topics. The goal of these experiments was to etch PVA slighty faster than nanocellulose in order to expose it and recognized it in SEM micrographs with SE. Roughness caused by initial conditions such as film casting substrate or etching conditions will obscure nanocellulose. Therefore, surface roughness induced by other sources than nanocellulose must be identified and eliminated.

Initial Roughness

SEM micrographs were taken of the bottom surface of PVA films cast in a regular and teflon petri dish in Figure A.4 and on a Si-wafer in Figure 4.25. These images showed that the most probable explanation for the surface structure was the surface of the petri dish itself. Earlier assumptions included that it might have been nanocellulose as it was first discovered on the bottom of PVA films containing nanocellulose. However, because the same structure was found on PVA films, it can not be nanocellulose. The texture also disappeared or changed when the petri dish was changed. All three films had rougher surfaces after being etched for 1 minute and 30 seconds. The least rough surface was observed for Si-PVA. This confirmed the hypothesis that the initial surface roughness was important for the final etched surface. The decrease in roughness was promising regarding the use of RIE as a characterization tool. A flat surface is important as the roughness resembles nanocellulose and for the method to be useful, nanocellulose must be seen clearly, consistently and not be confused with artifacts.

Etching-induced Roughness

The surface roughness appeared to increase when etching a film and when increasing etch duration from 1 minute and 30 seconds to 3 minutes for both 4CNC and 4CNF samples (Figure A.7, A.8, A.5 and A.6). This further indicates that the etching process increased the roughness, or in the least enhanced the initial roughness, and therefore requires further optimization. The grass-like structure seen on many of the etched samples are commonly observed when etching polymers [85]. There are several explanations for their appearance. Oxygen in the plasma is known to cause this and also increase roughness when etching polymers in general [31]. Although there was no oxygen in the gas mixture, it was present in PVA and nanocellulose. During etching, atomic oxygen may have formed and taken part in etching. If this was the case, there is little to be done about the surface roughness increasing. The grass-like structure has also been connected to a large rise in surface temperature. The wafer that supported the sample during etching was temperature controlled to 20℃, but poor thermal conduction in PVA and thermal contact between wafer and sample may have led to a hotter surface. If the temperature is too high, the polymer can carbonize and become a grass-like structure which is very hard to get rid of. As explained in Chapter 2.7.1, some surface reactions were exothermic and may have produced large amounts of heat. In addition, the surface was bombarded with energetic particles like Ar^+ and much of their energy is dissipated as heat. Lastly, the grass can be caused by etch resistant material forming in some areas. Fluorine addition describe in Chapter2.7.1 is an example of such a material, cross-linking of PVA could be another.

Nanocellulose-induced Roughness

Any difference observed between the etched surfaces of films cast in regular petri dishes would most likely stem from compositional differences. Both the height, size and spacing of roughness on the PVAf bottom surface was smaller than for 4CNF and 4CNC. The roughness on PVAf surface seemed to consist of isolated wire-like structures protruding from the surface (Figure A.9) while 4CNC etched under identical conditions was flatter with significantly larger structures on the surface (Figure A.7). This could possibly be from nanocellulose. The area in between the shapes had the characteristic cracking/wrinkling which PVA exhibits under electron radiation. 4CNF had yet another surface texture (Figure A.5), but the size-range appeared similar to that of 4CNC. The increased etch rate of PVA compared to nanocellulose may be manifesting itself as the increased roughness seen on films with nanocellulose. A clear distinction between CNF and CNC was difficult to make.

The difference between top and bottom surfaces was difficult to draw any conclusions on due to the large initial differences of the surfaces. However, the top surfaces of CNF and CNC were more similar in roughness than the bottom surfaces. This could indicate a higher similarity and therefore a lower content of nanocellulose. The large difference between the top surfaces of PVAf and both films containing nanocellulose indicates that there was most likely still a significant amount of nanocellulose near the top surface of the films. These observations further confirm those made from image analysis of cross-sections. There appeared to be more nanocellulose near the bottom surface than the top surface. It was expected that etch rates of CNF and CNC would differ somewhat as polymer characteristics like crystallinity are known to affect the etch rate [86].

5.5 Freeze-drying with Liquid Nitrogen and Liquid Ethane.

5.5.1 Experimental considerations

Freeze-drying in liquid ethane had two steps that required extra attention. First was the transformation of gaseous ethane to liquid. The amount of liquid nitrogen kept in the vessel around was critical to the formation of ethane. Too little and the gas would not be sufficiently cooled before escaping, and too much resulted in solid ethane. A small amount of solid ethane could quickly be turned into liquid ethane by force stirring with the gas delivery tube. However, if too much solid ethane was allowed to arise, it would remain solid until it disappeared by sublimation. The amount of solid ethane that appeared seemed to be related to the amount of liquid nitrogen in the vessel. Filling the vessel half-way with liquid nitrogen resulted in liquid ethane. The second step that required extra attention was keeping the temperature of the sample below -143°C (Chapter 2.3.1) until it was under vacuum.

5.5.2 Structural characterization of freeze-dried sample

PVA films with 4 wt% CNF were freeze-dried by two different freezing methods. Freezing with liquid ethane resulted in the fibril-like objects seen in Figure 4.28. The objects looked very similar to what CNF was expected to look like in a cross-section. This could indicate that the method successfully froze water amorphously. Therefore, small voids expected to be at the PVA/nanocellulose interface had been preserved. The same voids may have been seen in FIB-SEM cross-sections of unstained and stained samples. The lower concentration of these coincide well with the hypothesis that freeze-drying preserved more of the porous stucture. The reason the cavities appear bright was likely a charging effect as the electrons become trapped inside. They escape one surface, only to be reabsorbed by another. This process happens over and over, so the electron effectively remains in the void. Just as charging is electrons trapped in a non-conductive material. Although it may have been the voids that was observed, it could indicate where CNF was in the film.

However, based on earlier experience with FIB-SEM cross-sections, it was difficult to determine this conclusively. A possible explanation was milling artifacts, but milling artifacts should be in the lateral direction, not the horizontal as the beam milled from the top. A likelier explanation was the deposition of Pt protective layer prior to slice and view. Some Pt was deposited on the cross-section face.

Although the Pt was milled away, the electrons present in the conductive Pt could penetrate into the PVA behind it and remain there as charged areas. These areas will appear as bright compared to the uncharged regions. A similar effect was regularly seen when pausing other slice and view experiment to adjust focus. The adjustment was done by increasing magnification somewhere in the cross-section and adjusting focus and stigmatism. Then, the original magnification was restored and the slice and view experiment was resumed. The area zoomed in on appeared brighter than the surrounding area for a few slices before going back to the gray tone of the surrounding area. An example of this is shown in Figure A.12 in the Appendix.

Chapter 6

Conclusions

Several new methods have been used to characterize nanocellulose in PVA films. We have shown that the field emission (FE)-scanning electron microscope (SEM) characterization can be further developed to include a quantitative approach using image analysis to identify nanocellulose in selected areas. Image analysis discovered a segregation effect in films with CNC and with CNF. The method proved useful, but may be further refined for more accurate measurements. Concentration profiles were also made by the same method. These profiles revealed that the method generally recognized more CNF in a cross-section than CNC. They also showed that there was no significant difference in vertical distribution between the different films and between top and bottom surfaces. The lack of a better fracturing technique for PVA films limits the use of image analysis. Many samples must be fractured and imaged with SEM in order to find cross-sections flat and smooth, and therefore suitable.

Uncoated PVA films were successfully imaged with low-voltage scanning electron microscopy (LVSEM) as predicted Monte Carlo simulations and confirmed by experiments. A range around 1.4 kV acceleration voltage was found where charging of the polymer surface appeared to be close to zero. The exact values of acceleration voltage, beam current and image capture settings needed to be optimized for each sample, therefore no single value for each parameter can be defined as the best. The uncoated surface resembled that of the coated surfaces, and we therfore concluded that coating surfaces with 5 nm Pt/Pd was the best approach when SE mode was used. However, imaging uncoated surfaces has been proven to be possible for situations where coatings are not possible or unwanted.

Film cross-sections made by focused ion beam - scanning electron microscope

(FIB-SEM) was explored as a novel characterization technique. Milling and image resolution were proven to be good enough for characterizing nanocellulose. However, nanocellulose was not directly observed in the cross-sections by SE or BSE. The most probable explanations were that milling produced some local heating that may conceal nanocellulose or that contrast between PVA and nanocellulose was not sufficient. The latter was substantiated by Monte Carlo simulations. Several other cross-section features were seen and concluded to most likely to be voids in the film. The voids were hypothesized to occur at the nanocellulose/PVA interface. Staining was also attempted to increase contrast between nanocellulose and PVA. Ion-exchanging sodium counterions in TEMPO-oxidized CNF with Cs was unsuccessful in increasing contrast and was most likely due to Cs not successfully exchanging with sodium. Uranyl acetate (UA) staining was also tried and appeared to increase the BSE signal depending on UA concentration and staining duration. Similar features believed to be voids were observed in UA stained samples as well. A successful staining protocol would prove immensely helpful. When cross-section features were observed, 3D models were successfully made from sequential SEM images. The variable experimental results reveal that more experiments are necessary to fully determine the viability of FIB-SEM on this material system.

A method for preserving the native state of swollen films was developed. Samples freeze-dried in liquid ethane observed in FIB-SEM showed a significant increase in cross-section features believed to be interfacial voids. This may indicate a partial preservation of the porous structure.

RIE was challenging as a layered characterization technique. The etch rates found were close to optimal in that Ar/SF_6SF6 etched nanocellulose and PVA close to equally. Unfortunately, it roughened the surface of PVA films which would have concealed any nanocellulose, although casting PVA films on a flat surface (silicon wafer) reduced the roughness. Surface roughness was found to probably originate from a large increase in surface temperature of the sample during etching brought on by the poor heat conduction of PVA and surface reactions. It could also stem from etch resistant materials forming in only selected areas on the film surface.

Chapter 7

Further Work

As the aim of the work has been to develop new characterization techniques for nanocellulose in PVA films, all new methods used can be further improved. Making the PVA/nanocellulose films flatter, smoother and thinner could be an advantage in many applications. A thinner sample may cool faster and thereby give better results in freeze-fracturing and freeze-drying. Smoother films would benefit low-voltage SEM and reactive ion etching. The flatter films may produced less charging and thereby less electrostatic drift. This may allow a longer scan rates or strong beam currents that will give better images. Alternatively, the reduced electrostatic drift may open for using higher magnifications.

Further development of FIB-SEM characterization should be done as it would prove tremendously useful. Experiements should be done in order to learn whether contrast between PVA and nanocellulose is the main problem, or if ion beam heating of the polymer matrix is the problem. The latter problem can be addressed by specifically designed experiments. large cellulose fibers or other filler particles can be used to investigate the behavior of PVA at the matrix-filler interface. As of now, it is difficult to determine if there is melting/distortion of PVA in the cross-section because of the fine structure of PVA and the small size of nanocellulose. The first problem can be investigated with liquid nitrogen fractured cross-sections and FE-SEM in BSE mode. An analytical technique like energy dispersive X-rays (EDX) or mass spectroscopy shold be used to conclusively determine the presence of cesium. EDX was briefly attempted, but the rough cross-sections produced by liquid nitrogen fracturing was not suited for the technique. Uranyl acetate showed some indication that it would negatively stain the films. Further development of the protocol could possibly results in a working stain. Both concentration of the stain solution and staining duration should be further explored. It should be possible to measure the dissolution rate of PVA in water an By knowing this, a better staining protocol can be designed.

Liquid ethane freeze-drying appeared successful and should be further explored. Samples with different nanocellulose and varying weight percent should be examined. If there is a correlation between observed features and weight percent, it would further substantiate the hypothesis that the features are voids at the interface. Once this has been firmly established, the method can be used to characterize the distribution of nanocellulose.

Reactive ion etching could be further pursued by experimenting more with etching parameters like gas flow, gas mixture and power settings of the electrodes. Reduced power settings and gas flow may reduced the temperature on the surface and avoid "grass" formation. Also, the gas mixture should be explored to determine if Ar should be included or not. Physical etching rates are typically less material dependent, but sputtering yields have been shown to differ between different polymers. A recipe that does not induce surface roughness must be found before the method can be used for nanocellulose characterization.

References

[1] Henrik Riis. Structural characterization of poly (vinly alcohol) composite membranes for co2 gas separation. Master's thesis, Norges teknisk-naturvitenskapelig universitet, 2015.

[2] T.A. Boden, G. Marland, and Andres R.J. Global, regional and national fossil-fuel co2 emissions. *Carbon Dioxide Information Analysis Center, Oak Ridge National Laboratory, U.S. Department of Energy*, 2015.

[3] N. Stern. The Economics of Climate Change. Technical report, 2006.

[4] Bert Metz, Ogunlade Davidson, Heleen de Coninck, Manuela Loos, and Leo Meyer. Intergovernmental Panel on Climate Change. Special Report on Carbon Dioxide Capture and Storage. Technical report, 2005.

[5] Cheng-Hsiu Yu. A Review of CO2 Capture by Absorption and Adsorption. *Aerosol and Air Quality Research*, pages 745–769, 2012.

[6] Deanna M. D'Alessandro, Berend Smit, and Jeffrey R. Long. Carbon Dioxide Capture: Prospects for New Materials. *Angewandte Chemie International Edition*, 49(35):6058–6082, 2010.

[7] Dennis Y.C. Leung, Giorgio Caramanna, and M. Mercedes Maroto-Valer. An overview of current status of carbon dioxide capture and storage technologies. *Renewable and Sustainable Energy Reviews*, 39:426–443, 2014.

[8] Eric Favre. Carbon dioxide recovery from post-combustion processes: Can gas permeation membranes compete with absorption? *Journal of Membrane Science*, 294(1-2):50–59, 2007.

[9] P. Bernardo, E. Drioli, and G. Golemme. Membrane gas separation: A review/state of the art. *Industrial and Engineering Chemistry Research*, 48:4638–4663, 2009.

[10] A. Brunetti, F. Scura, G. Barbieri, and E. Drioli. Membrane technologies for CO2 separation. *Journal of Membrane Science*, 359(1-2):115–125, 2010.

[11] The cooperative reasearch centre for greenhouse gas technologies. `http://www.co2crc.com.au/images/imagelibrary/gen_diag/ccs_facilities_media.jpg`. Last accessed 13. December 2015.

[12] Lloyd M. Robeson. Correlation of separation factor versus permeability for polymeric membranes. *Journal of Membrane Science*, 62(2):165–185, 1991.

[13] Lloyd M. Robeson. The upper bound revisited. *Journal of Membrane Science*, 320(1-2):390–400, 2008.

[14] Taek Joong Kim, L. I. Baoan, and May Britt Hägg. Novel fixed-site-carrier polyvinylamine membrane for carbon dioxide capture. *Journal of Polymer Science, Part B: Polymer Physics*, 42(23):4326–4336, 2004.

[15] Jian Zou and W S Winston Ho. CO2-selective polymeric membranes containing amines in crosslinked poly (vinyl alcohol). *Journal of Membrane Science*, 286(1):310–321, 2006.

[16] Liyuan Deng, Taek-Joong Kim, and May-Britt Hägg. Facilitated transport of CO2 in novel PVAm/PVA blend membrane. *Journal of Membrane Science*, 340(1-2):154–163, 2009.

[17] Liyuan Deng and May-Britt Hägg. Carbon nanotube reinforced PVAm/PVA blend FSC nanocomposite membrane for CO2/CH4 separation. *International Journal of Greenhouse Gas Control*, 26:127–134, 2014.

[18] Muhammad Saeed and Liyuan Deng. CO2 facilitated transport membrane promoted by mimic enzyme. *Journal of Membrane Science*, 494:196–204, 2015.

[19] V Favier, H Chanzy, and J Y Cavaille. Polymer Nanocomposites Reinforced by Cellulose Whiskers. *Macromolecules*, 28:6365–6367, 1995.

[20] V Favier, H Chanzy, and J Y Cavaille. Nanocomposite materials from latex and cellulose whiskers. *Polymer for Advamced Technologies*, Volume 6:365–367, 1996.

[21] Shweta A Paralikar, John Simonsen, and John Lombardi. Poly (vinyl alcohol)/ cellulose nanocrystal barrier membranes. *Journal of Membrane Science*, 320(1):248–258, 2008.

[22] Mehdi Roohani, Youssef Habibi, Naceur M. Belgacem, Ghanbar Ebrahim, Ali Naghi Karimi, and Alain Dufresne. Cellulose whiskers reinforced

polyvinyl alcohol copolymers nanocomposites. *European Polymer Journal*, 44(8):2489–2498, 2008.

[23] Jue Lu, Tao Wang, and Lawrence T. Drzal. Preparation and properties of microfibrillated cellulose polyvinyl alcohol composite materials. *Composites Part A: Applied Science and Manufacturing*, 39(5):738–746, 2008.

[24] Y. M. Zhou, S. Y. Fu, L. M. Zheng, and H. Y. Zhan. Effect of nanocellulose isolation techniques on the formation of reinforced poly(vinyl alcohol) nanocomposite films. *Express Polymer Letters*, 6(10):794–804, 2012.

[25] Alain Dufresne. Cellulose Microfibrils from Potato Tuber Cells : Processing and Characterization of Starch – Cellulose Microfibril Composites. *Polymer*, 76(14):2080–2092, 2000.

[26] Zhi Wang, Meng Li, Yan Cai, Jixiao Wang, and Shichang Wang. Novel CO2 selectively permeating membranes containing PETEDA dendrimer. *Journal of Membrane Science*, 290(1-2):250–258, 2007.

[27] Qiuju Wu, Marielle Henriksson, Xiaohui Liu, and Lars A. Berglund. A high strength nanocomposite based on microcrystalline cellulose and polyurethane. *Biomacromolecules*, 8(12):3687–3692, 2007.

[28] M. Peresin, Y. Habibi, J. Zoppe, J. Pawlak, and O. Rojas. Nanofiber Composites of Polyvinyl Alcohol and Cellulose Nanocrystals: Manifacture and Characterization. *Biomacromolecules*, 11:674–681, 2010.

[29] Mi Jung Cho and Byung Dae Park. Tensile and thermal properties of nanocellulose-reinforced poly(vinyl alcohol) nanocomposites. *Journal of Industrial and Engineering Chemistry*, 17(1):36–40, 2011.

[30] Yottha Srithep, Lih Sheng Turng, Ronald Sabo, and Craig Clemons. Nanofibrillated cellulose (NFC) reinforced polyvinyl alcohol (PVOH) nanocomposites: Properties, solubility of carbon dioxide, and foaming. *Cellulose*, 19(4):1209–1223, 2012.

[31] Christopher Harrison, Miri Park, P.M. Chaikin, Richard a. Register, Douglas H. Adamson, and Nan Yao. Layer by layer imaging of diblock copolymer films with a scanning electron microscope. *Polymer*, 39(13):2733–2744, 1998.

[32] John R. Hollahan and Alexis T. Bell. *Techniques and Applications of Plasma Chemistry.* John Wiley and Sons, 1974.

[33] Alain Dufresne. Nanocellulose: A new ageless bionanomaterial. *Materials Today*, 16(6):220–227, 2013.

[34] Alain Dufresne. *Nanocellulose: From Nature to High Performance Tailored Materials.* Walter De Gruyter, 2012.

[35] Dieter Klemm, Friederike Kramer, Sebastian Moritz, Tom Lindström, Mikael Ankerfors, Derek Gray, and Annie Dorris. Nanocelluloses: A new family of nature-based materials. *Angewandte Chemie - International Edition*, 50(24):5438–5466, 2011.

[36] Robert J Moon, Ashlie Martini, John Nairn, John Simonsen, and Jeff Youngblood. Cellulose nanomaterials review: structure, properties and nanocomposites. *Chemical Society reviews*, 40(7):3941–3994, 2011.

[37] Vijay Kumar Thakur. *Nanocellulose Polymer Nanocomposites: Fundamentals and Applications.* 2014.

[38] Jonathan Torstensen. Nano mbe project description. 1993.

[39] Carl Moser. Energy efficiency for cellulose nanofiber production. *Cellulose Materials Doctoral Students Summer Conference*, 2015.

[40] Akira Isogai, Tsuguyuki Saito, and Hayaka Fukuzumi. TEMPO-oxidized cellulose nanofibers. *Nanoscale*, 3(1):71–85, 2011.

[41] TAPPI. Proposed New TAPPI Standard: Standard Terms and Their Definition for Cellulose Nanomaterial. pages 1–6, 2011.

[42] Linda Sawyer, David Grubb, and Gregory F Meyers. *Polymer microscopy.* Springer Science & Business Media, 2008.

[43] Vasant R Gowariker, NV Viswanathan, and Jayadev Sreedhar. *Polymer science.* New Age International, 1986.

[44] Shuhei Kudo, Emiko Otsuka, and Atsushi Suzuki. Swelling behavior of chemically crosslinked PVA gels in mixed solvents. *Journal of Polymer Science Part B: Polymer Physics*, 48(18):1978–1986, 2010.

[45] Ken Dill and Sarina Bromberg. *Molecular driving forces: statistical thermodynamics in biology, chemistry, physics, and nanoscience.* Garland Science, 2010.

[46] J. Grignon and a. M. Scallan. Effect of pH and neutral salts upon the swelling of cellulose gels. *Journal of Applied Polymer Science*, 25(12):2829–2843, 1980.

[47] Lisa Brannon-Peppast. Equilibrium swelling behavior of pH-sensitive hydrogels. *Chemical Engineering*, 46(3):715–722, 1991.

[48] Paul C. Hiemenz and Raj Rajagopalan. *Principles of Colloid and Surface Chemistry.* Taylor and Francis Group, 3 edition, 1997.

[49] C. Jeffrey Brinker and George W. Scherer. *Sol-gel Science: The Physics and Chemistry of Sol-Gel Processing.* Academic Press, 1990.

[50] S M Bailey and J a Zasadzinski. Validation of convection-limited cooling of samples for freeze-fracture electron microscopy. *Journal of microscopy*, 163(Pt 3):307–320, 1991.

[51] D Cheng, Drg Mitchell, D-b Shieh, and F Braet. Practical Considerations in the Successful Preparation of Specimens for Thin-Film Cryo-Transmission Electron Microscopy. *Current Microscopy Contributions to Advances in Science and Technology*, pages 880–890, 2012.

[52] Joseph I. Goldstein, Dale E. Newbury, Patrick Echlin, David C. Joy, Charles E. Lyman, Eric Lifshin, Linda Sawyer, and Joseph R. Michael. *Scanning Electron Microscopy and X-ray Microanalysis.* Springer US, 2003.

[53] Ray F. Egerton. *Physical Principles of Electron Microscopy-an Introduction to TEM, SEM, and AEM.* Springer Science & Business Media, 1 edition, 2005.

[54] K Kanaya and S Okayama. Penetration and energy-loss theory of electrons in solid targets. *Journal of Physics D: Applied Physics*, 5(1):43–58, 2002.

[55] D C Joy. An Introduction to Monte Carlo Simulation.pdf, 1991.

[56] Andrew R Leach. *Molecular modelling: principles and applications.* Pearson education, 2001.

[57] J. H. Butler, D. C. Joy, G. F. Bradley, and S. J. Krause. Low-voltage scanning electron microscopy of polymers. *Polymer*, 36(9):1781–1790, 1995.

[58] Jacques Cazaux. About the mechanisms of charging in EPMA, SEM, and ESEM with their time evolution. *Microscopy and microanalysis : the official journal of Microscopy Society of America, Microbeam Analysis Society, Microscopical Society of Canada*, 10(6):670–684, 2004.

[59] DC Joy and CS Joy. Low voltage scanning electron microscopy. *Micron*, 27(3-4):247–263, 1996.

[60] Heide Schatten and James B Pawley. *Biological low-voltage scanning electron microscopy.*

[61] Nan Yao. *Focused Ion Beam Systems : Basics and Applications.* Cambridge University Press, 2007.

[62] Nan Yao, editor. *Focused Ion Beam Systems.* Cambridge University Press, 2007. Cambridge Books Online.

[63] Michael J Dykstra and Laura E Reuss. *Biological electron microscopy: theory, techniques, and troubleshooting.* Springer Science & Business Media, 2011.

[64] Eero Sjostrom. The origin of charge on cellulosic fibers. *Nordic Pulp and Paper Research Journal*, 04(02):090–093, 1989.

[65] Michael Quirk and Julian Serda. *Semiconductor manufacturing technology*, volume 1. Prentice Hall Upper Saddle River, NJ, 2001.

[66] M Mao, Yn Wang, and A Bogaerts. Numerical study of the plasma chemistry in inductively coupled SF 6 and SF 6 /Ar plasmas used for deep silicon etching applications. *Journal of Physics D: Applied Physics*, 44(43):435202, 2011.

[67] Jörg Friedrich. *The plasma chemistry of polymer surfaces: advanced techniques for surface design.* John Wiley & Sons, 2012.

[68] S. R. Cain, F.D. Egitto, and F. Emmi. Relation of polymer structure to plasma etching behavior: Role of atomic fluorine. *Journal of Vacuum Science & Technology A: Vacuum, Surfaces, and Films*, 5(4):1578–1584, 1987.

[69] University of maine. `http://umaine.edu/pdc/cellulose-nano-crystals/`. Last accessed March 30, 2016.

[70] Karen Reinhardt and Werner Kern. *Handbook of silicon wafer cleaning technology.* William Andrew, 2008.

[71] Clare M. Lewandowski. Hydrophobicity, Hydrophilicity and Silane Surface Modification. *Gelest, Inc.*, 1, 2015.

[72] Håvard Fjerdingen. *Studies of the Fundamental Aspects of Kraft Paper Recycling.* PhD thesis, Norges tekniske-naturvitenskapelig universitet, 1997.

[73] T. Saito and A. Isogai. Ion-exchange behavior of carboxylate groups in fibrous cellulose oxidized by the TEMPO-mediated system. *Carbohydrate Polymers*, 61(2):183–190, 2005.

[74] Pierre Hovington, Dominique Drouin, and Raynald Gauvin. CASINO: A new Monte Carlo code in C language for electron beam interaction - Part I: Description of the program. *Scanning*, 19:1–14, 1997.

[75] Pierre Hovington, Dominique Drouin, Raynald Gauvin, David C. Joy, and Neal Evens. CASINO : A New Monte Carlo Code in C Language for Electron

Beam Interac- tions - Part II : Tabulated Values of the Mott Cross Section. *Scanning*, 19:20–28, 1997.

[76] Pierre Hovington, Dominique Drouin, Raynald Gauvin, David C Joy, and Neal Evans. CASINO: A new monte Carlo code in C language for electron beam interactions-part III: Stopping power at low energies. *Scanning*, 19(1):29–35, 1997.

[77] Dominique Drouin, A. R. Couture, Dany Joly, Xavier Tastet, Vincent Aimez, and Raynald Gauvin. CASINO V2.42 - A fast and easy-to-use modeling tool for scanning electron microscopy and microanalysis users. *Scanning*, 29(3):92–101, 2007.

[78] David C. Joy. The theory and practice of high-resolution scanning electron microscopy. *Ultramicroscopy*, 37(1-4):216–233, 1991.

[79] Caroline A Schneider, Wayne S Rasband, and Kevin W Eliceiri. NIH Image to ImageJ: 25 years of image analysis. *Nature Methods*, 9(7):671–675, 2012.

[80] Johannes Schindelin, Ignacio Arganda-Carreras, Erwin Frise, Verena Kaynig, Mark Longair, Tobias Pietzsch, Stephan Preibisch, Curtis Rueden, Stephan Saalfeld, Benjamin Schmid, et al. Fiji: an open-source platform for biological-image analysis. *Nature methods*, 9(7):676–682, 2012.

[81] C. F. Gallo, W. L. Lama, and W. L. Lama. Classical Electrostatic Description of the Work Function and Ionization Energy of Insulators. *IEEE Transactions on Industry Applications*, IA-12(1):7–11, 1976.

[82] Patrick Echlin. *Low-temperature microscopy and analysis.* Springer Science & Business Media, 2013.

[83] Alain Dufresne, Jean-Yves Cavaillé, and William Helbert. Thermoplastic nanocomposites filled with wheat straw cellulose whiskers. Part II: Effect of processing and modeling. *Polymer Composites*, 18(2):198–210, 1997.

[84] G. Aylward and T. Findlay. *Si chemical data.* Wiley, 6 edition, 7 2006.

[85] A Crockett, M Almoustafa, and W Vanderlinde. Plasma Delayering of Integrated Circuits. Technical report, 2004.

[86] G. Michler. *Electron Microscopy of Polymers.* Springer, 2008.

Appendix A

A.1 SEM micrographs

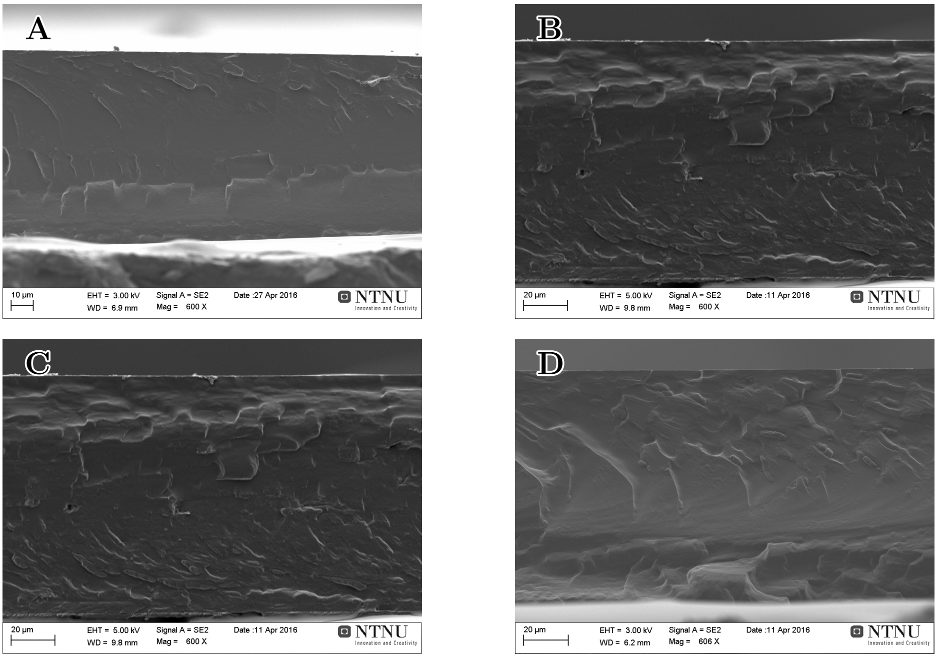

Figure A.1: Cross-section of 0.5CNF (A), 4CNF (B), 0.5CNC(C) and PVAf (D) made by liquid nitrogen fracturing. There was no general trend between cross-section appearance and weight percent or nanocellulose type.

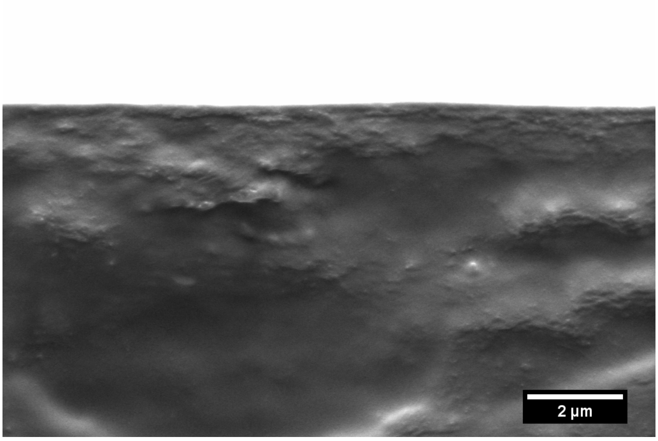

Figure A.2: Cross-section of 4CNF prepared by LN fracturing. The image was taken at the bottom surface. Images taken at this point often showed bulges indicated by arrows. These were not seen at the top surface or in films containing CNC.

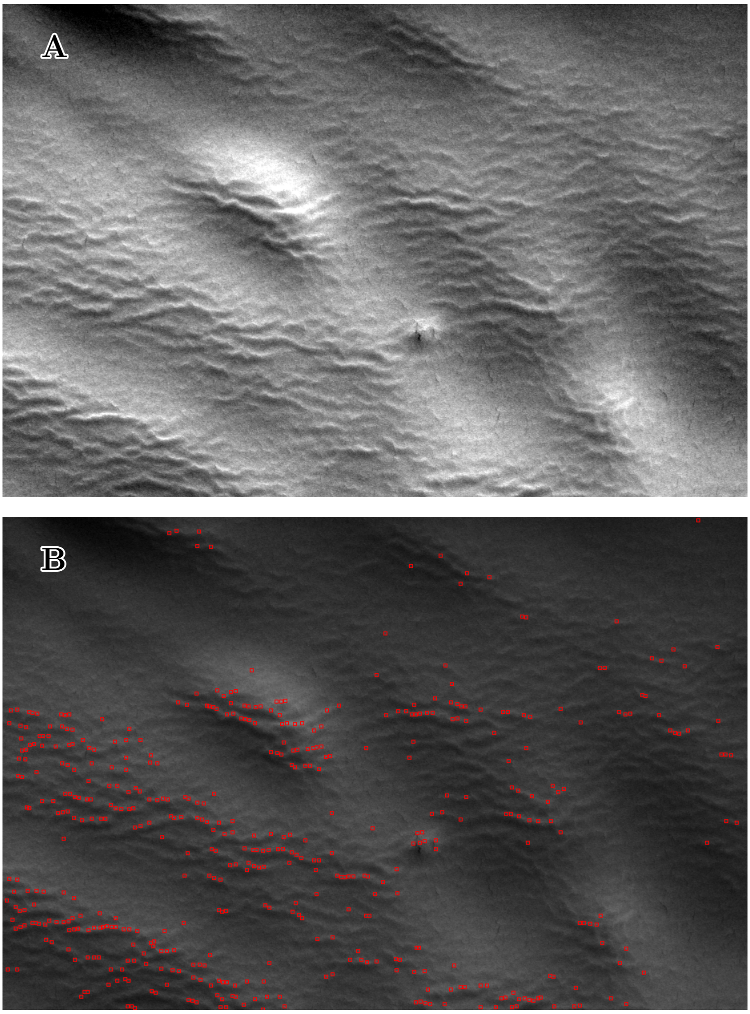

Figure A.3: A. The cross-section of a neat PVA film after extensive imaging. Wrinkles appeared and the polymer deformed. B. The same image with red circles showing areas the Mosaic particle tracker plugin recognized as nanocellulose particles.

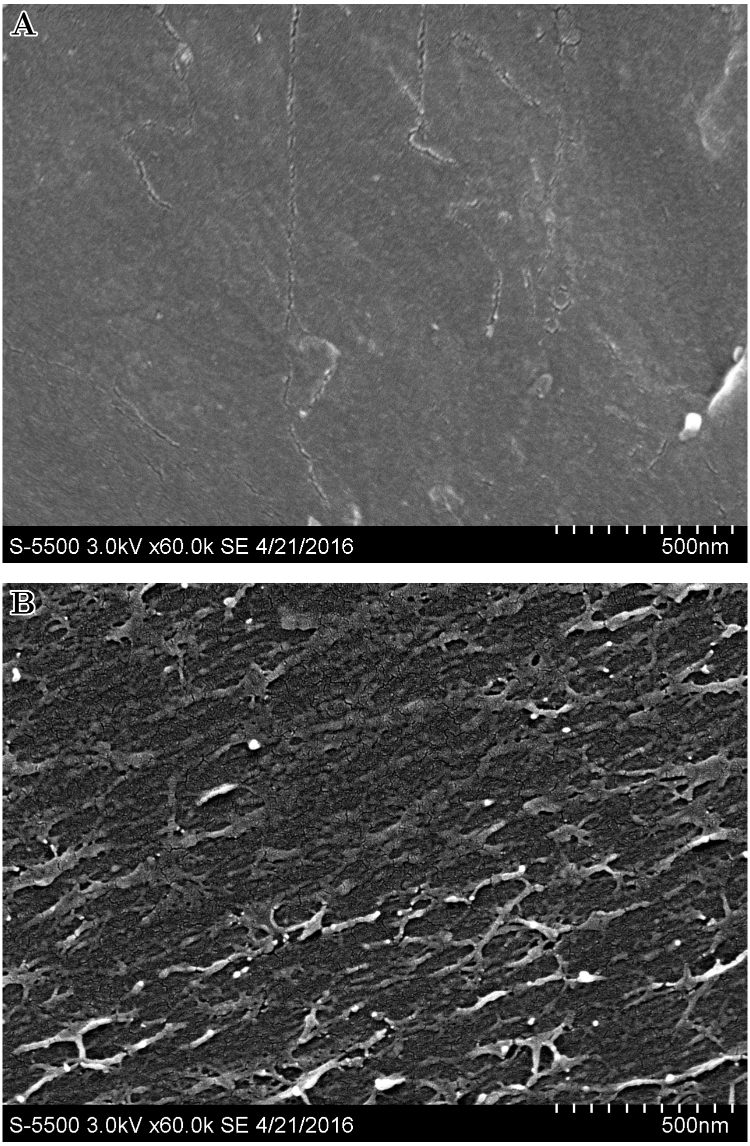

Figure A.4: The bottom surface of PVA films made in a teflon perti dish (A) and in a regular petri dish (B). The surface texture was different between the two films and the teflon film appeared smoother.

A.1.1 PVA/nanocellulose films etched by reactive ion etching

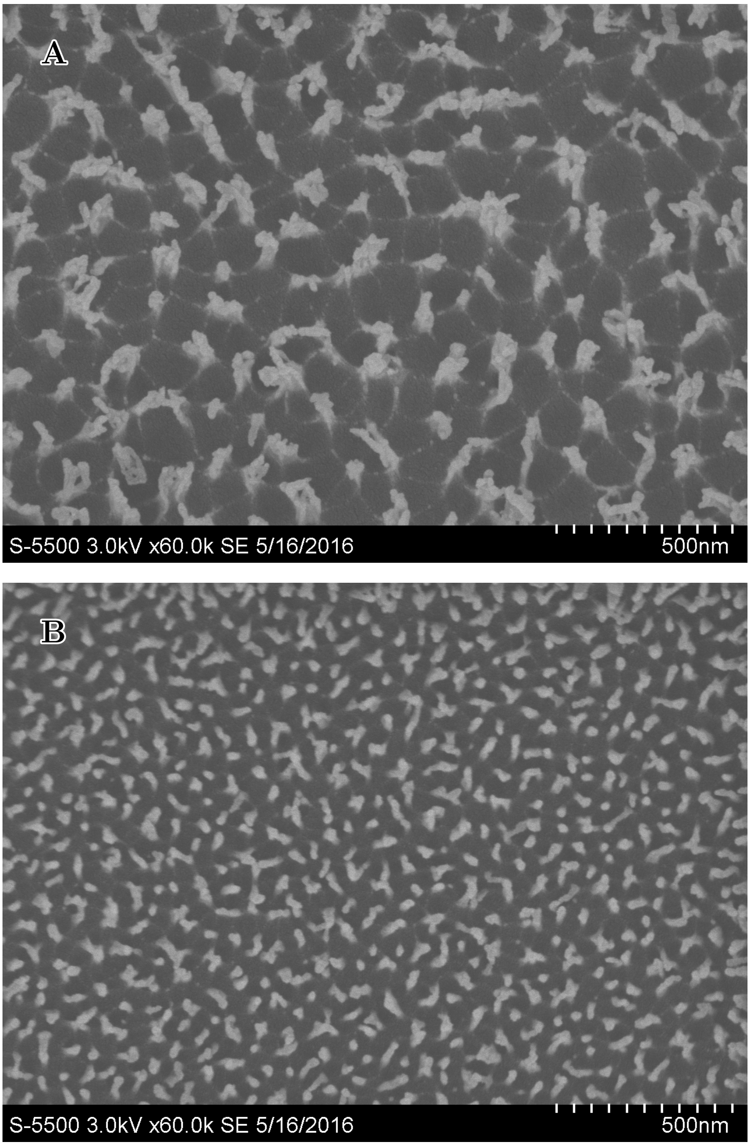

Figure A.5: 4CNF film etched for 1 minute and seconds with SF_6 and Ar. The images show the A. bottom surface and B. top surface

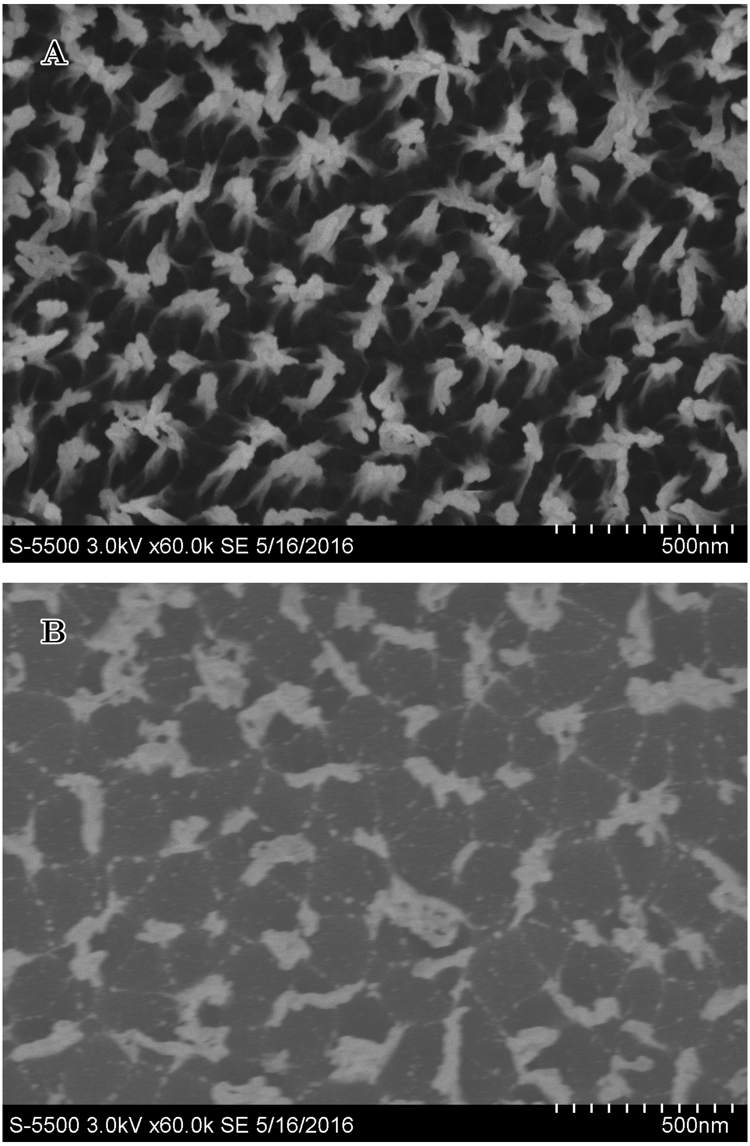

Figure A.6: 4CNF film etched for 3 minutes with SF_6 and Ar. The images show the A. bottom surface and B. top surface

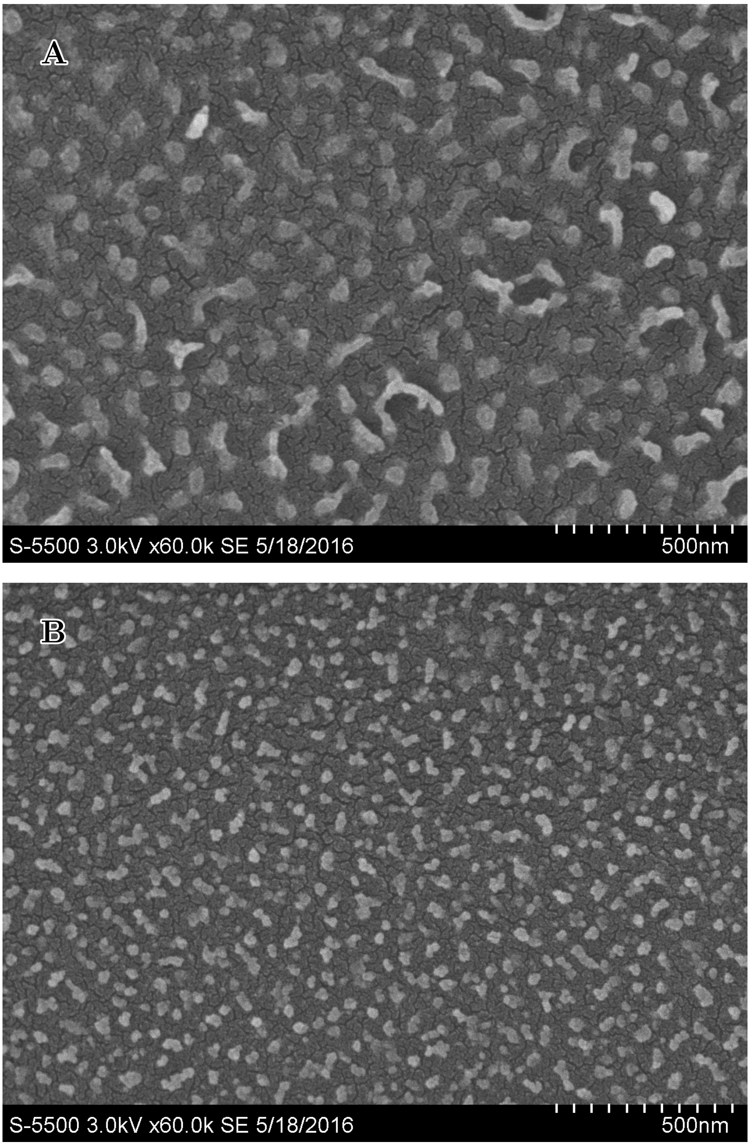

Figure A.7: 4CNC film etched for 1 minute and seconds with SF_6 and Ar. The images show the A. bottom surface and B. top surface

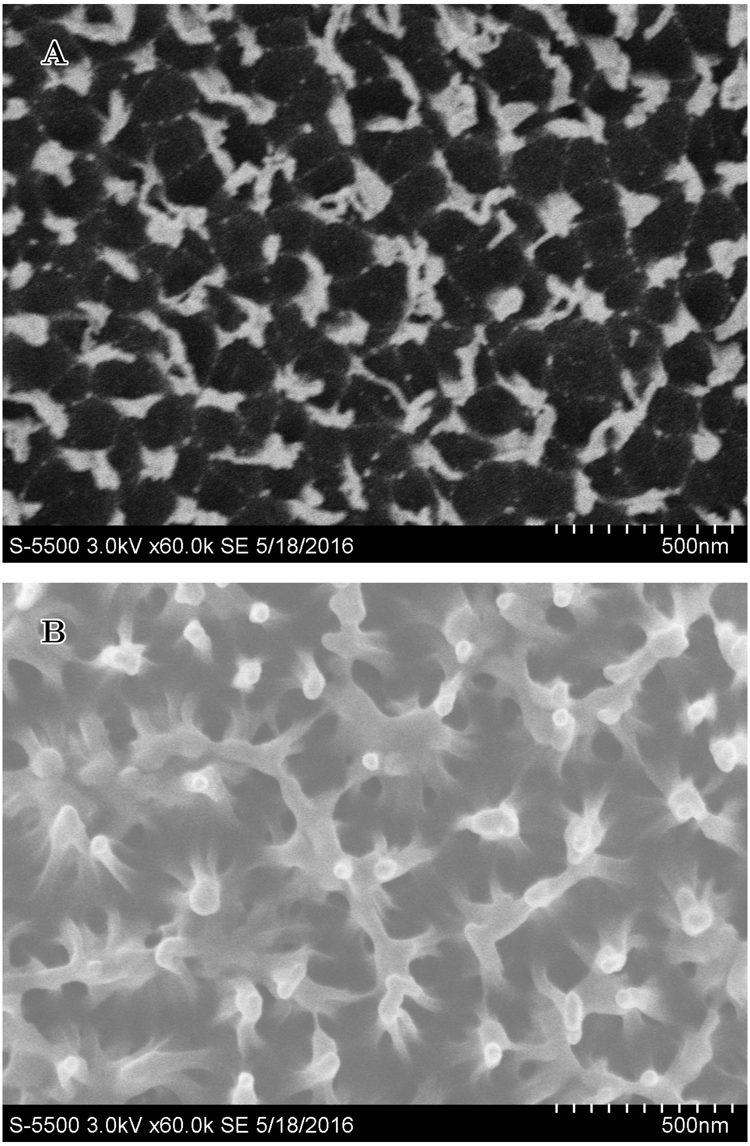

Figure A.8: 4CNc film etched for 3 minutes with SF_6 and Ar. The images show the A. bottom surface and B. top surface

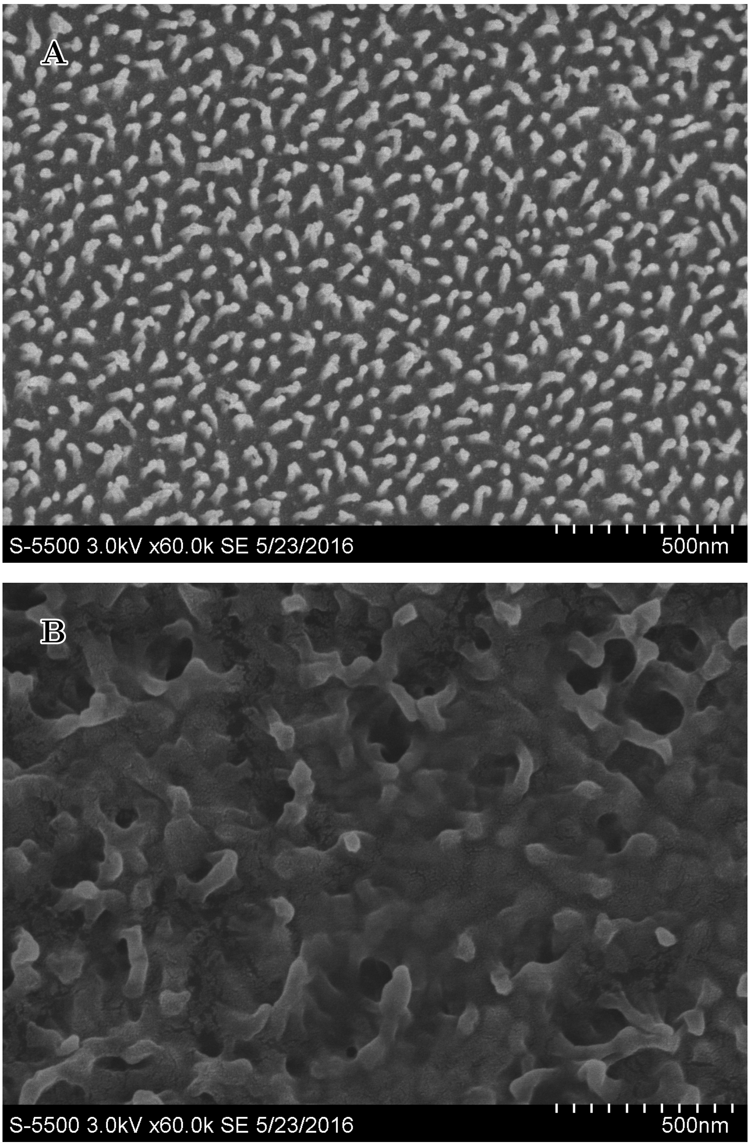

Figure A.9: PVAf film etched for 1 minute and 30 seconds with SF_6 and Ar. The images show the A. bottom surface and B. top surface

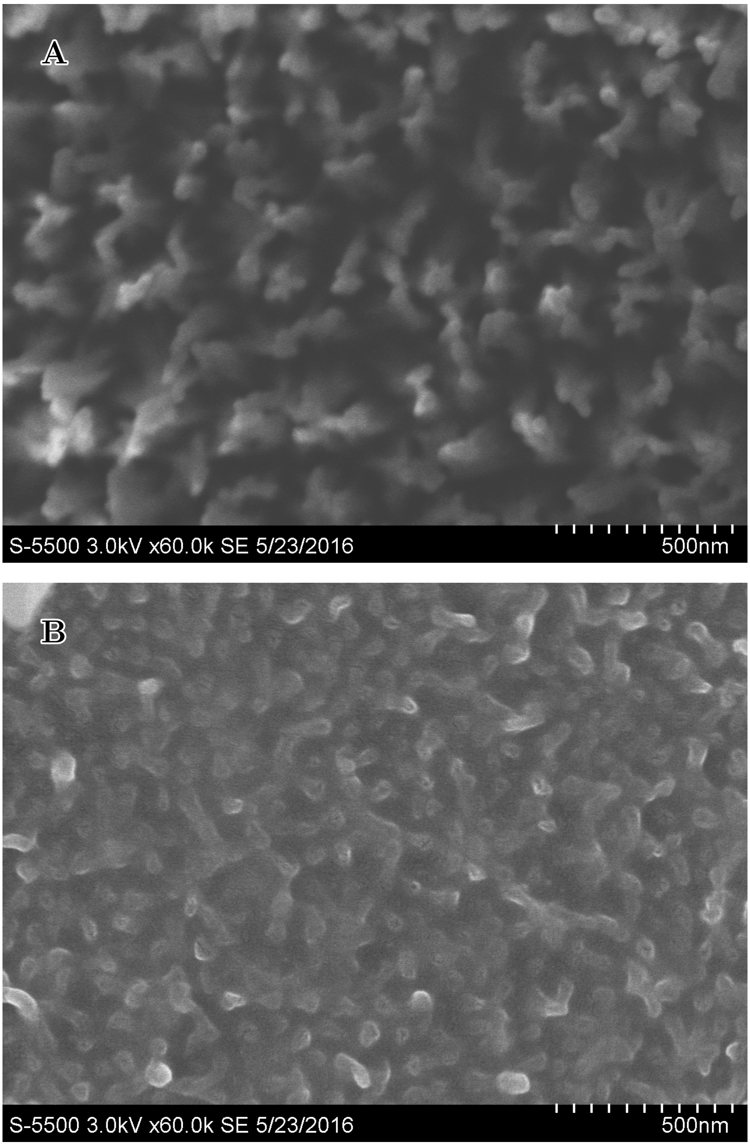

Figure A.10: TeflonPVA etched for 1 minute and 30 seconds with SF_6 and Ar. The images show the A. bottom side and B. top side.

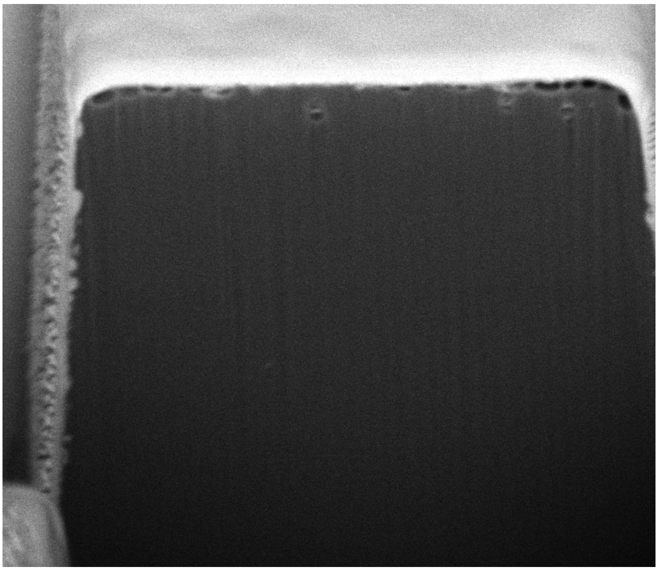

Figure A.11: Example of striations that occured in FIB-SEM cross-sections. The striations persisted throughout the entire slice and view experiment.

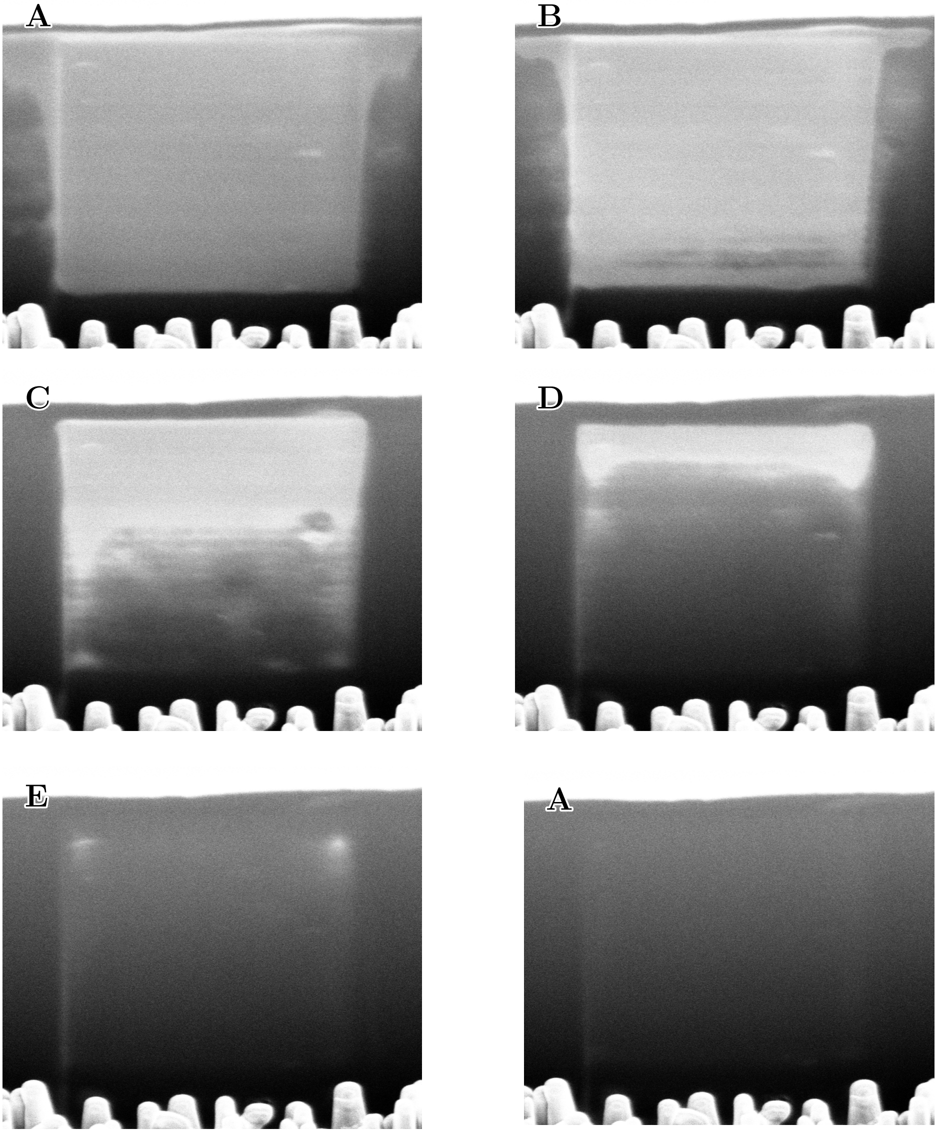

Figure A.12: Sequential micrographs from a slice and view experiment demonstrating the charging effect of increasing magnification.

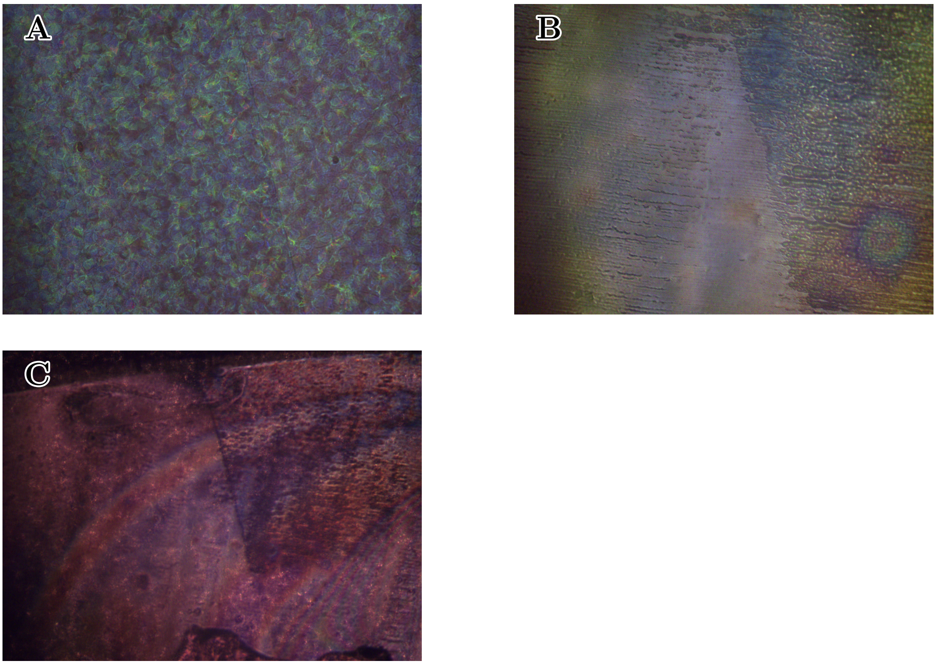

Figure A.13: Optical microscope images of step edges

A.2 Calculations

This chapter has detailed calculations for values used in the discussion.

A.2.1 Backscatter coefficient for a real volume

CNF are small and even at lower voltages not expected to constitute the entire interaction volume. This will in turn affect the backscatter coefficient for this scan point. If an acceleration voltage of 2 kV is used, Table 4.2 showed the interaction volume was approximately 3×10^5 nm^2. The volume of a CNF approximated as a cylinder was 1.4×10^5 with a diameter of 15 nm and a length of 200 nm (Chapter 3.1. CNF would in this case constitute approximately half the interaction volume. Common practice for computing the backscatter coefficient of a multi-component material is a weight-averaged backscatter coefficient [52]. Densities given in Table 3.3 are so similar that volume average can be used instead of weight average. Using values from Figure 4.9, the backscatter coefficient for a point consisting half CNF and half PVA is

$$\eta = 0.5 \times 0.067 + 0.5 \times 0.057 = 0.062 \tag{A.1}$$

The contrast between this volume and a volume containing only PVA will, by Equation 2.9, be

$$C = \frac{0.062 - 0.057}{0.062} = 0.081 \tag{A.2}$$

A.2.2 Contrast from ion-exchanging Cesium for Sodium

For calculating the contrast when exchanging Cs for Na, the average atomic number must be recalculated. Three assumptions were made before calculating. The average dimension of a CNF was 15 nm in diameter og 200 nm in length, the density of CNF was 1.55 g/cm^3 and the density of carboxylic acid groups was 0.85 mmol/g.

First, the mass of one fibril can be calculated from the volume and density where the volume of a fibril was approximated as a cylinder.

$$M_{fibril} = V \times d = 5.48 \times 10^{-17} g \tag{A.3}$$

TEMPO-oxidation replaces some OH-groups with COO$-$Na$^+$ groups. By calculating the number of monomers on one fibril that have their OH-group replaced, the mass percent of each element can be calculated accurately. The mass of one monomer, $C_6H_{10}O_5$, is

$$M_{mono} = 6 \times 12.01 + 10 \times 10.01 + 5 \times 16.00 = 2.69 \times 10^{22} g \tag{A.4}$$

The total number of monomers per fibril is then

$$N_{mono} = M_{fibril}/M_{mono} = 203566 \tag{A.5}$$

The number of acid groups per fibril is then

$$N_{acid} = 0.85 \times 10^{-3} mol/g \times 5.48 \times 10^{-17} g \times N_A = 28051 \tag{A.6}$$

where N_A is Avogadro's number. The number of "unmodified" monomers per fibril is then

$$N_{unmod} = N_{mono} - N_{acid} = 175515 \tag{A.7}$$

Now, each unmodified monomer will have the six carbon atoms, ten hydrogen atoms and 5 oxygen atoms. A TEMPO-oxidized monomer will have six carbon, nine hydrogen atoms, six oxygen atoms and one sodium atom (before ion-exchange). The number of different atoms in a TEMPO-oxidized CNF with sodium as a counter ion is

$$\begin{align} C =& 6 \times N_{mono} = 1221396 \tag{A.8} \\ H =& 10 \times N_{unmod} + 9 \times N_{acid} = 2007609 \tag{A.9} \\ O =& 5 \times N_{unmod} + 6 \times N_{acid} = 1045881 \tag{A.10} \\ Na =& 1 \times N_{mono} = 28051 \tag{A.11} \\ & \tag{A.12} \end{align}$$

This results in weight percents of 43.07% for carbon, 5.90% for hydrogen, 49.13% for oxygen and 1.9% for sodium. The average atomic number of TEMPO-CNF is then

$$Z_{Cs} = 6 \times 0.4307 + 1 \times 0.059 + 8 \times 0.4913 + 11 \times 0.019 = 6.783 \tag{A.13}$$

This does not differ significantly from cellulose which has an average atomic number of 6.678. If we assume that ion-exchange replaces every Na with Cs then using the same approach, the weight percent is 39.50% for carbon, 5.41% for hydrogen, 45.06% for oxygen and 10.04% for cesium. The average atomic number is then

$$Z_{Na} = 6 \times 0.395 + 1 \times 0.0541 + 8 \times 0.4506 + 55 \times 0.1004 = 11.551 \qquad \text{(A.14)}$$

If only half the sodium atoms are replaced, the average atomic number is $Z_{Cs/Na} = 9.267$. The resulting contrast is shown in Figure using Equation 2.5 to calculate the backscatter coefficients and Equation 2.9 to calculate the contrast.

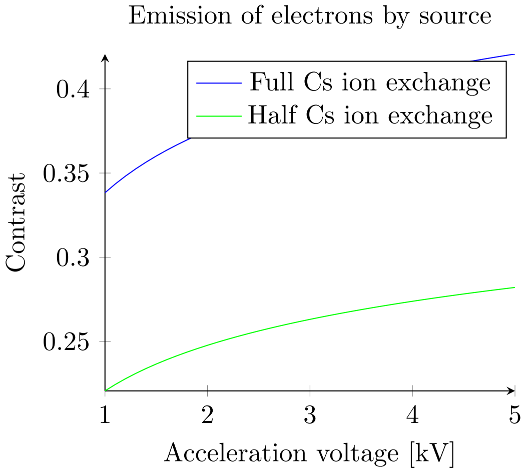

Figure A.14: Bla bla bla.